Photoacoustic Imaging of Evoked Cortical and Subcortical Responses in Small Animal Brain

by

KaiWei Chang

A dissertation submitted in partial fulfillment
of the requirements for the degree of
Doctor of Philosophy
(Biomedical Engineering)
in the University of Michigan
2024

Doctoral Committee:

Professor Xueding Wang, Co-Chair
Assistant Professor Guan Xu, Co-Chair
Associate Professor Zhongming Liu
Associate Professor Kwoon Y. Wong

KaiWei Chang

kaiweic@umich.edu

ORCID iD: 0000-0003-4432-2346

Acknowledgements

I am immensely grateful to my advisors, Dr. Xueding Wang and Dr. Guan Xu, for their invaluable guidance, mentorship, and support throughout my research journey. Their expertise and encouragement have been fundamental in shaping this dissertation.

My heartfelt thanks go to my lab colleagues, Dr. Janggun Jo, Dr. Wei Zhang, Dr. Linyu Ni, Tianqu Zhai, Mingyang Wang, Xiaorui Peng, Zhanpeng Xu, Yaocai Huang, Sumin Park, and Hyeonwoo Kim, for their collaboration and support. Special thanks to Scott Szalay and Scott Almburg for their instrumental and electronic assistance, and Dr. Chunyan Dou for her support on animal handling. I also extend my gratitude to my committee members, Dr. Kwoon Wong and Dr. Zhongming Liu, for their valuable insights and advice.

Finally, profound thanks to my family for their unwavering love and support. Your belief in me has been the driving force behind my accomplishments, and I am eternally grateful.

This work was sponsored by the National Institutes of Health (NIH) R01DK125687, R01EB026897, R01NS118918, R01NS030853, R37CA222829.

Table of Contents

List of Tables

List of Figures

Abstract

Photoacoustic imaging is an emerging, non-invasive biomedical imaging modality, offering a unique blend of high spatial resolution and deep tissue penetration with endogenous contrast agent. This dissertation presents a comprehensive exploration of advanced photoacoustic imaging techniques in neuroscience, focusing on utilizing photoacoustic computed tomography (PACT) and photoacoustic microscopy (PAM) to study hemodynamic responses in the brain for various mouse models and non-human primates (NHPs).

First, a label-free PACT system was developed for imaging mouse brains. This system was employed to monitor hemodynamic responses in the primary visual cortex (V1) during retinal photostimulation. The findings demonstrated the system's sensitivity in detecting differences in response between wild-type mice, rod/cone-degenerate mice, and melanopsin-knockout mice, showing its potential in providing detailed insights into brain activities. Furthermore, the research demonstrated the ability of the PACT system to image not just cortical but also subcortical responses. A total of five visually related brain regions at different depths and coronal planes were simultaneously observed. This demonstrates the versatility and depth of imaging capability in the PACT system.

Second, the application of photoacoustic imaging to NHP models, specifically squirrel monkeys, marked a significant advancement in the research. Photoacoustic imaging techniques, both PACT and PAM, were utilized to detect cortical and subcortical responses to peripheral electrical and mechanical stimulation. The research revealed significant hemodynamic changes in the somatosensory and motor cortices during stimulation. A deep fully connected neural network

was trained and proven to considerably enhance the image quality. This application of photoacoustic imaging in NHPs, which are closer analogs to human brain physiology, established its efficacy in mapping brain functions.

Finally, the dissertation explores the capability of capacitive micromachined ultrasonic transducer (CMUT) arrays in capturing visual-evoked hemodynamic responses in the mouse brain. Demonstrating the comparable performance between CMUT and traditional piezoelectric arrays, this research paves the way for the development of more compact and efficient imaging systems for small animal studies. A wearable imaging device setting was also demonstrated using a catheter ultrasound array.

In conclusion, this dissertation demonstrates significant advancements in photoacoustic imaging for brain research. The collective findings highlight the potential of photoacoustic imaging in overcoming the limitations of traditional neuroimaging modalities, offering non-invasive, label-free detection, high spatial resolution, and the ability to image deep brain structures. This work contributes significantly to the field of neuroscience, offering new insights and methodologies for studying brain functions in small animal models and potentially in clinical settings.

Chapter 1 Introduction

Photoacoustic (PA) imaging (PAI), an emerging modality in biomedical imaging that combines the advantages of optical and ultrasonic technologies. This dissertation explores the application of PAI for studying the complex neural architectures of small animal brains. By utilizing the nature of light absorption and subsequent ultrasonic emission, PAI offers a unique angle to observe and analyze biological tissues, particularly neural structures. The research presented here is propelled by the urgent need to understand the intricate workings of the brain, not just in human models, but also in small animals like mice, which offer a valuable window into the genetic and cellular dynamics of neural functions and disorders. As such, this dissertation presents a comprehensive exploration of photoacoustic computed tomography (PACT) in mouse models, extending to non-human primate (NHP) brains, and culminates in a comparative analysis of capacitive micromachined ultrasonic transducer (CMUT) and piezoelectric transducer arrays in these models. The insights gathered from this investigation are expected to contribute significantly to the field of neuroscience, offering new perspectives for research and therapeutic strategies.

1.1 Overview of Photoacoustic Imaging in Neuroscience

In the field of neuroscience, scientists have long sought imaging techniques that can penetrate the depths of neural tissue without compromising on resolution or causing harm to the subject. PAI emerged as a groundbreaking solution to this quest. It is a technique that combines the high-contrast capabilities of optical imaging with the deep penetration of ultrasound (US), offering an unprecedented view into biological tissues. In neuroscience, particularly, this

technology has opened doors to visualizing and understanding brain activities at a level of detail that was previously unattainable. This imaging technique relies on the PA effect, where pulsed laser light is absorbed by biological tissues, leading to a rapid thermal expansion and the generation of ultrasonic waves [1]. These waves, captured by US detectors, are then used to reconstruct high-resolution images of the brain's internal structures [2].

The adaptability of PAI to study a variety of biological tissues makes it particularly suitable for neuroscience research. It has been effectively used to image the cerebral vasculature, monitor blood oxygenation, and even track the dynamics of neurovascular coupling in animal models [3]. The depth and resolution offered by this method allow researchers to explore the mysteries of the brain, studying everything from the hemodynamic responses in small animal models to the more complex neural structures in NHPs [4]. The evolution of PAI, from its fundamental principles to its advanced applications in brain research, forms a cornerstone of this dissertation.

1.2 Significance of the Research

The significance of this research lies in its potential to transform our understanding of the brain's functionality and its response to various stimuli. The conventional methods of brain imaging, while informative, have been limited by either their invasive nature or lack of depth and resolution [5]. PAI, by contrast, offers a non-invasive window into the brain, allowing for longitudinal studies that can track changes over time, essential in understanding progressive neurological conditions. This research employs state-of-the-art PACT to observe and analyze the neural responses in mouse models. These small animals are crucial in neuroscience research due to their genetic similarity to humans and the feasibility of genetic manipulation, making them ideal

subjects for studying neurodegenerative diseases, brain injuries, and the effects of therapeutic interventions.

Furthermore, this dissertation extends the application of PAI to NHP models, bridging the gap between small animal studies and human applications. This leap is significant as it brings the research one step closer to clinical relevance. Additionally, the comparative analysis of CMUT and piezoelectric arrays in PAI presents an exploration of technological advancements that could redefine the standards of brain imaging. The findings of this research could catalyze the development of more effective, non-invasive diagnostic tools and therapeutic strategies, offering new hope in the battle against neurological disorders. The overall goal of this work is not just to advance the field of PAI but to pave the way for new discoveries in neuroscience, ultimately contributing to better health outcomes and quality of life for those affected by brain-related disease.

1.3 Objectives of this Dissertation

This dissertation aims to contribute significantly to the field of neuroscience through the exploration and application of PAI technologies. It is designed to explore the complex field of brain imaging, utilizing the unique capabilities of PACT, and analyzing its impact on small animal models, primarily mice, and extending to NHPs. The objectives are multifaceted, focusing on both the technical advancements in PAI and the biological insights obtained from these advanced imaging techniques.

1.3.1 Chapter 2: Background

Chapter 2 explores the fundamental principles and evolving applications of PAI, particularly in brain research. This chapter will dissect the technology's basic mechanics and methodologies, emphasizing its critical role in neuroscience. It focuses on how PAI uniquely combines optical and ultrasonic technologies, allowing for an unprecedented exploration of brain structures and functions at various depths. By reviewing current implementations and addressing potential future advancements, this chapter seeks to provide an extensive understanding of PAI's significance and its promising future development in advancing our knowledge of the brain.

1.3.2 Chapter 3: Photoacoustic Computed Tomography of Mouse Brains

Chapter 3 focuses on the application of PACT in mouse models. The specific objectives include establishing specialized PACT systems for detailed brain imaging, investigating cerebral hemodynamics in response to stimuli, and exploring hemodynamic responses in various brain regions. A critical aspect of this chapter is the comparative analysis of responses in genetically modified mouse models, providing insights into the neural correlates of behavior and disease. This chapter seeks to integrate these findings into the broader context of neuroscience, contributing to the development of non-invasive imaging techniques and enhancing our understanding of brain function and disorders.

This chapter is partly adapted from the publication, "**Kai-Wei Chang**, Yunhao Zhu, Xueding Wang, Kwoon Y. Wong, and Guan Xu, Label-free photoacoustic computed tomography of mouse cortical responses to retinal photostimulation using a pair-wise correlation map, *Biomed. Opt. Express*, 13, 1017-1025 (2022)."

1.3.3 Chapter 4: Photoacoustic Imaging of Non-human Primate Brains

Chapter 4 explores the application of PACT and photoacoustic microscopy (PAM) in NHP models. The primary objective is to demonstrate the effectiveness of these imaging techniques in bridging the gap between rodent models and human clinical research. This chapter shows the capabilities of PACT and PAM in capturing detailed cerebral hemodynamics in primate brains, highlighting their potential in studying complex neurobiological processes. A significant focus is placed on the challenges of translating PAI from small animal models to NHPs, emphasizing anatomical, physiological, and cognitive parallels to humans. The chapter also seeks to validate these imaging modalities as powerful tools for advancing our understanding of primate neurobiology, with implications for translational research in neuroscience and the development of diagnostic and therapeutic strategies for neurological disorders.

This chapter is partly adapted from the publication, "**Kai-Wei Chang**[†], Yunhao Zhu[†], Heather M. Hudson, Scott Barbay, David J. Guggenmos, Randolph J. Nudo, Xinmai Yang, Xueding Wang, Photoacoustic imaging of squirrel monkey cortical and subcortical brain regions during peripheral electrical stimulation, *Photoacoustics*, 25 (2022)," and "**Kai-Wei Chang**[†], Madhumithra Subramanian Karthikesh[†], Yunhao Zhu, Heather M. Hudson, Scott Barbay, David Bundy, David J. Guggenmos, Shawn Frost, Randolph J. Nudo, Xueding Wang, Xinmai Yang, Photoacoustic imaging of squirrel monkey cortical responses induced by peripheral mechanical stimulation, *J. Biophotonics* (2024)."

1.3.4 Chapter 5: Comparative Analysis of Mouse Models with CMUT and Piezoelectric Arrays

Chapter 5 aims to conduct a detailed comparative analysis between CMUT arrays and piezoelectric transducer arrays within the context of PAI in mouse models. The primary objective

is to assess the relative strengths, limitations, and application-specific advantages of these two technologies in neuroscientific research. This chapter intends to provide a thorough evaluation of CMUT and piezoelectric arrays in terms of spatial resolution, depth penetration, signal quality, and overall imaging performance, particularly focusing on their effectiveness in capturing detailed cerebral vascular structures and hemodynamic responses. By comparing the outcomes from these two technologies, the chapter seeks to offer insights into their practical utility in neuroimaging, guiding future technological choices and developments in the field. Additionally, it explores the potential of CMUT technology for its miniaturization capabilities and application in more complex, potentially wearable, imaging systems. The ultimate goal is to contribute to the advancement of PAI technology in neuroscience, enhancing our understanding of brain function and aiding in the development of novel diagnostic and therapeutic methods.

This chapter is partly adapted from the publication, "**Kai-Wei Chang**[†], Ermek Belekov[†], Xueding Wang, Kwoon Y. Wong, Ömer Oralkan, and Guan Xu, Photoacoustic imaging of visually evoked cortical and subcortical hemodynamic activity in mouse brain: feasibility study with piezoelectric and capacitive micromachined ultrasonic transducer (CMUT) arrays, *Biomed. Opt. Express*,14, 6283-6290 (2023)."

1.3.5 Chapter 6: Conclusions and Future Work

The final chapter summarizes the major findings of the research conducted on PAI technologies and their application in neuroscience. The primary objective is to synthesize the key discoveries from the previous chapters, including the advancements in PACT in mouse models, the breakthroughs in applying these technologies to NHP brains, and the comparative effectiveness of CMUT and piezoelectric arrays. Furthermore, it outlines a clear view for future research,

focusing on the clinical implications of these findings, the exploration of more compact and integrative imaging systems, and the continuous technological advancement, especially in CMUT technology.

Chapter 2 Background

In this chapter, we review the fundamentals of photoacoustic (PA) imaging (PAI) and its current applications in brain imaging and envision its future potential. This retrospective and prospective view provides essential context for understanding the significance of PAI in neuroscience research.

2.1 Fundamentals of Photoacoustic Imaging

In PAI, tissues are typically irradiated with a short-pulse light source, usually in the nanosecond range. This rapid optical absorption leads to a temporary rise in temperature and consequently, an increase in pressure. The pressure increase, proportional to the temperature rise, propagates as an ultrasonic wave, known as a PA wave. For example, a temperature increase of about 1 m-K can cause a pressure rise of around 800 Pa, which is comparable to the noise level in standard ultrasonic transducers. If the pulse duration is shorter than both the thermal and stress relaxation times, the excitation will meet thermal and stress confinements, allowing for an initial pressure increase to be calculated as:

$$p_0 = \Gamma \cdot \mu_a . F,$$

where Γ is the Gruneisen parameter, which is a dimensionless fraction. It is the ratio of thermal energy converted to kinetic energy. Therefore, it increases with equilibrium temperature. μ_a is the photon absorption coefficient (cm^{-1}), and F is the local optical fluence (J/cm^2).

After the initial pressure generation p_0, an acoustic wave starts to travel at the speed of sound in the medium. The propagation in a non-viscous environment is described by the general PA equation in the time domain, such as:

$$\left(\nabla^2 - \frac{1}{v_s^2}\frac{\partial^2}{\partial t^2}\right) p(\vec{r}, t) = -\frac{\beta}{C_p}\frac{\partial H(\vec{r},t)}{\partial t}, \text{ [7]}$$

where β is the isothermal compressibility and C_p is the specific heat capacity at constant pressure. H is the heating function, defined as thermal energy converted per unit volume and time. It is related to the optical fluence rate Φ (W/cm^2) by $H = \mu_a \Phi$. Applying the Green's function approach to this equation, the heating response of an arbitrary absorbing object can be depicted as:

$$p(\vec{r}, t) = \frac{1}{4\pi v_s^2}\frac{\partial}{\partial t}\left\{\frac{1}{v_s t}\int d\vec{r}' p_0(\vec{r}')\delta\left(t - \frac{|\vec{r}-\vec{r}'|}{v_s}\right)\right\}.$$

For an ideal point transducer, the detected PA signal can be reformed as:

$$p_d(\overrightarrow{r_d}, t) = \frac{\partial}{\partial t}\left\{\frac{t}{4\pi}\iint_{|\overrightarrow{r_d}-\vec{r}|=v_s t} p_0(\vec{r}) d\Omega\right\},$$

where Ω is the solid angle of $\vec{r}$ with respect to $\overrightarrow{r_d}$. It suggests that the detected pressure at a specific time originates from sources across a spherical shell centered at the detector at $\overrightarrow{r_d}$ with a radius of $v_s t$. The initial pressure p_0 can then derived. This is called the universal back-projection (UBP) algorithm for image reconstruction, which can be expressed in the temporal domain as:

$$p_0(\vec{r}) = \frac{1}{\Omega_0}\int_S d\Omega_0 \left\{2p_d(\overrightarrow{r_d}, t) - 2t\frac{\partial p_d(\overrightarrow{r_d},t)}{\partial t}\right\}\Big|_{t=|\overrightarrow{r_d}-\vec{r}|/v_s},$$

which indicates that the initial pressure p_0 can be obtained by back-projecting the filtered data, $p_d(\overrightarrow{r_d}, t) - 2t\frac{\partial p_d(\overrightarrow{r_d},t)}{\partial t}$, onto a collection of concentric spherical surfaces that are centered at each transducer location $\overrightarrow{r_d}$, with $d\Omega_0/\Omega_0$ as the weighting factor applied to each back-projection. The first derivative with respect to time represents a ramp filter, which suppresses low frequency signals. Therefore, the UBP reconstruction algorithm essentially functions as an advanced

triangulation method for locating PA sources using time-resolved acoustic signals [8]. Also, the unfiltered UBP is numerically equivalent to the delay-and-sum (DAS) beamforming method commonly used in ultrasound (US) imaging systems [9].

2.2 Current Brain Imaging Techniques in Mouse Models

Mouse models are extensively used in vision research due to their genetic similarities to humans and ease of genetic manipulation [10]. While there are numerous methods to examine retinal phenotypes in these models [11], assessing higher visual areas poses considerable challenges. Traditionally, extracellular microelectrodes have been the primary tool for *in vivo* brain recording, especially in subcortical nuclei [5]. However, positioning these electrodes accurately is challenging, and they often record from only a limited subset of neurons, which may not fully represent the region's overall activity.

Existing assays for regions like the olivary pretectal nucleus (OPN), accessory optic system, and visual cortex are not available for significant retinal ganglion cell (RGC) targets like the superior colliculus (SC), dorsal lateral geniculate nucleus (LGd), and suprachiasmatic nucleus (SCN). Additionally, high-pass filtering in cortical field potential recordings makes it difficult to detect low-frequency responses, particularly those driven by melanopsin-expressing, intrinsically photosensitive retinal ganglion cells (ipRGCs) [12,13]. Functional magnetic resonance imaging (fMRI) offers good spatial and temporal resolution for mouse SC, LGd, and primary visual cortex (V1) [14], but its effectiveness is limited by the use of anesthesia [15] or physical restraint [13,16], which can have physiological side effects. For example, mice anesthetized with 1% isoflurane exhibit slower pupillary light reflexes compared to those under 0.5% isoflurane, as shown in Figure 2.1 [15]. Anesthesia has also been found to affect SCN photoresponse sensitivity [17] and duration

[18,19]. Though stress-reducing drugs have been used for unrestrained, unanesthetized animals [20], they can have their own adverse effects [21–28]. Therefore, our studies with anesthetized mice followed a protocol [15] to minimize isoflurane levels to 0.5%.

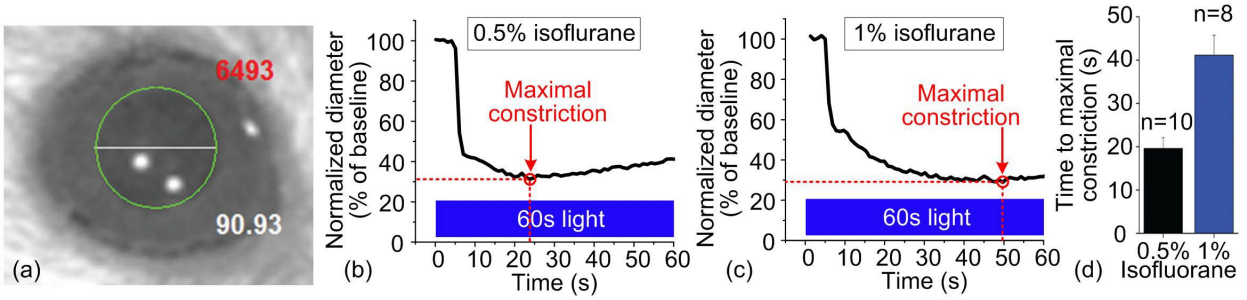

Figure 2.1: Pupil responses in anesthetized mice. (a) The pupil outline is fitted with the green circle, whose diameter (white value) is then calculated. The circle's area (red value) is not used in this study. (b, c) Example pupil responses for (b) a mouse anesthetized by 0.5% isoflurane and (c) another by 1% isoflurane. (d) Statistics on population-averaged data.

Functional near-infrared spectroscopy (fNIRS) has been successful in imaging human brain hemodynamics due to its mobility and temporal resolution [29], but its inability to spatially resolve visual nuclei in mice limits its use. On the other hand, photoacoustic computed tomography (PACT) overcomes this by merging the contrast mechanism of fNIRS with US imaging's spatial resolution. In PACT, nanosecond light pulses cause biological tissues to emit acoustic signals, captured by a US transducer array, to create images with optical contrast and US resolution. PACT systems can image at high frame rates [30] with ~100 μm resolution at 1 cm depth [1]. In recent years, PACT has been demonstrated to be able to study functional connectivity in mouse cortical areas [31,32] and capture cortical hemodynamic responses to electrical stimulations [4,33,34] and in free-moving rats [33,35].

2.3 Current Brain Imaging Techniques in Non-human Primate Models

NHPs are pivotal in advancing medical and scientific research, particularly in the study of the brain due to their physiological closeness to humans. Animal models based on NHPs are crucial for addressing specific research questions that are less feasible with other species [36]. The development of effective functional imaging methods for the NHP brain is crucial for enhancing our understanding of various brain functions and could be relevant to a range of neurological conditions like stroke, Alzheimer's disease, Parkinson's disease, and epilepsy [37,38].

Historically, invasive neurophysiological electrical recording techniques in NHPs have shed light on the functional organization of the primate brain. While these methods offer good spatial and depth-resolved insights, they are restricted to small tissue areas and are challenging to use for in-depth brain function studies. Deep brain structures, several centimeters beneath the cortex, are critical in sensorimotor processing as well as cognitive, affective, and social functions linked to psychiatric disorders like schizophrenia, depression, and autism spectrum disorders [39]. However, the role of specific subcortical nuclei abnormalities in neurocognitive and socio-functional outcomes remains largely unexplored.

fMRI is commonly used for detecting whole-brain functional changes [40–45]. Yet, fMRI is hampered by high costs and limitations in spatial and temporal resolution, particularly problematic when studying awake, active monkeys, where motion artifacts can impede accurate data collection [46–48]. The use of human MRI scanners in NHP research is fraught with technical issues such as motion artifacts, which are challenging to mitigate [48,49]. Even under anesthesia, motion artifacts caused by cardiac and respiratory cycles persist in fMRI data.

Optical brain imaging offers a lower-cost alternative to other modalities like microelectrode recordings and fMRI, and can be performed in real-time [50–57]. This method has

expedited progress in various fields, including neuroscience, psychology, and psychiatry. In NHP studies, optical imaging has enabled the visualization of functional modules in the cerebral cortex, particularly in visual, auditory, and somatosensory areas [58,59]. It works by monitoring blood oxygenation changes related to neural activity and detecting tissue optical properties via absorption or scattering. However, due to intense light scattering in brain tissue, high-resolution optical microscopy is limited to the cortex's surface, while diffuse optical methods accessing subcortical regions have poor spatial resolution and limited depth information.

Ultrafast Doppler-based functional ultrasound imaging (fUS) has recently shown promise in imaging cerebral blood volume (CBV) in NHPs [60]. However, fUS mainly detects larger blood vessels and has limited sensitivity to capillary flow. Crucially, it cannot assess blood oxygenation (sO2), a key brain function indicator.

PACT emerges as a novel solution to these challenges in NHP brain imaging. It can capture optical information deep within brain tissues with superior ultrasonic spatial resolution (below 300 μm) at depths exceeding 3 cm [61,62]. Extensive research has demonstrated PACT's ability to map structural and functional information in small-animal and monkey brains [63–70]. PACT can quantitatively track changes in blood volume and oxygen saturation, assessing brain tissue metabolism linked to brain functions. A PACT system, potentially wearable and non-restrictive, could be mounted on a monkey's head to map brain function through a cranial window, providing in-depth, high-resolution insights into subcortical areas in real-time.

2.4 Current Development of CMUT Arrays in Photoacoustic Brain Imaging

Although 3D PACT using a 1D US transducer array and mechanical translation is popular [71–74], its weight and bulkiness limit its use in free-moving mice. PACT with 2D [75] or 3D [76] transducer arrays offers promise for high frame rate and large aperture imaging, improving

resolution. However, the weight of traditional piezoelectric transducer arrays and front-end electronics increases with the element count. Recent advances have enabled the creation of lightweight US transducer arrays and isolated frontend electronics. A pilot study developed a ring-shaped, head-mounted 3D PVDF transducer array for free-moving rats, successfully recording PA signals in the visual cortex [33,35]. Despite its lower sensitivity and frequency range compared to the piezoelectric arrays, the PVDF array lacks the spatial resolution and penetration depth needed for subcortical nuclei analysis.

Capacitive micromachined ultrasonic transducer (CMUT) arrays offer advantages in fabrication techniques and performance metrics, making them a promising option for small-animal PACT systems. CMUTs have been used in various medical applications, including Doppler [77,78], intravascular US [79], PAT [80,81], and US therapy [82–84]. It is demonstrated that wafer-bonded CMUTs are simpler, faster, and offer greater design flexibility [85]. This results in uniform quality, reduced costs, and the easy integration of transducer arrays with electronic circuits, which is critical for high-frequency applications. CMUTs, compared to traditional piezoelectric arrays, provide similar sensitivity [86,86] but with a much wider (>40%) bandwidth, significantly enhancing PACT image quality [87–89]. A 256-element 1D CMUT array using anodic bonding and constructed imaging probes with in-probe frontend electronics has recently been developed. These ultrawideband arrays, operating at 3–25 MHz [90,91], offer the high output pressure and bandwidth necessary for improved image quality in cutting-edge PACT and US imaging systems.

The thin substrates used in CMUT fabrication, the elimination of thick backing layers, and the close integration of transducer arrays with frontend electronics make CMUTs ideal for creating miniaturized probes for wearable devices. A lightweight, wearable 1D [92] and 2D [93] CMUT

arrays for mice, featuring wireless communication or flexible cable connections to backend electronics has been reported. The close integration of frontend electronics and the wide bandwidth of CMUTs yield high-quality images characterized by a high signal-to-noise ratio (SNR) and fine resolution. Such arrays have potential to effectively quantify visual-evoked hemodynamic responses in key brain regions of freely moving mice and detect subtle alterations in transgenic mice and disease models.

2.5 Future Directions in Photoacoustic Brain Imaging

The future development of PA brain imaging is set towards enhancing its application in both research and clinical settings. It includes the development of PA systems with higher repetition rates to match the scale of electrophysiological measurements and the expansion of imaging capabilities to deeper brain regions such as the suprachiasmatic nucleus (SCN).

There is also an emerging interest in leveraging multiple optical wavelengths within PAI to assess blood oxygenation changes. This technique stands out for its potential to provide detailed insights into cerebral hemodynamics by assessing blood oxygenation levels and metabolic rates. By employing a range of optical wavelengths, it becomes feasible to distinguish between oxyhemoglobin and deoxyhemoglobin, offering more understanding of brain oxygenation and its fluctuations during different physiological and pathological states. This capability is pivotal for exploring complex brain functions and dysfunctions, as it allows researchers to observe and quantify the dynamic changes in blood oxygenation associated with neuronal activity.

Furthermore, in order to eliminate anesthesia interference by imaging freely moving mice, innovations in array technologies, especially in the field of CMUTs, are expected to lead to more

compact, flexible, and sensitive imaging systems. This facilitates the functional assessment of brain activity under normal physiological conditions and in longitudinal studies.

Last but not least, the integration of advanced computational techniques, such as deep learning and neural networks, in processing PA images promises to significantly enhance image quality and signal detection.

Chapter 3 Photoacoustic Computed Tomography of Mouse Brains

3.1 Introduction

This chapter presents the methodologies used in our photoacoustic computed tomography (PACT) imaging study, focusing on capturing hemodynamic responses in the mouse brain. It introduces two PACT systems: one featuring a full-ring array for transverse plane imaging and another with a linear array for the coronal plane (Figure 3.1). Each system is uniquely tailored with specific laser wavelengths – 1064 nm for the full-ring array and 797 nm for the linear array – to ensure precise imaging while avoiding interference with visual stimuli. It also elaborates on the sophisticated image reconstruction and signal processing techniques employed to analyze hemodynamic responses from photoacoustic (PA) signals, which are crucial in distinguishing brain activities from background noise.

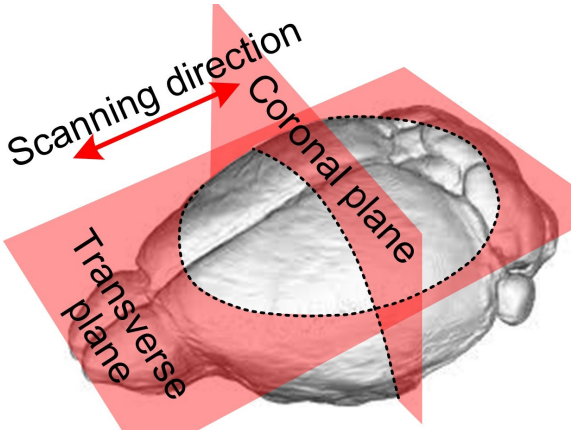

Figure 3.1: Imaging planes of the PACT system.

3.2 Material and Methods

3.2.1 PACT System Using Full-Ring Array

Figure 3.2 illustrates the design of our ring-array PACT system for real-time imaging of the mouse brain. We employed a Nd:YAG laser (Quantel, Brillant B) operating at 1064 nm as our excitation source. The laser features a pulse duration ranging between 4-6 ns, a repetition rate of 10 Hz, and less than 5% variation in pulse energy. This specific wavelength was selected due to several key reasons. Firstly, it aligns with the insensitivity of mouse retinal photoreceptors to near-infrared (NIR) light [94,95], ensuring that our imaging process does not disrupt visual stimulations. Secondly, previous studies in brain PA imaging (PAI) have demonstrated that at 1064 nm, oxygenated hemoglobin (HbO_2) has adequate optical absorption to effectively monitor hemodynamic changes, and water's limited attenuation at this wavelength enables satisfactory optical penetration in mouse brain tissue. Additionally, the low pulse energy variation is critical in reducing measurement errors, enhancing the accuracy in capturing genuine signals linked to cortical activities. We expanded the laser beam to a diameter of 1 cm using a combination of concave and convex lenses, ensuring full coverage of the mouse brain's horizontal surface. The optical fluence at the skull was maintained at roughly 50 mJ/cm^2, within the American National Standards Institute's safety threshold of 100 mJ/cm^2 for 1064 nm. For the detection of PA signals, we utilized a custom-made 256-element full-ring ultrasonic transducer array with a 5 cm inner diameter. This array features an 80% bandwidth at a central frequency of 10 MHz and offers an axial resolution of 400 μm and lateral resolution of 200 μm within the 2-cm-diameter central field of view. The PA signals captured were then digitized and sampled at a frequency of 40 MHz using the Vantage 256 ultrasound research system by Verasonics (Redmond, WA).

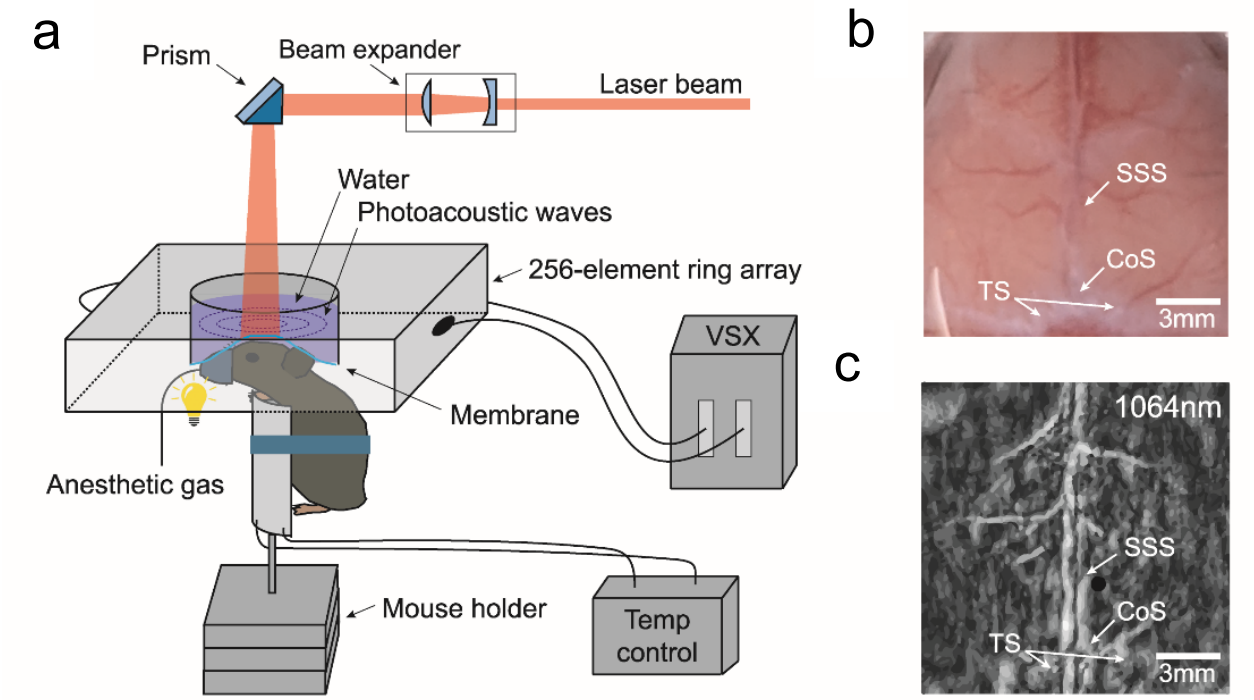

Figure 3.2: Full-ring PACT system. (a) Schematic of the PACT system. (b) Photograph of the cortical vasculature of a mouse brain with the scalp removed. (c) The representative PACT image using 1064 nm excitation light. (VSX: Verasonics system, SSS: the superior sagittal sinus, TS: the transverse sinus, and CoS: the confluence of sinuses)

3.2.2 PACT System Using Linear Array

Figure 3.3a shows a schematic of the alternative design of our PACT system using linear array for imaging coronal planes of mouse brain. The laser beam at 797 nm was used in order to avoid interference with the visual stimulation. Besides, at this wavelength, the oxygenated and deoxygenated hemoglobin have the same absorption coefficients. Similar to the full-ring array system, the laser has a pulse duration of 4-6 ns and a repetition rate of 10 Hz. It was delivered through a bifurcated, multimode fiber bundle with fiber tips attached on both sides of a linear 256-element ultrasonic array (GE L8-18i) with a central frequency of 10 MHz. The maximum optical fluence at the skull surface was ~20 mJ/cm^2, which is below the American National Standards Institute (ANSI) safety limit of 31 mJ/cm^2 at 797 nm. The PA signals were digitalized and sampled

at 40 MHz with a Vantage 256 ultrasound research system (Verasonics, Redmond, WA). The PACT system had an axial resolution of 150 μm and a lateral resolution of 150 μm within 2-cm imaging depth. The translational stage in Figure 3.3b scans through the mouse brain for PACT of different coronal planes, covering all the targeted brain nuclei, including primary visual cortex (V1), superior colliculus (SC), dorsal lateral geniculate nucleus (LGd), olivary pretectal nucleus (OPN), and suprachiasmatic nucleus (SCN) (Figure 3.4). The complete scanning cycle, covering all 3 planes and also serving as the temporal resolution of the system for imaging each nucleus, is executed in 1.2 sec. The positions of these targeted nuclei are shown on the corresponding ultrasound (US) images. A representative PA image is also shown in Figure 3.3c.

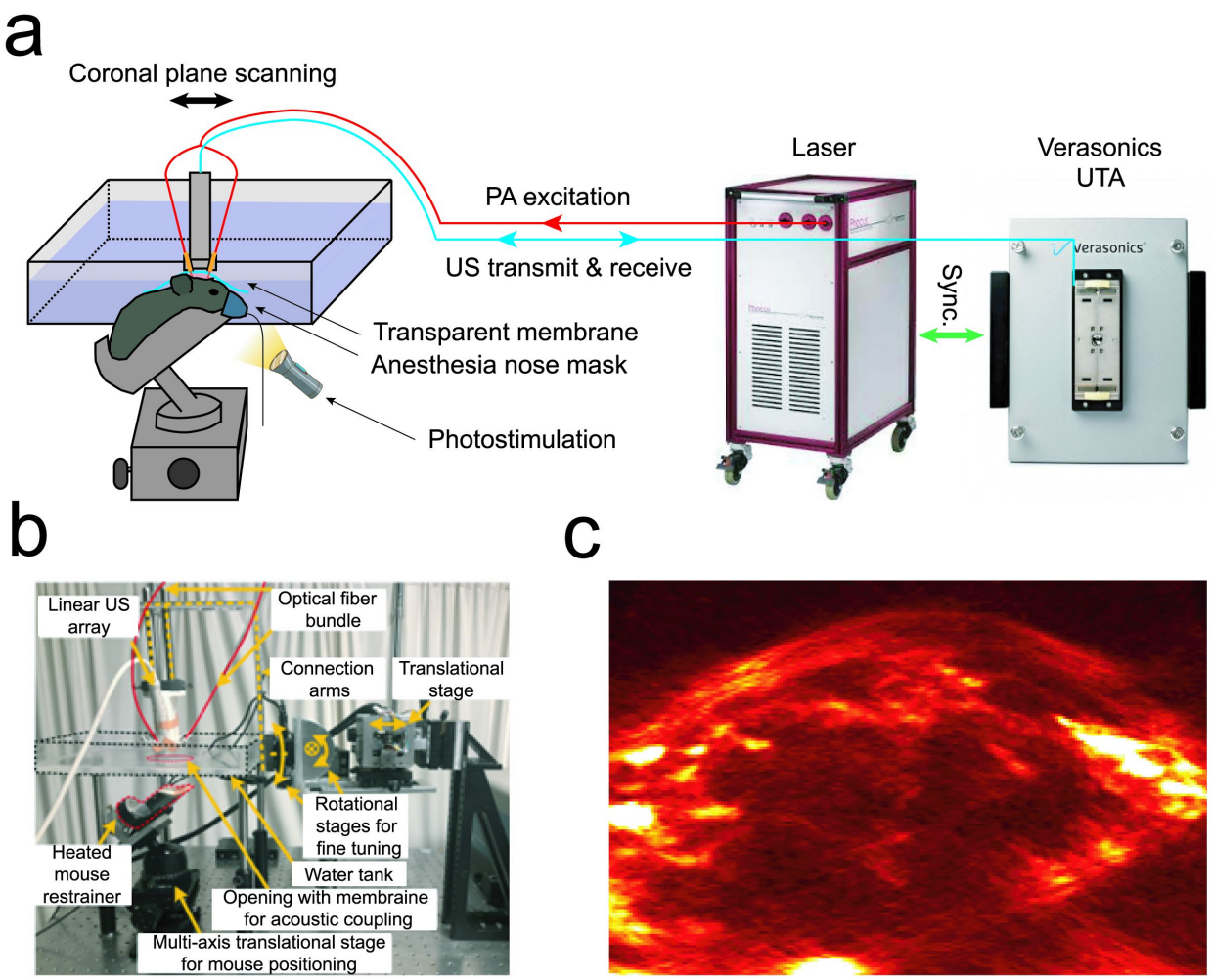

Figure 3.3: Linear array PACT system. (a) Schematic of the PACT system. (b) The photograph of the system and the translational stage for coronal plane scanning. (c) A representative photoacoustic image from the system.

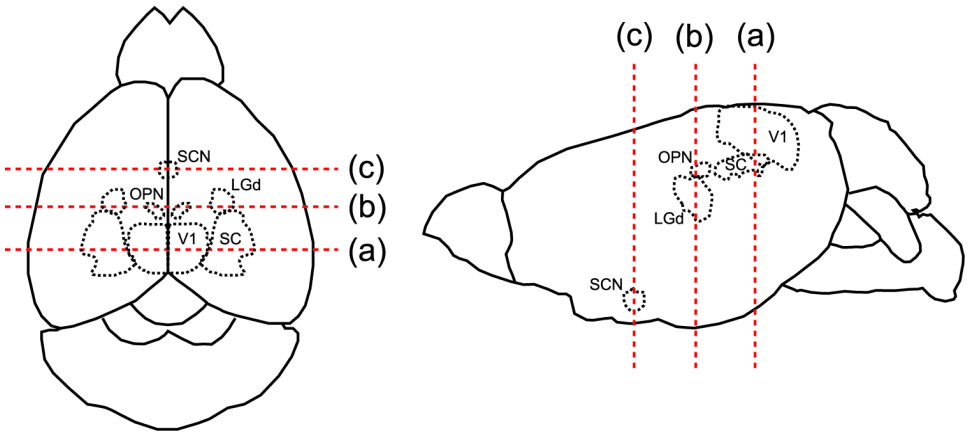

Figure 3.4: The positions of the targeted brain nuclei in the mouse brain, including V1, SC, LGd, OPN, and SCN. The 3 scanning planes are indicated with red dashed lines.

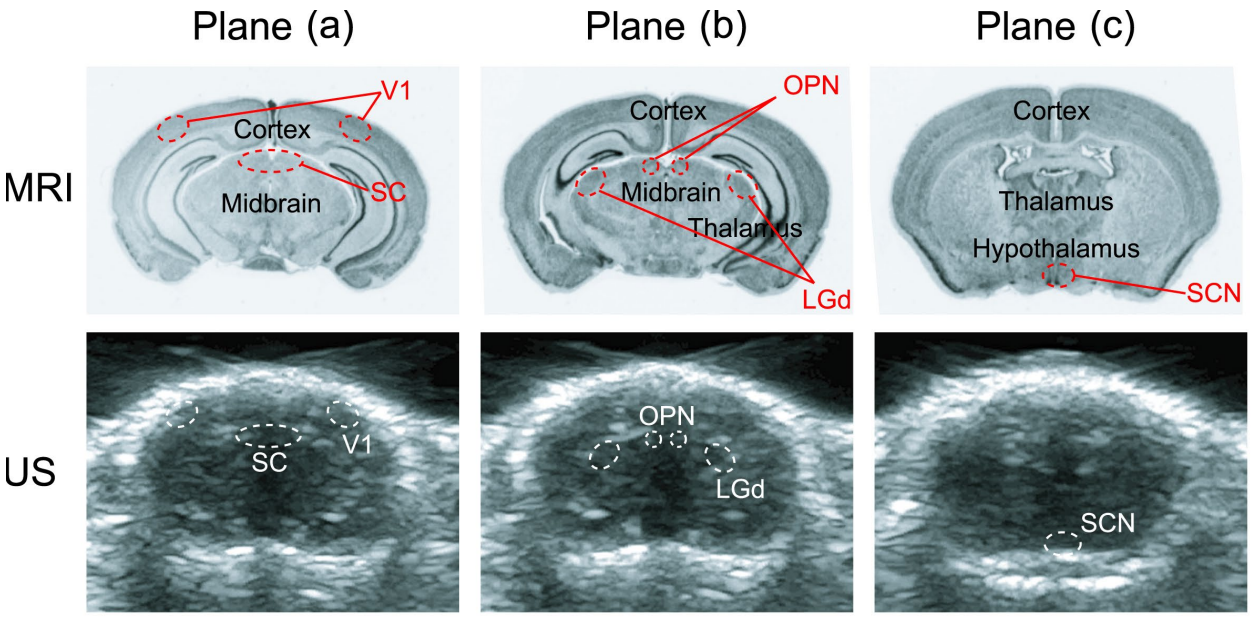

Figure 3.5: The MRI, and US images of the mouse brain for the 3 imaging planes. The contours of the targeted nuclei are marked on the images.

3.2.3 Mouse Models and Animal Preparation

The Institutional Animal Care and Use Committee at the University of Michigan granted approval for all procedures involving animals in this study. We utilized C57BL/6 wild-type mice homozygous *rd1* retinal degenerate mice, and melanopsin-knockout (mel-ko) mice, aged between 4 to 7 months, and kept them on a 12-hour light/dark cycle. PACT was conducted during their light cycle. Prior to imaging sessions, each mouse underwent overnight dark adaptation and received anesthesia through 1% isoflurane, delivered at a flow rate of 1.5 L/min, complemented by an intraperitoneal injection of acepromazine at a dosage of 5 mg/kg [15]. To reduce optical and acoustic signal loss, the scalp of each mouse was carefully removed. The animals were then positioned on a multi-axis translation stage, ensuring the brain's surface was correctly aligned with our imaging apparatus. Upon completion of the imaging procedures, humane euthanasia was conducted via inhalation of carbon dioxide, followed by inducing bilateral pneumothorax.

3.2.4 Skull thinning

Prior to our PACT imaging of mouse brains, a skull thinning procedure was implemented, essential for reducing optical and acoustic attenuation and enhancing image quality. Mice were anesthetized through 2-5% isoflurane and placed on a heated pad to maintain body temperature, with continuous monitoring to ensure adequate depth of anesthesia. The scalp was shaved and cleaned, followed by a precise midline incision to expose the skull. After lubricating the eyes to prevent dehydration, a microsurgical blade was used to gently scrape away connective tissue from the skull, with local analgesia applied as needed. The skull was then immobilized using ear pins on a skull holder. A high-speed micro-drill (SDE-H102S, Shiyang), intermittently used to prevent overheating, thinned the skull over the target region. The drilling was carefully monitored to avoid

excessive thinning or damage to the underlying cortex. This process resulted in a thin (~20 μm), smooth skull window, allowing for optimal imaging conditions.

3.2.5 Retinal Photostimulation

For visual stimulation, we employed a fiber-optic halogen illuminator (HL150-B, AmScope), emitting broadband white light that flickered at a frequency of 1 Hz. This illuminator was positioned roughly 5 cm away from each eye of the mouse, resulting in a corneal irradiance of about 16 mW/cm^2. Prior to initiating the light stimulus, mice were kept in complete darkness for initial baseline measurements. Subsequently, we exposed both eyes of the mouse to the flickering light for a duration of 10 or 20 seconds. This was followed by a 10-minute period of darkness. During this time, our PACT system persistently tracked the hemodynamic changes and recovery in response to the visual stimulus.

3.2.6 Image Reconstruction and Signal Processing

For the reconstruction of PACT images of both systems, we utilized a delay-and-sum (DAS) beamforming algorithm, processing the signals we had gathered. In order to adjust for any movement of the brain due to the animal's respiration or heartbeat, we aligned the frames from the time-lapse PACT video using reference points. For full-ring array system, the reference points are the key blood vessels, including the superior sagittal sinus (SSS), transverse sinus (TS), and confluence of sinuses (CoS), as illustrated in Figure 3.2b and c. For linear array system, the reference points are on the surface of the thinned skull surface. We extracted the temporal trace from each pixel in the PACT video, spanning 600 consecutive frames over a one-minute duration.

This sequence included 200 frames prior to the stimulus, 200 during the stimulus, and 200 immediately following it, as shown in Figure 3.6a. Each series of 600 frames was initially corrected by removing the linear trend from the pre-stimulation temporal trace, effectively eliminating any systematic shifts in the detected signal. Subsequently, these traces were normalized against the root-mean-square value of the signal strength from the original pre-stimulation trace, yielding baseline-corrected and normalized PA (ΔPA/PA) signals. We further refined the data by applying a spatial moving average across 3×3 pixels and a temporal forward-moving average over 25 frames (equivalent to 2.5 seconds), aiming to eliminate noise caused by random fluctuations, as depicted in Figure 3.6b.

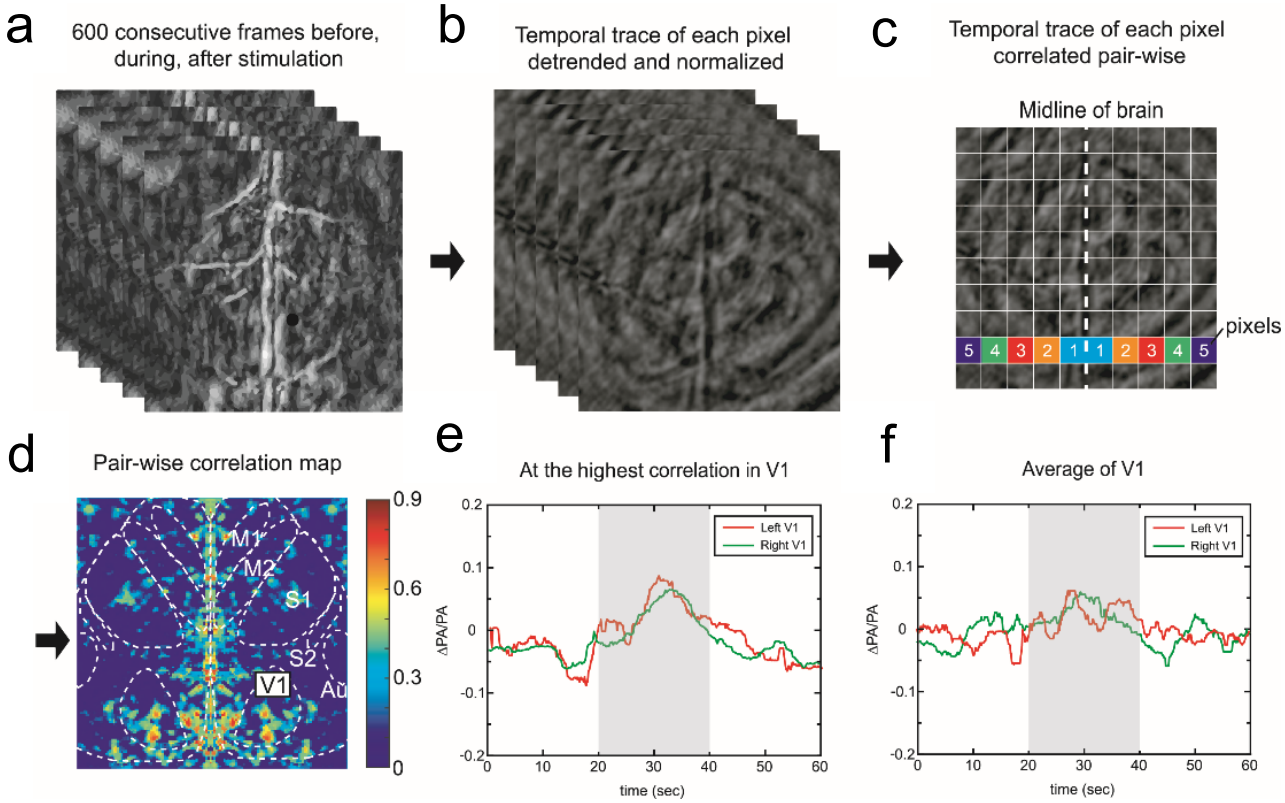

Figure 3.6: Demonstration of the pair-wise correlation map. (a-c) The procedure of the production of a pair-wise correlation map. Consecutive frames covering a 1-min period were detrended and normalized. The temporal trace of each pair of pixels was then correlated pair-wise to produce the correlation map. (d) A representative correlation map during visual stimulation. (M1: primary motor cortex, M2: secondary motor cortex, S1: primary somatosensory cortex, S2: secondary somatosensory cortex, Au: auditory cortex, and V1: primary visual cortex) (e) The temporal traces of the background-subtracted and normalized PA signals (ΔPA/PA) for a single pixel at the highest correlation coefficient

located in V1 in (d) from both left (red) and right (green) hemispheres. (f) The average temporal traces of ΔPA/PA for all pixels within V1 from both left (red) and right (green) hemispheres. The shaded area represents the period of visual stimulation.

3.2.7 Pair-wise Correlation Map and Temporal Trace Analysis

In order to more precisely discern the hemodynamic response triggered by retinal photostimulation, we employed a strategy based on calculating pair-wise correlation maps from our PACT brain images. Initially, we divided the brain images into two distinct hemispheres, left and right. We then paired pixels that were symmetrically positioned on either side of the brain's midline, as depicted in Figure 3.6c. For each pixel pair, we computed the correlation coefficient by comparing the temporal traces from the left and right hemispheres. This calculation resulted in a correlation map for each set of paired pixels. Given that both eyes of the mouse were subjected to the stimulus, we anticipated a corresponding hemodynamic response on both sides of the brain. If the alterations in the PA signals were genuinely indicative of a hemodynamic response, then the variations in signal from both brain halves would exhibit similar patterns in terms of amplitude and timing, leading to high correlation coefficients. Conversely, should the PA signal changes be attributable to random noise, the temporal traces would exhibit random fluctuations in intensity, yielding low correlation coefficients in the pair-wise map. This method significantly improves the identification of genuine hemodynamic responses amid random background noise, as illustrated in Figure 3.6d. We pinpointed the hemodynamic response by focusing on temporal traces at positions where the highest left-right correlation coefficients were observed, as shown in Figure 3.6e. Compared to the mean temporal traces in the left and right V1 regions, this method effectively dampened random fluctuations (Figure 3.6f). We then quantified the response amplitude and peak latency of the visually induced hemodynamic response, assessed the data distribution for normality

using the Shapiro-Wilk test, and compared the findings between wild-type and *rd1* mice through a two-tailed Student's t-test. Additionally, any potential differences between male and female subjects were also investigated.

3.2.8 Isolation of the Hemodynamic Response

In our study, we have adopted a refined process for differentiating the hemodynamic response (HR) from the background noise in PA signals, building upon established techniques used in functional magnetic resonance imaging (fMRI) [96] and functional near-infrared spectroscopy (fNIRS) [97,98]. This method, influenced by our extensive background [53,99–101] and informed by other leading studies [97,98,102,103], employs a specific protocol:

Firstly, a bandpass filter ranging from 0.01 to 1.25 Hz is applied to the frequency domain spectra of the PA signals. This step is crucial for reducing repetitive noises stemming from physiological activities like respiration and heartbeat, as well as low-frequency baseline signals. We then implement a Kalman filter to eliminate autocorrelated measurement noises [97].

To model the visual-evoked HR, we use linear basis function modeling. Given the limited scope of our pilot data, we employ a fixed canonical shape HR function [104–106], a model commonly utilized in fMRI [96] and fNIRS [97,98]. This function models the impulse HR response to neuronal activation, as demonstrated in Figure 3.7a. The impulse response is convolved with our photostimulation sequence, forming the basis function, as shown in Figure 3.7b.

The HR is then modeled as a linear combination of a basis set, following standard methods [100,107–111]. The model is expressed as:

$$y_t = \hat{\beta}_0 + \hat{\beta}_1 \mathrm{x}_t + \hat{\beta}_2 \frac{\partial \mathrm{x}_t}{\partial t} + \hat{\beta}_3 \frac{\partial^2 \mathrm{x}_t}{\partial^2 \mathrm{t}} + \varepsilon_t.$$

where $\hat{\beta}_0$ is a constant bias, $\hat{\beta}_1 \mathrm{x}_t + \hat{\beta}_2 \frac{\partial \mathrm{x}_t}{\partial t} + \hat{\beta}_3 \frac{\partial^2 \mathrm{x}_t}{\partial^2 \mathrm{t}}$ represents the second-order Taylor expansion of the basis function, and ε_t is a noise term. Considering that some mouse strains with visual impairments exhibit delayed responses, we fit the temporal traces at each pixel in the PA image to a series of basis sets with 1-second shifts by adjusting $\widehat{\beta_t}$. The basis set yielding the least fitting error and the lowest p-value in the linear fit is selected as the isolated HR, as shown in the red trace in Figure 3.7c.

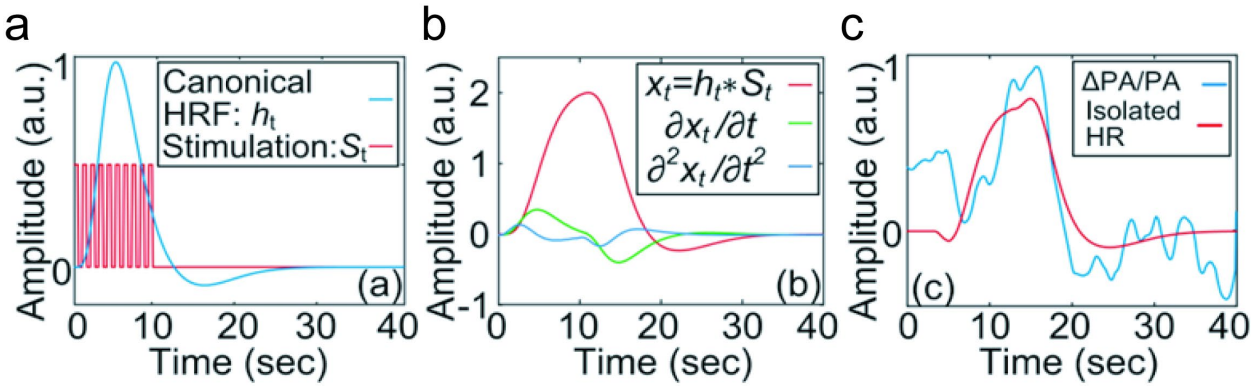

Figure 3.7: HR isolation from PA signals. (a) Canonical function and visual stimulation sequence. (b) A basis set derived from a. (c) Temporal trace in PA image and the isolated HR.

3.3 Results

This section offers a detailed examination of hemodynamic responses in the mouse brain, using PACT. Our findings, derived from a complete analysis involving wild-type, *rd1*, and mel-ko mice, provide new insights into the neural correlates of visual stimulation. We have successfully applied correlation mapping and functional mapping techniques to isolate and evaluate these responses across various brain regions. Notably, the results reveal significant differences in the

visual-evoked HR among the three mouse strains. These differences are especially noticeable in key areas such as the V1 and subcortical nuclei, such as SCN. It underscores the potential of PACT in advancing our understanding of neural mechanisms.

3.3.1 Pair-wise Correlation Map

In Figure 3.6d, a typical correlation map derived from a wild-type mouse during the visual stimulation process is depicted. The map's symmetry along the brain's midline reflects the pair-wise correlation of pixels equidistant from this central line. When examining major cortical areas, such as the motor, somatosensory, auditory, and primary visual cortices, it was observed that predominantly the primary visual cortex (V1) exhibited correlation coefficients above 0.2 across most of its extent. Figure 3.6e presents the temporal traces from areas in both hemispheres where these high correlation coefficients were found. The resultant hemodynamic responses were substantially more pronounced than the average responses observed in V1 (shown in Figure 3.6f), underscoring the efficacy of this correlation mapping technique.

3.3.2 Retinal Photostimulation Procedure and Time-lapsed Correlation Maps

Figure 3.8 outlines the sequence followed during retinal photostimulation and depicts time-lapsed correlation maps derived from wild-type mice at various stages of the process, as seen in Figure 3.8b. Since the differences in PACT images across the different time points were not considerable, correlation maps were employed to visualize the effects of stimulation over time. Prior to stimulation, lower correlation coefficients were noted in the initial two time points. At the height of stimulation (time point 3), the V1 area exhibited the highest correlation, which then

subsided soon after the stimulation ceased (time point 4). Ten minutes post-stimulation (time point 5), the correlation values across all observed areas had reverted to levels akin to those before stimulation.

In comparing the correlation maps of wild-type and *rd1* mice (illustrated in Figure 3.8b and c), both groups exhibited similar trends in correlation map fluctuations throughout the experiment. The primary distinction between the two was the reduced magnitude of peak correlation coefficients in the *rd1* mice compared to their wild-type counterparts. It can be attributed to the differences in their temporal trace amplitudes. In *rd1* mice, the amplitudes of the temporal traces were notably lower, thereby closely approximating the amplitude levels of background noise. This proximity in amplitude to the noise levels inherently reduced the signal-to-noise ratio in the *rd1* mice. As a consequence, the hemodynamic responses in these mice were more likely to be obscured by the surrounding noise, leading to reduced correlations in the response.

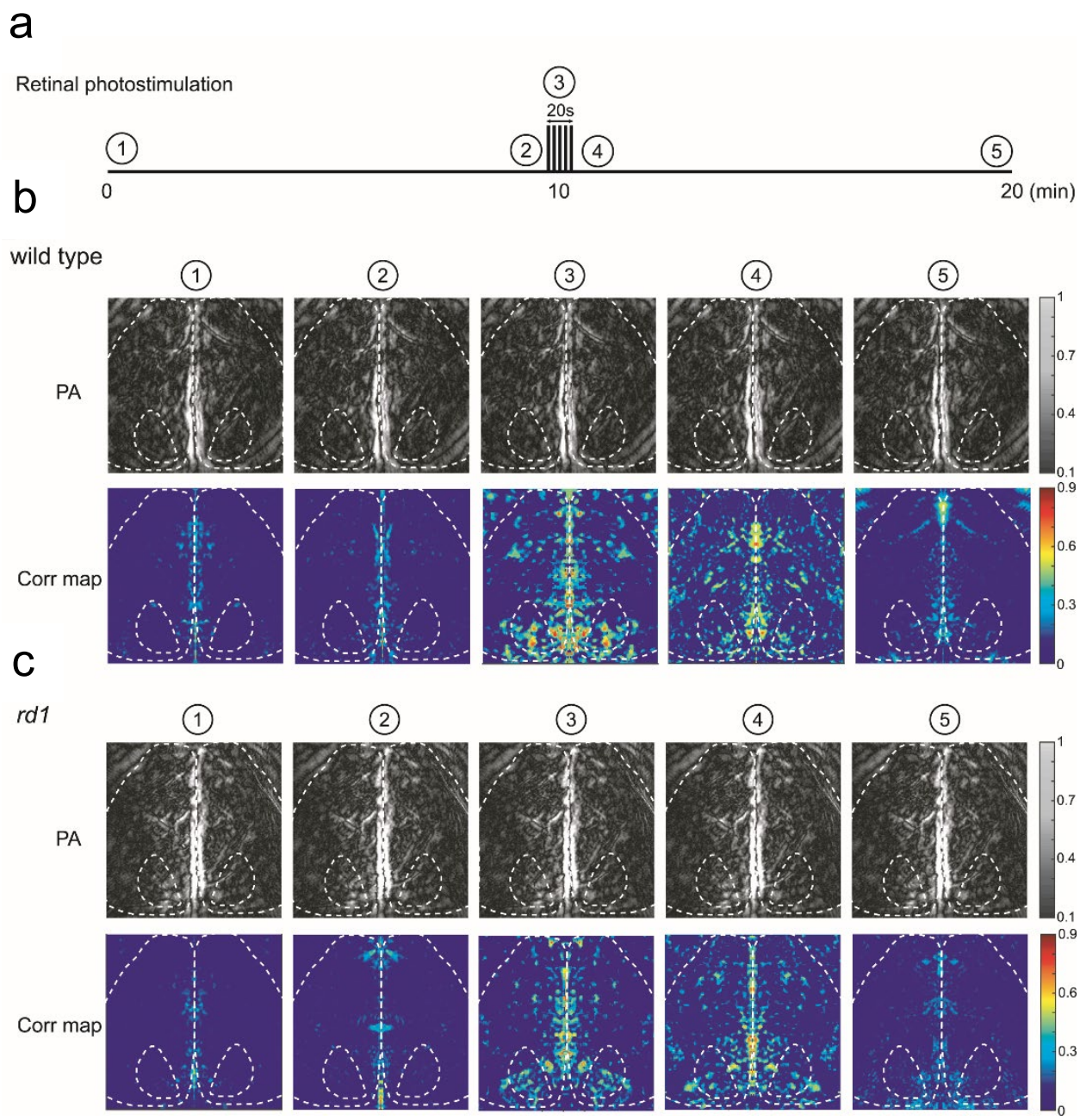

Figure 3.8: The timeline of retinal photostimulation and the corresponding pair-wise correlation maps at each time point for wild-type and *rd1* mice. (a) Each time point is a 1-min period. Time point 1: pre-stimulation (0m0s-1m0s); time point 2: shortly before the stimulation (8m40s-9m40s); time point 3: during the stimulation, including 20 sec of pre-stimulation, 20 sec of flickering stimulus, and 20 sec of post-stimulation (9m40s-10m40s); time point 4: shortly after the stimulation (10m40s-11m40s); time point 5: post-stimulation (19m-20m). (b) Average photoacoustic images and pair-wise correlation maps of wild-type and (c) *rd1* mice at each time point.

3.3.3 Temporal Traces of Visual-Evoked Hemodynamic Changes in the Primary Visual Cortex

Our imaging study encompassed 3 male and 3 female wild-type mice, alongside an equal number of male and female *rd1* mice. Figure 3.9a and b show the temporal hemodynamic change traces at V1 locations with the highest left-right correlation coefficients for each mouse. Population-averaged temporal traces for all 6 wild-type and 6 *rd1* mice are presented in Figure 3.9c and d, respectively. Notable inter-individual variations were observed, with wild-type mice generally displaying larger response amplitudes and quicker peak latencies (ranging approximately from 5 to 15 seconds in wild-types, compared to about 10 to 35 seconds in *rd1* mice).

A two-tailed Student's t-test affirmed the statistical significance of these disparities, yielding p-values of 0.0075 for response amplitude and less than 0.001 for peak latency (Figure 3.10a). Figure 3.10b demonstrates that response amplitudes and peak latencies were comparably distributed across both genders in both wild-type and *rd1* mice.

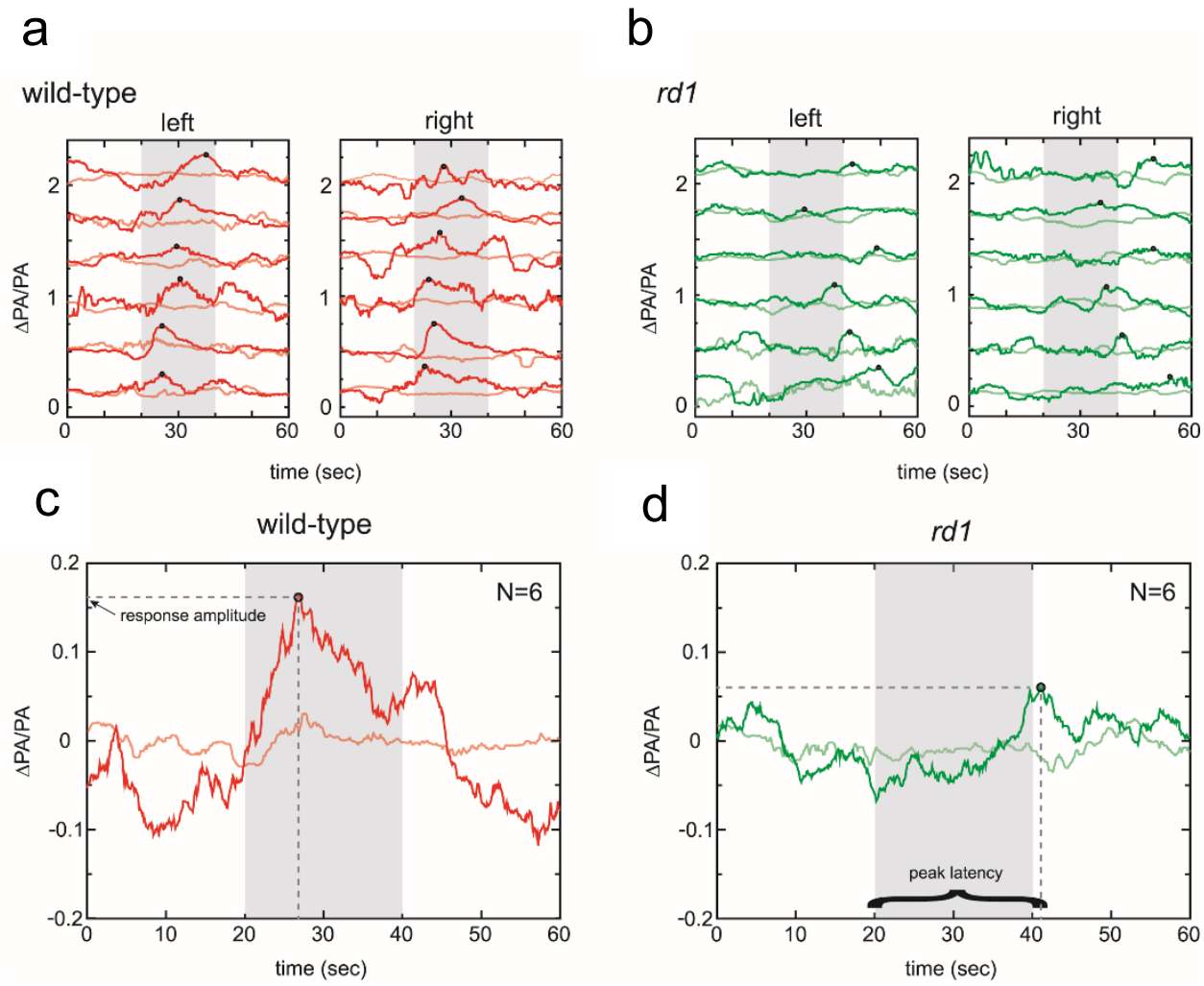

Figure 3.9: PACT of visual-evoked hemodynamic change *in vivo* using the full-ring array system. (a, b) The individual temporal traces of the background-subtracted and normalized PA signals (ΔPA/PA) for a single pixel located in V1 on both left and right hemispheres from wild-type and *rd1* mice. (c, d) The mean temporal trace of ΔPA/PA for single pixels located in V1 from both left and right hemispheres of 6 wild-type mice and 6 *rd1* mice. Dark control recordings obtained without photostimulation are shown in light red or light green. Shaded areas represent the period of stimulation. The red and green dots indicate the peak responses for the calculation of response amplitudes and peak latencies. The response amplitude was calculated by measuring the difference between the peak intensity and the mean pre-stimulation intensity. The peak latency was calculated from the time when the signal reached the maximum intensity after the onset of photostimulation.

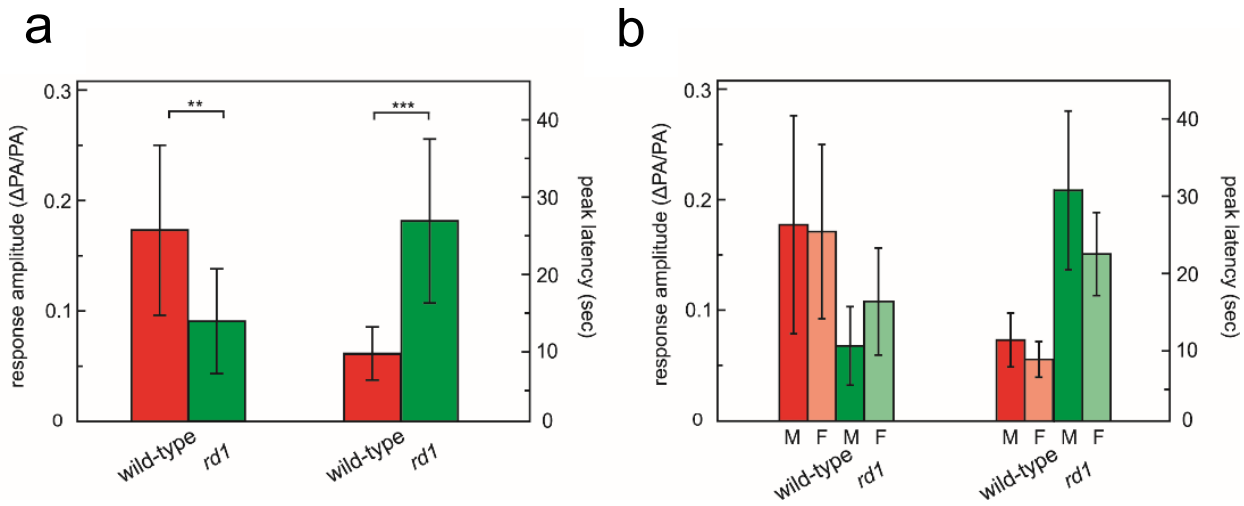

Figure 3.10: Statistical analysis. (a) Comparing the response amplitude and peak latency for wild-type and *rd1* mice. **, $p<0.01$ (n = 6,6); ***, $p<0.005$ (n = 6,6); (b) Comparisons between male and female wild-type and *rd1* mice.

3.3.4 Functional Maps of Visual-Evoked Hemodynamic Changes

After demonstrating the capability of our PACT system for characterizing the hemodynamic changes in the primary visual cortex, the alternative PACT system using linear array (GE L8-18i) was used to monitor all the targeted nuclei, including V1, SC, LGd, OPN, SCN, as shown in Figure 3.5.

Due to the higher sensitivity of the linear array used in the system, pair-wise correlation maps were not required for obtaining the hemodynamic changes at the nuclei. Instead, functional maps were obtained by calculating the relative variations of the averaged signal amplitude in each pixel of the temporal PA images during stimulation (20-30 sec) compared to the averaged signal amplitude before stimulation (0-20 sec).The relative variations were marked on the US images, showing areas with hemodynamic changes during retinal photostimulation (Figure 3.11), which match with the positions of the nuclei.

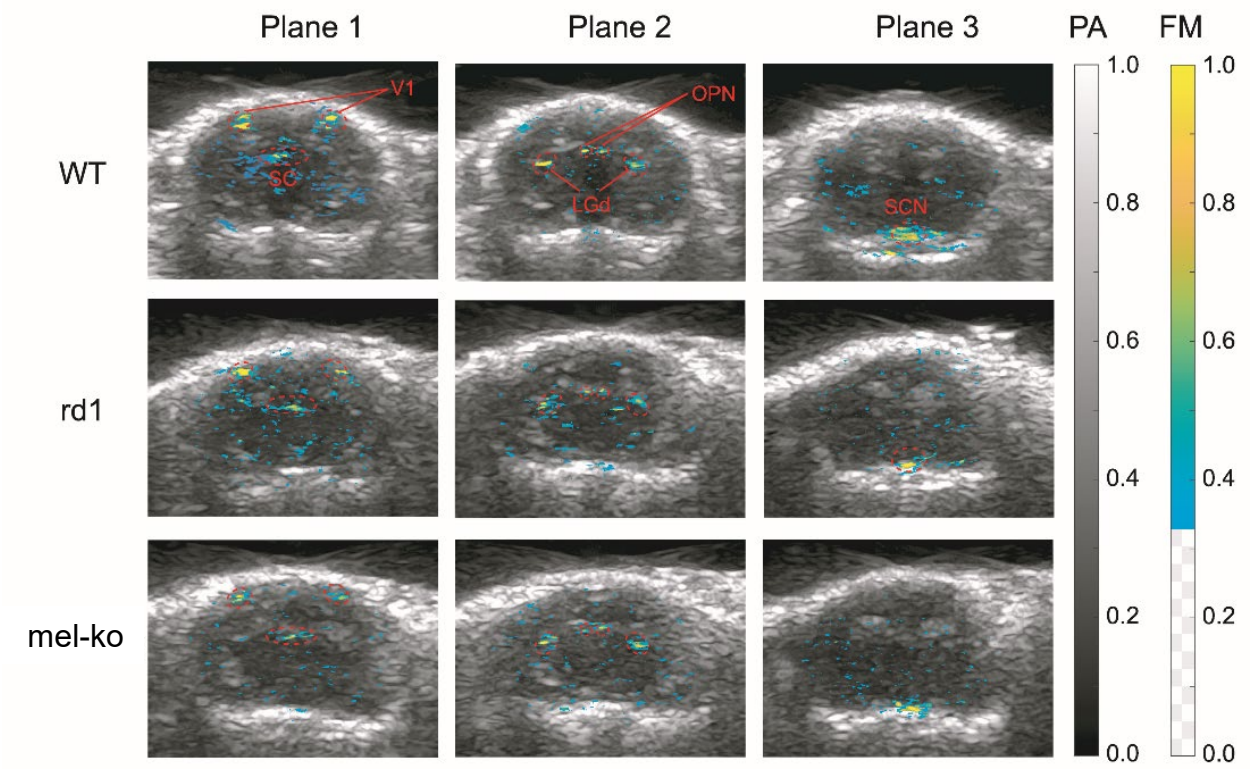

Figure 3.11: The visual-evoked functional maps of the mouse brain of different strains, wild-type (WT), *rd1*, and mel-ko, for the 3 imaging planes overlapped on the US images.

3.3.5 Temporal traces of Visual-Evoked Hemodynamic Changes in All Targeted Nuclei

The visual-evoked temporal traces extracted from the targeted nuclei are shown in Figure 3.12, and the average isolated HRs using the method described in section 3.2.7 are shown in Figure 3.13. The data were obtained from 10 wild-type, 10 *rd1*, and 10 mel-ko mice. The findings for V1

are consistent with those presented in Figure 3.9c and d. Both *rd1* and mel-ko also show deficits in the subcortical nuclei.

Our study pays particular attention to SCN, as it is deeply situated in the brain and presents significant imaging challenges. The results regarding SCN align with the expectations:

(1) Since the SCN predominantly receives ipRGC input [112–114], mel-ko had lower-amplitude SCN photoresponses than wild-type.

(2) The residual responses in mel-ko were driven by rod/cone input to ipRGCs and thus not significantly delayed compared to wild-type.

(3) *rd1*, using only melanopsin which responds to light sluggishly [115], showed both smaller and slower responses.

Statistical analysis using the method described in section 3.3.3 was also conducted (Figure 3.14). The response amplitude was calculated by measuring the difference between the peak intensity and the mean pre-stimulation intensity, and the peak latency was calculated from the time when the signal reached the maximum intensity after the onset of photostimulation. In all of the targeted nuclei, the response amplitudes of both *rd1* and mel-ko mice were significantly lower than wild-type mice, but only *rd1* mice had slower response latency compared to wild-type mice.

However, it is worth noting that in some instances, the *rd1* and mel-ko curves began to rise before the initiation of stimulation. This phenomenon can be attributed to the low amplitude of the responses in mel-ko mice. Even after averaging across subjects, these response amplitudes remained low, making them less distinct from the background noise. As a result, the influence of noise becomes more prominent in the data, potentially leading to a premature rise in the response

curve. It shows the necessity of optimizing the experimental settings or employing noise reduction techniques to accurately interpret the weaker responses from the genetically deficit models.

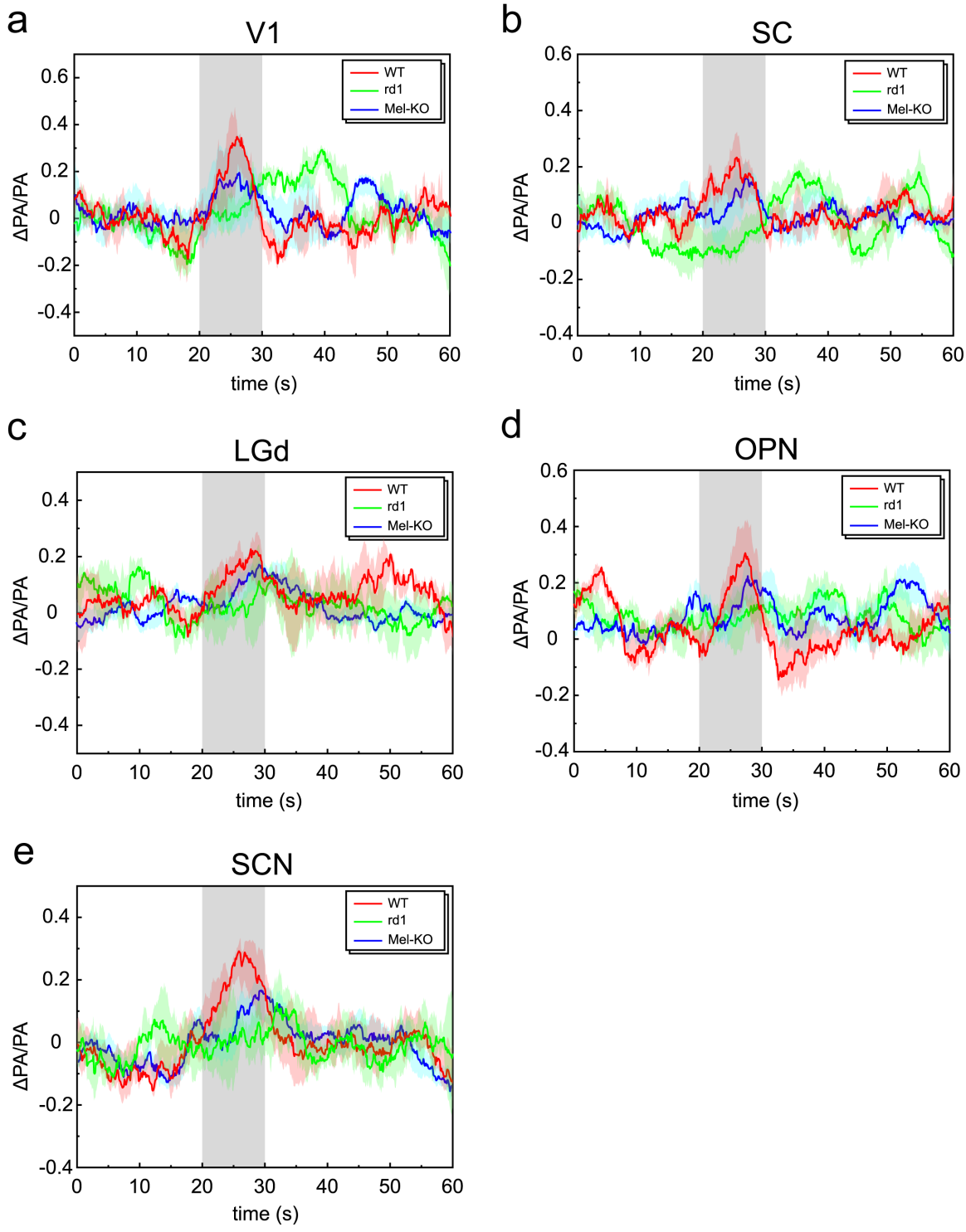

Figure 3.12: Visual-evoked hemodynamic changes in *rd1* mice and mel-ko mice compared with those in wild-type mice. The mean temporal traces of the background-subtracted and normalized PA signals (ΔPA/PA) for single pixels with the highest functional changes located in the targeted nuclei (a-e) of 10 wild-type mice (red), 10 *rd1* mice (green), and 10 mel-ko mice (blue). The standard deviations of the temporal traces are shown as the upper and lower bound of the traces. Shaded areas represent the period of stimulation.

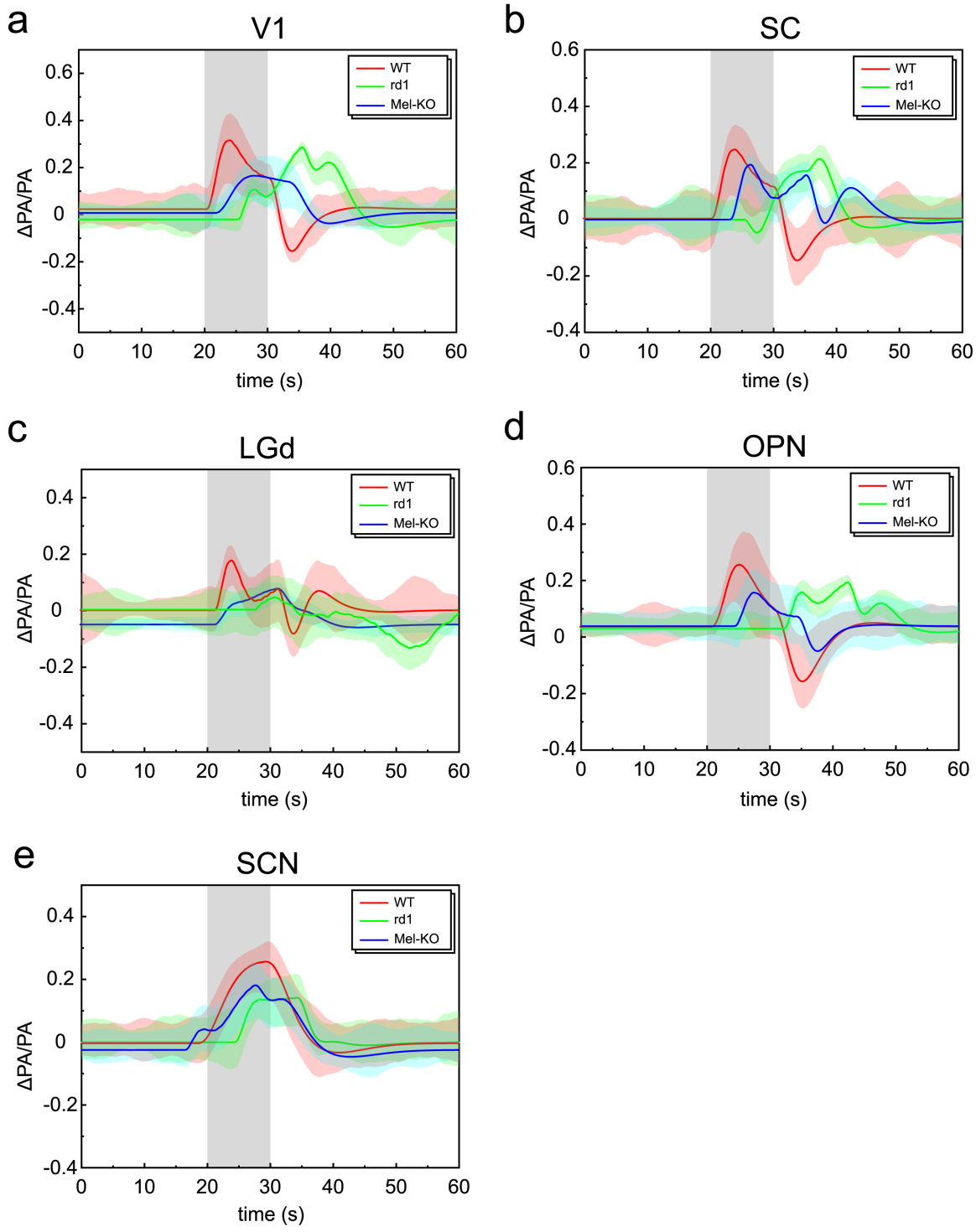

Figure 3.13: Isolated visual-evoked HR in *rd1* mice and mel-ko mice compared with those in wild-type mice. The mean HR located in the targeted nuclei (a-e) of 10 wild-type mice (red), 10 *rd1* mice (green), and 10 mel-ko mice (blue). The standard deviations of the temporal traces are shown as the upper and lower bound of the traces. Shaded areas represent the period of stimulation.

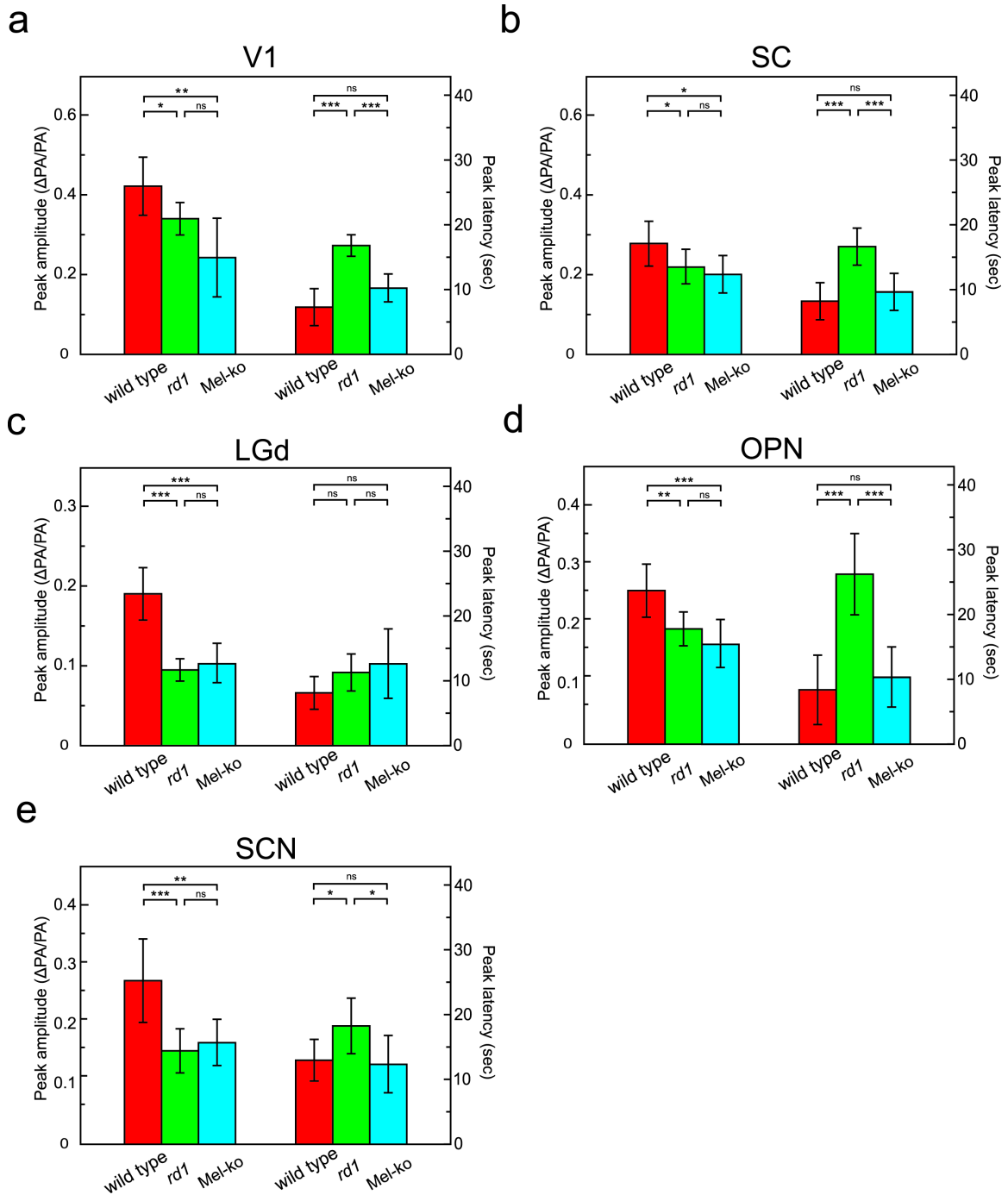

Figure 3.14: Statistical analysis. Comparing the response amplitude and peak latency of the targeted nuclei (a-e) for wild-type, *rd1*, and mel-ko mice. *, $p<0.05$ (n = 10,10); **, $p<0.01$ (n = 10,10); ***, $p<0.005$ (n = 10,10).

3.4 Discussion and Conclusions

The approach employed in this investigation effectively delineated the visual cortical and subcortical responses induced by retinal photostimulation within the mouse brain. Despite the initial low signal-to-noise ratio of the PA signals, the application of bilateral correlation mapping proved effective in pinpointing cortical regions undergoing visually induced hemodynamic changes. Quantitative evaluation of temporal traces from these identified regions revealed apparent differences between wild-type mice, *rd1* mice, and mel-ko mice. Notably, *rd1* mice, which rely solely on melanopsin for light detection due to the absence of rod/cone photoreceptors, exhibited both weakened and delayed hemodynamic responses, while mel-ko mice only shows weakened responses. This observation aligns with prior electrophysiological data gathered from retinal ganglion cells and visual thalamic recordings, underscoring the potential of this imaging technique in facilitating less invasive cortical assessments in vision-related research.

Future enhancements to the system could include the integration of a laser with elevated repetition rates, potentially elevating the sampling frame rates to align with those seen in electrophysiological studies, potentially reaching up to 10 kHz. Although the hemodynamic responses we are monitoring are relatively slow, there are specific advantages to this enhancement. Firstly, a higher sampling rate provides a more detailed temporal resolution of the hemodynamic response, allowing for the observation of subtle dynamics within these slow response curves. These finer details, though seemingly minor, can be crucial in understanding the complex interplay of neuronal and vascular activities. Furthermore, a high sampling rate is essential for effective synchronization with other high-frequency neuroimaging modalities. In particular, recent research has employed genetically encoded calcium indicators like GCaMP6f for calcium imaging in conjunction with PACT. This approach is intended to capture neuronal responses, which can occur

at much faster timescales than hemodynamic changes. The ability to simultaneously record both neuronal and vascular dynamics at high temporal resolution can offer a more comprehensive understanding of neurovascular coupling and brain function. Thus, while the primary focus has been on slower hemodynamic responses, the potential to capture and synchronize with faster neuronal events makes the case for a higher sampling frame rate compelling. Additionally, the system could be optimized to discern changes in blood oxygenation (sO2) using multi-wavelength imaging setup, offering an alternative metric for cortical response assessment.

A notable feature in the correlation maps is the consistently illuminated central line, as seen in Figure 3.6C and Figure 3.8. This phenomenon arises due to the division of the superior sagittal sinus, located centrally in the brain, thereby affirming the reliability of our methodology. However, one constraint of this bilateral correlation approach is its basis on the simultaneous photostimulation of both eyes, which may necessitate modifications when exploring disease models characterized by unilateral vision impairment. Therefore, a US array with high sensitivity is crucial in order to avoid the use of correlation maps, which has been demonstrated with our alternative PACT system with a more highly sensitive linear array.

In comparing the temporal traces of hemodynamic responses obtained from our PACT systems with fMRI results reported in the literature [14], a notable difference is observed in the noise levels. Our PA imaging data exhibits relatively higher noise compared to the flatter averaged baseline in fMRI results. This discrepancy can be attributed to several factors inherent to the PA imaging process and the experimental setup. Firstly, the number of subjects used in our study – 6 and 10 for the two PACT systems – while substantial, could be increased to enhance the reliability of the data through averaging. Secondly, inherent fluctuations and jittering in laser output, with a 5% variation in laser energy, contribute to the noise. Implementing a dichroic mirror to measure

laser energy in real-time and compensating accordingly could mitigate this effect. Lastly, the potential for tissue heating poses a significant consideration. The increase in local brain tissue temperature, even within ANSI safety limits, may amplify PA signals, contributing to background noise. This is particularly relevant considering the experimental setup involving scalp removal and skull thinning, which suggests that a lower safety threshold might be applicable for brain tissue exposure. Moreover, ANSI safety limits, which are tailored for human retina and skin, are often adopted as a benchmark in animal research. However, it is crucial to consider that mouse models, due to their distinct physiological characteristics, may have lower safety thresholds compared to humans. Future experiments will aim to reduce laser energy to assess its impact on noise levels. Such refinements in methodology are essential for enhancing the accuracy and applicability of PACT in neuroscientific research, particularly in studies paralleling those conducted using fMRI.

In conclusion, this study has established label-free, high-resolution PACT systems, capable of real-time imaging of the mouse brain and monitoring hemodynamic responses across different brain regions. The system has successfully identified hemodynamic changes in V1, SC, LGd, OPN, SCN in response to retinal photostimulation, while other areas largely remained inactive. Comparisons between the responses in *rd1* and mel-ko mice, and wild-type mice validate the sensitivity of this technique in discerning significant variances in response amplitudes and latencies. Such findings highlight the potential of our system to elucidate the connections between initial visual processing in the retina and more complex visual responses within the cortex.

Chapter 4 Photoacoustic Imaging of Non-human Primate Brains

4.1 Introduction

In this chapter, we focus on the application of photoacoustic computed tomography (PACT) and photoacoustic microscopy (PAM) in non-human primate (NHP) models, an area that holds immense potential for bridging the gap between small animal studies and human clinical research. NHPs, with their close physiological and anatomical similarities to humans, provide an invaluable platform for advancing our understanding of complex neural mechanisms and pathologies. The transition from mouse models to NHPs in photoacoustic (PA) imaging (PAI) represents a significant leap, bringing us closer to translating these techniques into clinical settings.

The complexity of the primate brain, coupled with the advanced cognitive abilities it supports, offers a prospect for exploring neurobiological questions that are directly relevant to human health and disease. Through PACT and PAM, we can obtain detailed insights into cerebral hemodynamics in primate brains. These techniques offer a unique combination of depth, resolution, and functional information, making them ideal for studying the primate brain's intricate structure and function.

This chapter also highlights the significant contributions of various experts in the field, ensuring a comprehensive and multidisciplinary approach. The preparation and mapping of the non-human primate cortex, along with the precise execution of peripheral electrical and mechanical stimulation, were meticulously carried out by experienced surgeons from the University of Kansas Medical Center, including Dr. Heather M. Hudson, Dr. Scott Barbay, Dr.

David Bundy, Dr. David J. Guggenmos, and Dr. Shawn Frost from Prof. Randolph J. Nudo's research group. Their expertise in surgical and neurological procedures was instrumental in the successful execution of these complex experiments. Furthermore, the sophisticated analysis involving the fully connected neural network (FCNN), which played a pivotal role in interpreting the photoacoustic microscopy data, was adeptly handled by Madhumithra Subramanian Karthikesh from the University of Kansas, a member of Dr. Xinmai Yang's research group. Their profound understanding of computational neuroscience and neural networks significantly enhanced the accuracy and relevance of our findings. The collaboration between these groups epitomizes the multidisciplinary nature of this research, bridging the gap between clinical expertise, neuroscientific inquiry, and advanced computational analysis. It enriches our understanding of primate neurobiology and paves the way for future innovations in clinical imaging technologies.

4.2 Material and Methods

4.2.1 Non-human Primate Preparation

This study involved two adult squirrel monkeys (Saimiri scuireus), estimated to be 12-15 years old. The experimental procedures adhered to the guidelines approved by the Institutional Care and Use Committee at the University of Kansas. The mapping and imaging tasks were conducted during a single session with the animals under anesthesia. After the completion of these procedures, the monkeys were euthanized in a humane manner, followed by post-mortem examinations.

4.2.2 Surgical Procedures

The squirrel monkeys were initially sedated with ketamine (20-30 mg/kg intramuscularly) and atropine (0.04 to 0.07 mg/kg intramuscularly), followed by preparation for the surgical procedure, which involved shaving the head and forelimbs. The animals were then intubated, and a combination of 70% nitrous oxide and 30% oxygen with 0.5-3% isoflurane was administered through gas anesthesia, maintained throughout the cranial surgery. Intravenous access was established via the saphenous vein for fluid administration, consisting of 10 ml/kg/hr of lactated Ringers supplemented with 3% dextrose. Additional ketamine doses ranging from 10-60 mg/kg/hr were given intravenously in 2-6 mg boluses as required to sustain a consistent level of anesthesia. The monkeys' heads were immobilized using a stereotaxic frame with earbars (Model 1430 Stereotaxic Frame, Kopf). Prophylactic penicillin (G benzathine and G procaine 45,000 IU subcutaneously) was administered. The incision site was treated with bupivacaine (0.5-1.0 cc) for local anesthesia and Mannitol (0.75 to 2 g/kg intravenously). Surgery commenced once vital signs, including body temperature, stabilized. The procedure involved making an incision in the scalp over the right hemisphere, cutting the temporalis muscle insertion, and removing a section of the skull over the somatosensory and motor cortex. After excising and removing the dura, a plastic cylinder (inner diameter: 2.5 cm) was secured around the cranial opening using dental acrylic.

4.2.3 Motor Area Mapping

To locate the motor regions of interest, including the primary motor cortex (M1), dorsal premotor cortex (PMd), and ventral premotor cortex (PMv), we employed established intracortical microstimulation (ICMS) techniques [116–118]. A fine plastic ruler with 250 μm divisions was positioned on the cortical surface, and the area was covered with warm, sterile silicone oil to

prevent desiccation and facilitate electrode insertion. We captured a digital image of the cortical surface's vascular layout through a surgical microscope, covering the entire cranial opening. This image was then loaded into a graphic software program (Canvas GFX Inc., Boston, MA), where we calibrated the distance to match the cortical ruler and overlaid a 250 μm grid onto the vascular image. Additional layers on the software were used to record responses to microstimulation.

For the microelectrode, we used a finely pulled glass micropipette, tapered to a 15-20 μm outer diameter tip and sharply beveled, filled with 3.5M NaCl and equipped with a tungsten wire. This electrode was systematically inserted into the cortex at intersections on the grid, using the vascular pattern as a reference point, to a depth of approximately 1750 μm ± 10 μm. At each insertion point, we used a constant current stimulus isolator (Bak Electronics, Inc., Umatilla, FL) to deliver a train of stimuli (13 pulses of 200 μs duration pseudo-biphasic square waves at 330 Hz) at 1 Hz intervals. These stimuli were visually observed for motor outputs. The stimulation was connected to an audio amplifier, allowing for a visual correlation between stimulation pulse trains and movements. The current was incrementally increased from 0 μA, with a maximum limit of 30 μA, until a movement around a joint was detected, and the type of movement was then noted on the digital image. The forelimb motor representations for the primary and premotor cortex were mapped at approximately 500 μm resolution, except at boundary areas or to distinguish M1 from PMd, where mapping was conducted at finer resolutions of 250-350 μm.

4.2.4 Somatosensory Area Mapping

For the somatosensory mapping in S1, we utilized microelectrode techniques to record multiunit neuronal activity, delineating cutaneous and muscle/joint fields in areas 3a, 3b, and 1/2 [119–121]. The identical digital image utilized for motor mapping was repurposed to align cortical

surface locations for the somatosensory maps. A 16-channel, single-shank Michigan-style probe (NeuroNexus Technologies part no. A1x16-100-703, Ann Arbor, MI), connected to a unity-gain headstage and a digitizing amplifier (Tucker-Davis Technologies, Alachua, FL), was inserted into the somatosensory areas at approximately 1700 μA to cover the entire cortical column at each site. The neural signals were relayed to a computer workstation, where they underwent real-time filtering and were amplified for auditory monitoring.

From the action potentials observed on each channel, we selected one based on its activity rate and signal-to-noise ratio for sensory response assessment. Cutaneous receptive fields were pinpointed by identifying the skin area that, when gently indented with a fine glass probe, elicited cortical neuron activation. Deep receptive fields were determined through high-threshold stimulation and joint manipulation. We conducted a two-row rostral-caudal recording across D1 and D5 brain regions, extending from area 3a to area 2. This approach facilitated precise identification of boundaries between the various somatosensory areas.

4.2.5 Peripheral Electrical and Mechanical Stimulation

To induce a peripheral electrical response for imaging, pairs of 30 ga needle electrodes were subcutaneously inserted on the medial and lateral aspects of digit 2 parallel to the distal phalanges in each hand. These electrodes were linked to a constant current stimulus isolator (Bak Electronics, Inc., Umatilla, FL). In each trial, one digit received stimulation through monophasic anodal pulses of 200 μs duration at a frequency of 1 Hz, lasting for 20 seconds, at an amplitude of either 3 or 8 mA, with current flowing from the lateral to the medial electrode. Notably, no reflex movements were observed in response to these stimulation levels.

For the mechanical stimulation aspect, the forelimb digits D1 and D5 were activated using a small solenoid. This solenoid was controlled by a computer-synchronized signal, which generated a 200 ms tap on the distal pad at a frequency of 1 Hz, continuing for 20 seconds. PAM images were captured either at the onset of mechanical stimulation or after a 10-second duration.

4.2.6 PACT and PAM System

Figure 4.1A illustrates the design of the PACT system utilizing a linear array for imaging the squirrel monkey brain. The setup featured an Nd:YAG laser (Surelight SLIII-10, Continuum, Santa Clara, CA) coupled with an optical parametric oscillator (OPO) (SLOPO Plus, Continuum, Santa Clara, CA) as the excitation source. This setup generated pulses with a duration of 4-6 ns at a repetition rate of 10 Hz. The laser, operating at a wavelength of 797 nm, was channeled through a bifurcated multimode fiber bundle, with the fiber tips positioned on either side of a linear 128-element ultrasonic array (Verasonics L22-14v) with a central frequency of 15.6 MHz. The peak light intensity at the brain's surface was kept under ~20 mJ/cm2, well within the safety limit of 31 mJ/cm2 at 797 nm set by the American National Standards Institute (ANSI). The PA signals generated were captured by the ultrasonic array positioned vertically above the exposed right hemisphere, producing images in a coronal view. These signals were processed using a Vantage 128 ultrasound research system (Verasonics, Redmond, WA). The PACT system boasted an axial resolution of 200 μm and a lateral resolution of 400 μm within a 2-cm depth.

For the PAM system depicted in Figure 4.1B, the excitation light at 532 nm was produced by a Q-switched diode-pumped solid-state (DPSS) laser (Elforlight Model SPOT-10-200-532, Bozeman, MT). This system had a pulse duration of 1.5 ns and a high pulse repetition rate of 10 kHz, with each pulse carrying an energy of 50 nJ. The light was concentrated through an objective

lens (AC127-050-A, Thorlabs, Inc) onto the brain's surface, creating a focal spot of 20 μm in diameter. A custom-programmed Galvo mirror system facilitated a scanning area of 5mm × 5mm (256 × 256 pixels). Nearby, a calibrated needle hydrophone (HNC1500, ONDA Corp.) was positioned to detect the ensuing PA signals . The PAM system's temporal resolution was set at 10 seconds.

Both the 797 nm wavelength used in PACT and the 532 nm wavelength in PAM are isosbestic points, where the optical absorption of deoxyhemoglobin and oxyhemoglobin is identical [33].

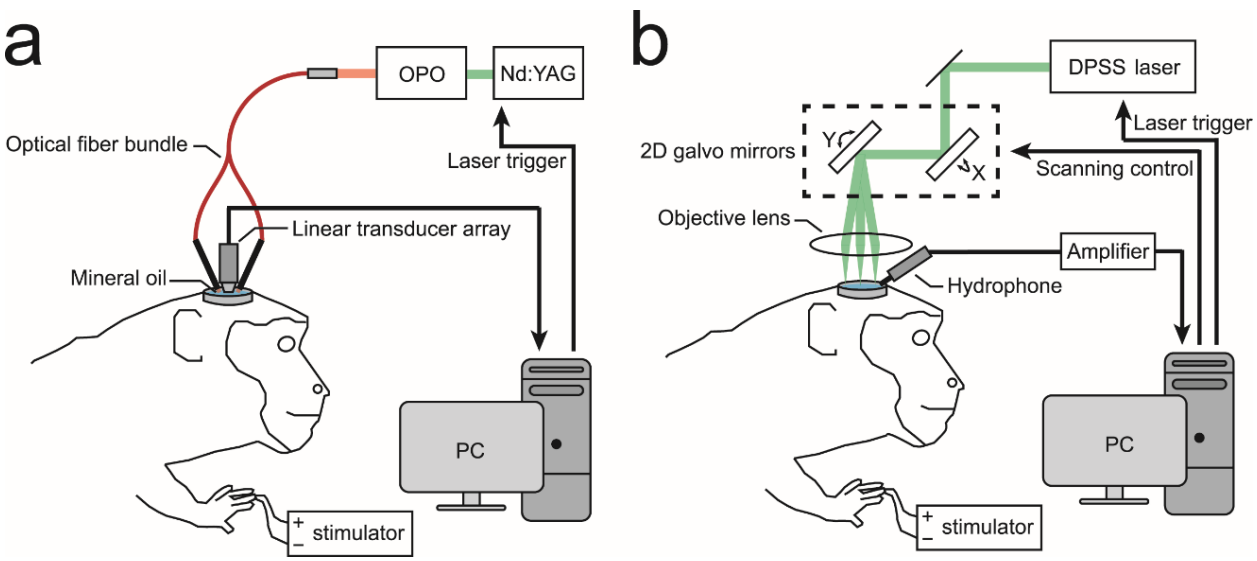

Figure 4.1: Schematic diagrams of the photoacoustic imaging (PAI) system for squirrel monkeys with peripheral electrical stimulation. (a) Photoacoustic tomography (PACT) system. (b) Photoacoustic microscopy (PAM) system.

4.2.7 Image Reconstruction and Signal Processing

In each experiment, the PACT system captured brain signals of the squirrel monkey over a one-minute duration, encompassing 30 seconds before the stimulation, 20 seconds during stimulation, and 10 seconds following it. This process generated a series of 600 frames, forming a

time-lapse PA recording. This one-minute PA footage was methodically cross-correlated on a frame-by-frame basis, with adjustments made for any vertical movements caused by the monkey's breathing [122,123]. For every pixel, a temporal trace was extracted from this PA sequence. Initially, the trace underwent detrending by subtracting its pre-stimulation linear trend, effectively eliminating any systematic shifts in the detected signal. Subsequently, this adjusted trace was normalized against the root-mean-square of the signal strength observed in the pre-stimulation phase, resulting in what is referred to as the baseline-subtracted and normalized PA signals ($\Delta PA/PA$). To further refine the data, a spatial average was calculated over a 3×3 pixel area, coupled with a temporal forward-moving average spanning 25 frames (equivalent to 2.5 seconds), thus filtering out noise arising from random signal fluctuations.

For the PAM system, imaging was achieved by calculating the peak intensity of the ultrasound (US) waves received for each laser pulse, as detected by the needle hydrophone. These intensity values were then adjusted based on the hydrophone's directional response, taking into account the polar angles between the scan points and the transducer's orientation. The relative hemodynamic changes observed in the PAM system were quantified by subtracting the pre-stimulation image from the post-stimulation image, and then normalizing this difference against the pre-stimulation image. This approach allowed for a precise assessment of the hemodynamic variations following stimulation.

4.2.8 Magnetic Resonance Imaging of the Squirrel Monkey Brain

Following the completion of the experimental procedures, the squirrel monkey was humanely euthanized. Subsequently, the brain was extracted and preserved in 10% neutral buffered formalin (NBF) for further analysis. To align the PA images with specific

neuroanatomical structures, magnetic resonance imaging (MRI) was employed. The MRI scans of the monkey's brain were conducted using a 7T Bruker Biospec MRI scanner (Bruker Inc., Billerica, MA). These scans utilized a turbo spin-echo method (Rapid Acquisition with Refocused Echoes, RARE), with the following parameters: repetition time/echo time (TR/TE) set at 2000/90 milliseconds, averaging performed four times, a RARE factor of 8, and a matrix size of 256 × 256. The imaging covered a field of view measuring 3.30 cm by 3.30 cm and included 50 slices, each 1 mm thick. This process enabled the creation of detailed T2-weighted MRI images, which facilitated the precise co-registration of PA images with the corresponding brain structures.

4.2.9 Fully Connected Neural Network

In the process of transforming the two-dimensional PAM images into one-dimensional data, a four-layer fully connected neural network (FCNN) was employed. This FCNN comprised an input layer, three hidden layers, and an output layer, with the configuration being 4/256/128/256/4 [124] (as illustrated in Figure 4.2). The hidden layers were represented by l_n, $n = 1, \dots, N$ as:

$$l_n(\mathrm{y}) = \tau(b_n + W_n y),$$

where $b_n \epsilon\, R^{N_k}$ is the bias vector, and W_n is the output weight matrix.

Three hidden layers were determined to be optimal, and the number of nodes in each layer was chosen through a series of experimental procedures. The network's training employed the widely recognized supervised learning technique, backpropagation, which updated all the network's weights and biases. The learning rate was set at 0.01, and the training was conducted over 1000 epochs. The network utilized a nonlinear hyperbolic tangent activation function, represented as:

$$\tau(y) = tanh\,(y) = \frac{2}{1+e^{-2y}} - 1, y\epsilon(-\infty, +\infty)$$

The mean squared error served as the loss function, defined as:

$$O(\Psi) = \frac{1}{D}\sum_{u=1}^{D} \|\boldsymbol{\rho}(y_u; \Psi) - \boldsymbol{x}_u\|_2^2$$

For post-processing, the FCNN output images underwent enhancement to achieve a 3D effect. Initially, median filtering with a 3x3 mask was applied to eliminate any salt-and-pepper noise. The images were then rescaled and underwent contrast enhancement using the "imadjust" function to a [0,1] range. Subsequently, the edges detected through Canny edge detection were subtracted from the enhanced images, resulting in a pronounced 3D visual effect.

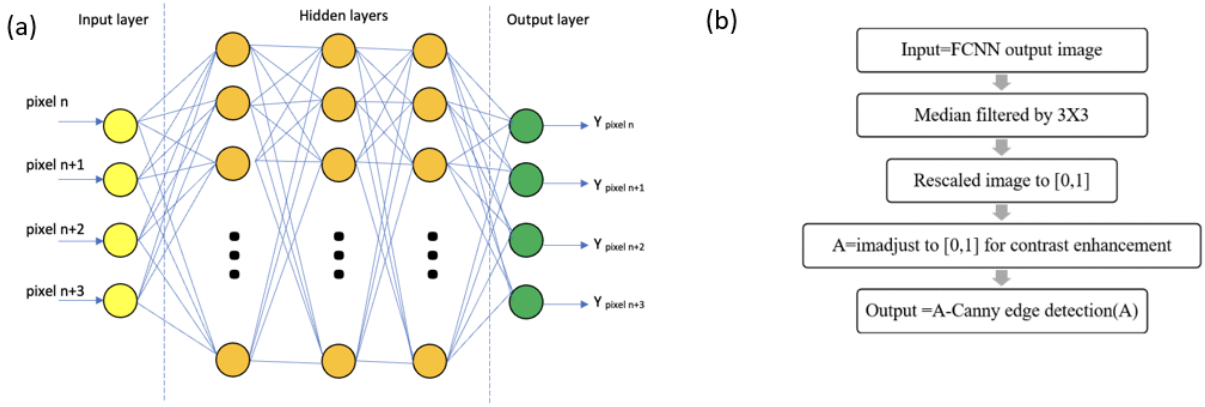

Figure 4.2: (a) The fully connected neural network (FCNN) model schematic. The input layer was the pixels of the original reconstructed PAM images and generated dataset. The output layer was the pixels of the processed PAM images and was compared with the digital images of the monkey cortical surface. (b) Post-processing after FCNN to add 3D effect.

4.2.10 Dataset Generation

For enhancing the dataset size of the PAM images obtained from the experiment, data augmentation techniques were employed, as the initial sample size was limited to nine images.

This set included one control image, along with two images taken immediately (0 sec) and two images taken ten seconds after the stimulation of both D1 and D5 digits. To augment the dataset, each PAM image was used to generate an additional hundred images. This was achieved by individually and collectively applying a variety of kernels, filters, and noise patterns [125–127].

For the training of the FCNN, a selection of 828 images was randomly chosen from the augmented dataset, while a distinct set of 81 samples, including the nine original images, was reserved for testing the network's performance. To ensure that the functional changes captured during the actual experiments were accurately reflected, the output for each training image was modeled as a composite of the training image and a binarized photograph image. This combination was set in a ratio of 17:3, carefully chosen to optimally preserve the original functional characteristics observed in the experiment.

4.2.11 Vessel Quantification

In order to quantify the enhancement in visualizing blood vessels, both the original and FCNN-enhanced PAM images underwent a comparison of vessel count and vessel area. Initially, all images were subjected to median filtering with a 3 × 3 kernel, effectively eliminating any present salt and pepper noise. Subsequently, the images were sharpened and underwent a dilation process magnified by a factor of two. The next step involved converting the images into binary format through a thresholding process. This threshold was determined by adding the mean and standard deviation of the pixel values for each image. Utilizing standard deviation around the mean as a thresholding technique is a common practice, aimed at removing outliers, and was thus applied in this study [128].

Following the thresholding, the images were skeletonized to extract vessel endpoints. This process allowed for the calculation of the vessel count. The vessel area was then determined based on the pixel area covered by the vessels, and this measure was normalized against the measurement area expressed in square millimeters. To ensure accuracy, the original photograph was used as a reference for validating both the vessel area and the vessel count derived from the processed images.

4.2.12 Quality and Repeatability of Hemodynamic Signals

To assess the improvement in image clarity and consistency of hemodynamic signals, specific evaluation metrics were employed, including the structural similarity index (SSIM), signal-to-noise ratio (SNR), and correlation coefficient (CC). The analysis utilized images acquired directly from PAM and those processed using the FCNN, without any further post-processing adjustments. The measurement of hemodynamic changes in the monkey's cortex, as captured by PAM, involved a straightforward subtraction of post-stimulation images from those taken prior to stimulation.

The analysis of the repeatability of PA signals within the same experimental group incorporated both the correlation coefficient and the structural similarity index. These measures were specifically applied to evaluate the consistency of the PA signals. Furthermore, the overall enhancement in image quality, particularly the clarity and definition of the images, was assessed using the SNR. This metric provided a quantifiable means to compare the relative improvements in image fidelity achieved through the FCNN processing.

4.2.13 Statistical Analysis

For the statistical evaluation of the data, a paired t-test was utilized. This analysis was conducted using the GraphPad Prism software (GraphPad Software, based in La Jolla, California, USA). The results were presented as the mean value with its corresponding standard deviation. A threshold of $p<0.05$ was established to determine the statistical significance of the findings.

4.3 Results

This section explores the results of using PACT and PAM to investigate the responses of squirrel monkey brains during electrical or mechanical stimulation. Our study delves into the real-time changes observed within the brain's cortical and subcortical regions, captured through PACT. By administering electrical stimulation, we were able to observe and analyze the resulting hemodynamic changes. Furthermore, we utilized PAM to zoom in on the primary somatosensory cortex, revealing detailed vascular structures and the subtle hemodynamic shifts during the stimulation.

Another advancement was the incorporation of FCNN to enhance the quality of our PAM images. This technology allowed us to significantly improve the signal-to-noise ratio and other indexes. This section, therefore, presents a comprehensive study of the cerebral hemodynamics observed in squirrel monkey brains under peripheral stimulations, enhanced through the latest imaging and processing technologies.

4.3.1 Real-time PACT of the Squirrel Monkey Brain In Vivo

Prior to utilizing the PACT system, the various cortical areas such as the ventral premotor (PMv) cortex, dorsal premotor (PMd) cortex, primary motor cortex (M1), and primary somatosensory cortex (S1), were delineated using intracortical microstimulation (ICMS). For the PACT experiments (as illustrated in Figure 4.1a), the linear US transducer was strategically positioned at three distinct locations on the right hemisphere, as shown in Figure 4.3a. This setup facilitated the acquisition of PA images in a coronal view, capturing distinct slices of the premotor cortices (slice 1), primary motor cortex (slice 2), and primary somatosensory cortex (slice 3) during peripheral electrical stimulation, depicted in Figure 4.3b-d. The subcortical region was precisely identified using T2-weighted MRI images, which were aligned with the stereotaxic atlas of the squirrel monkey brain [129]. Key regions on these slices were annotated, including the frontal gyrus (FG), precentral gyrus (PrG), postcentral gyrus (PoG), inferior parietal cortex (IPC), caudate nucleus (Ca), internal capsule (IC), putamen (Put), and thalamus (Th). PA signals, primarily emanating from hemoglobin, pinpointed blood vessel locations situated predominantly beneath each coronal slice in the subcortical areas. The images for each slice were generated with the US transducer positioned vertically to the brain surface, providing a unidirectional view of the imaging plane within the brain. Consequently, only the blood vessels aligned perpendicularly to the acoustic axis of the transducer were distinctly visible in the reconstructed images. Although other vessel structures might not be distinctly visualized, any enhancement in their PA signals was still detectable as an increase in the background intensity of the images.

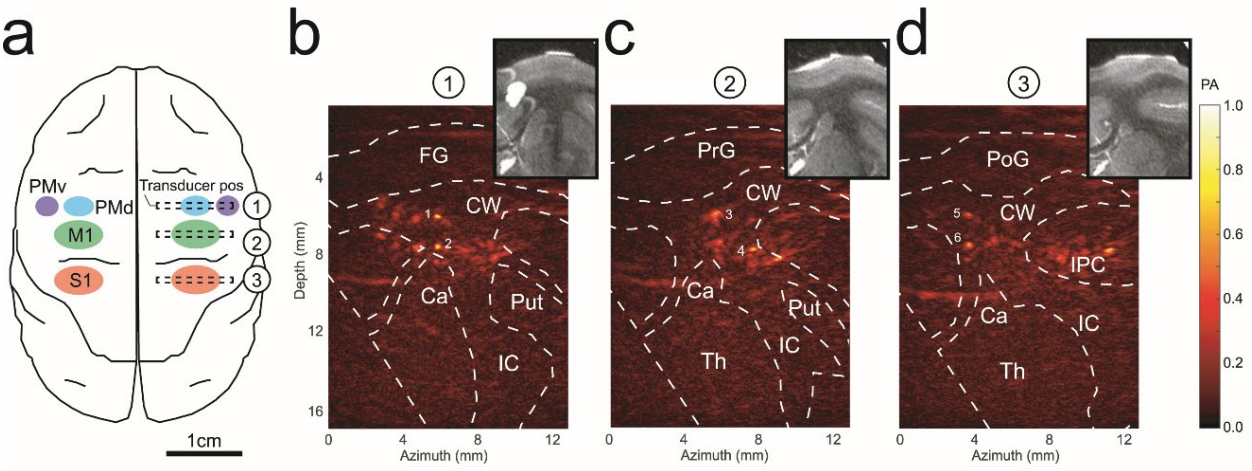

Figure 4.3: (a) Cerebral cortex regions including premotor cortex (PMd, PMv), primary motor cortex (M1) and primary somatosensory cortex (S1). (b) PACT images of the right hemisphere at PMd and PMv, (c) M1 and S1, and corresponding MRI images at each region. The transducer positions for (b-d) are shown in (a). FG: frontal gyrus, PrG: precentral gyrus, PoG: postcentral gyrus, IPC: inferior parietal cortex, CW: cerebral white matter, Ca: caudate nucleus, IC: internal capsule, Put: putamen, Th: thalamus. The colormap represents the normalized PA amplitude.

4.3.2 Temporal Traces of Electrically Evoked Hemodynamic Changes of Different Regions in Cortical and Subcortical Brain Structures

The analysis proceeded with an examination of the temporal traces of PA signals across various regions. Initially, each pixel's temporal trace in the images was adjusted by subtracting the baseline, determined via linear regression of the pre-stimulation phase, and then normalized against the baseline's original signal strength (the root mean square of the pre-stimulation temporal trace), creating baseline-adjusted and normalized PA signals (ΔPA/PA). To assess the variations in hemodynamic responses across different cortical and subcortical regions, and to incorporate all vessels, regardless of their orientation relative to the limited perspective of the reconstructed images, we averaged the temporal traces for different regions. These included cortical areas such as gyrus regions (FG, PrG, PoG, IPC) and cerebral white matter, along with subcortical areas like the caudate nucleus (Ca), internal capsule (IC), putamen (Put), and thalamus (Th).

Following an 8 mA electrical stimulation applied to the left index finger, significant hemodynamic changes were observed in the cortical areas at the level of the somatosensory cortex, aligning with existing literature [130–132]. Notably, the stimulation, despite not inducing limb movements in the monkey, could have triggered muscle contractions in the limb, thereby activating mild hemodynamic alterations in the cortical regions beneath the motor cortex and premotor cortices, which were approximately 20% and 12% less intense, respectively, as shown in Figure 4.4a and c. The subcortical responses, affected by optical and acoustic attenuation through cortical tissues, were notably weaker (44-64% lower) in the areas beneath the somatosensory cortex, motor cortex, and premotor cortices compared to cortical areas, as illustrated in Figure 4.4a, c, and e. Additionally, the level of stimulation influenced the response magnitude, with all three cortical areas exhibiting 19%-37% weaker responses to 3 mA stimulation compared to 8 mA stimulation, as depicted in Figure 4.4b,d, and f.

An intriguing observation of our hemodynamic responses is a dip in some of the temporal traces shortly after the 30 sec. The initial-dip is frequently observed in functional neuroimaging signals, immediately after stimulus onset, [139] which reflects an autoregulatory adjustment in the local blood flow, a response to the initial increase in neuronal activity and associated metabolic demand. While the exact mechanism behind this observation remains to be fully elucidated and can be further explored with multi-wavelength imaging settings, it demonstrated the sensitivity of our PACT system in detecting subtle fluctuations in hemodynamic activity.

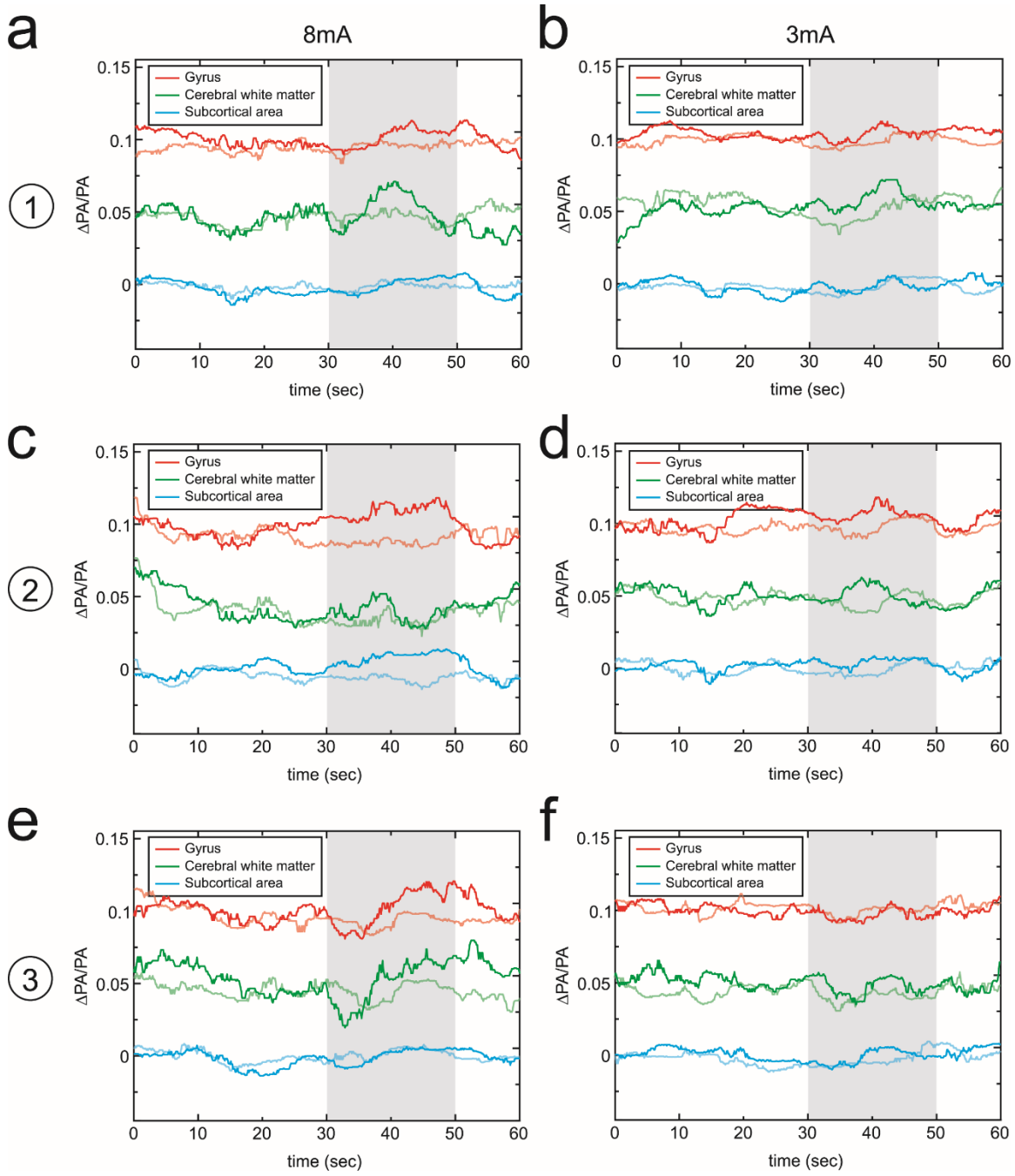

Figure 4.4: PACT of electrically evoked hemodynamic change *in vivo*. The temporal traces of the baseline-subtracted and normalized PA signals (ΔPA/PA) for cortical, including gyrus (FG, PrG, PoG, IPC) and cerebral white matter (CW), and subcortical (Ca, IC, Put, Th) brain regions at PMd and PMv of the right hemisphere with electrical stimulation of (a) 8 mA and (b) 3 mA on the left hand index finger. (c-d) The temporal traces of different brain regions at M1 with electrical stimulation of 8 mA and 3 mA, respectively. (e-f) The temporal traces of different brain regions at S1 with electrical stimulation of 8 mA and 3 mA. The light red, green, and blue lines indicate the temporal traces with electrical stimulation on the right hand index finger (control). Shaded area represents the time period of the stimulation.

4.3.3 Temporal Traces of Electrically Evoked Hemodynamic Change of Single Vessels in the Cortical Brain

In each imaged slice, two major blood vessels within the white matter were pinpointed due to their pronounced PA signal amplitudes, as shown in Figure 4.5 (labeled as vessels 1 through 6 in Figure 4.3b-d). A closer examination revealed that certain vessels, such as vessel 1 and vessel 4, exhibited more robust responses under 8 mA electrical stimulation compared to the overall regional analysis presented in Figure 4.4. The response levels of most vessels were relatively consistent, yet notably, vessel 3 demonstrated an almost negligible response under 8 mA stimulation when contrasted with the regional analysis of the gyrus areas in slice 2. This observation suggests that analyzing individual vessels could be crucial for identifying those that contribute significantly to the hemodynamic responses in white matter. It became evident that higher hemodynamic responses might be achieved through this method. However, not every primary vessel (those with strong PA signals) played a role in the observed responses within the white matter.

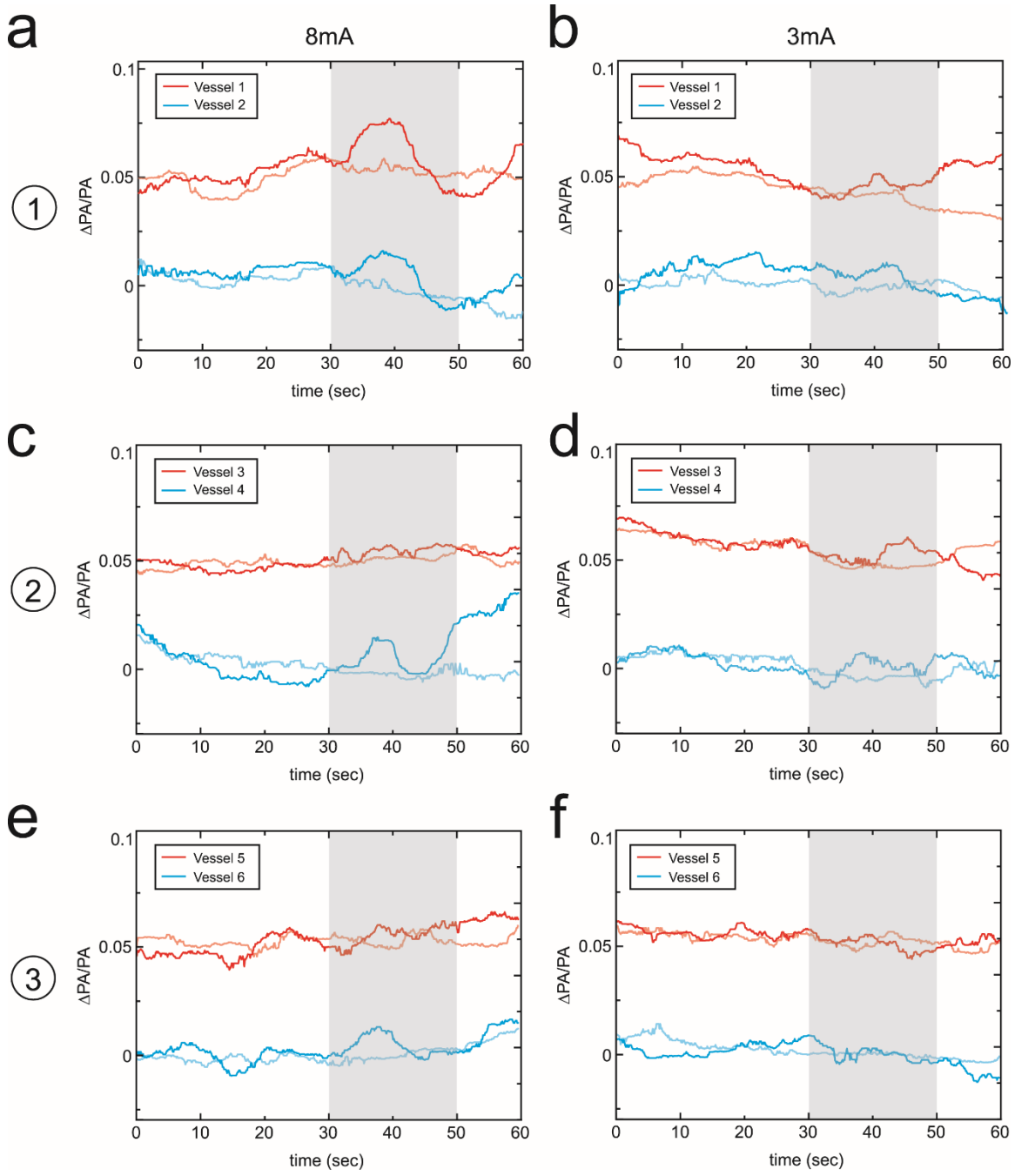

Figure 4.5: Temporal traces electrically evoked hemodynamic changes in single blood vessels *in vivo*. The temporal traces of the baseline-subtracted and normalized PA signals (ΔPA/PA) for the two vessels with the highest signal strength at the level of PMd and PMv of the right hemisphere with electrical stimulation of (a) 8 mA and (b) 3 mA on the left hand index finger. (c-d) The temporal traces of the two strongest vessels at the level of M1 with electrical stimulation of 8 mA and 3 mA, respectively. (e-f) The temporal traces of the two strongest vessels at the level of S1 with electrical stimulation of 8 mA and 3 mA, respectively. The vessel positions are shown in Fig. 2. The light red, green and blue lines indicate the temporal traces with electrical stimulation on the right hand index finger (control). Shaded area represents the time period of the stimulation.

4.3.4 Functional Imaging by Hemodynamic Change during Electrical Stimulation

Functional images were derived by assessing the variations in signal amplitude across each pixel within the temporal PA images. This assessment was carried out by comparing the signal amplitude during the stimulation phase (spanning 30-50 seconds) against the amplitude in the pre-stimulation phase (0-30 seconds). Regions where the relative amplitude change surpassed 0.5% (the average relative change observed in control groups) were highlighted in hues ranging from yellow to red over the grayscale PA images. This coloration indicated regions experiencing hemodynamic responses to the electrical stimulation, as depicted in Figure 4.6. Predominantly, areas manifesting significant hemodynamic alterations were found within the white matter. Comparatively fewer changes were noted in the gyrus regions, with the weakest functional changes detected in the subcortical areas. These functional images effectively illustrated the specific vessel pixels that were reactive to the peripheral electrical stimulation.

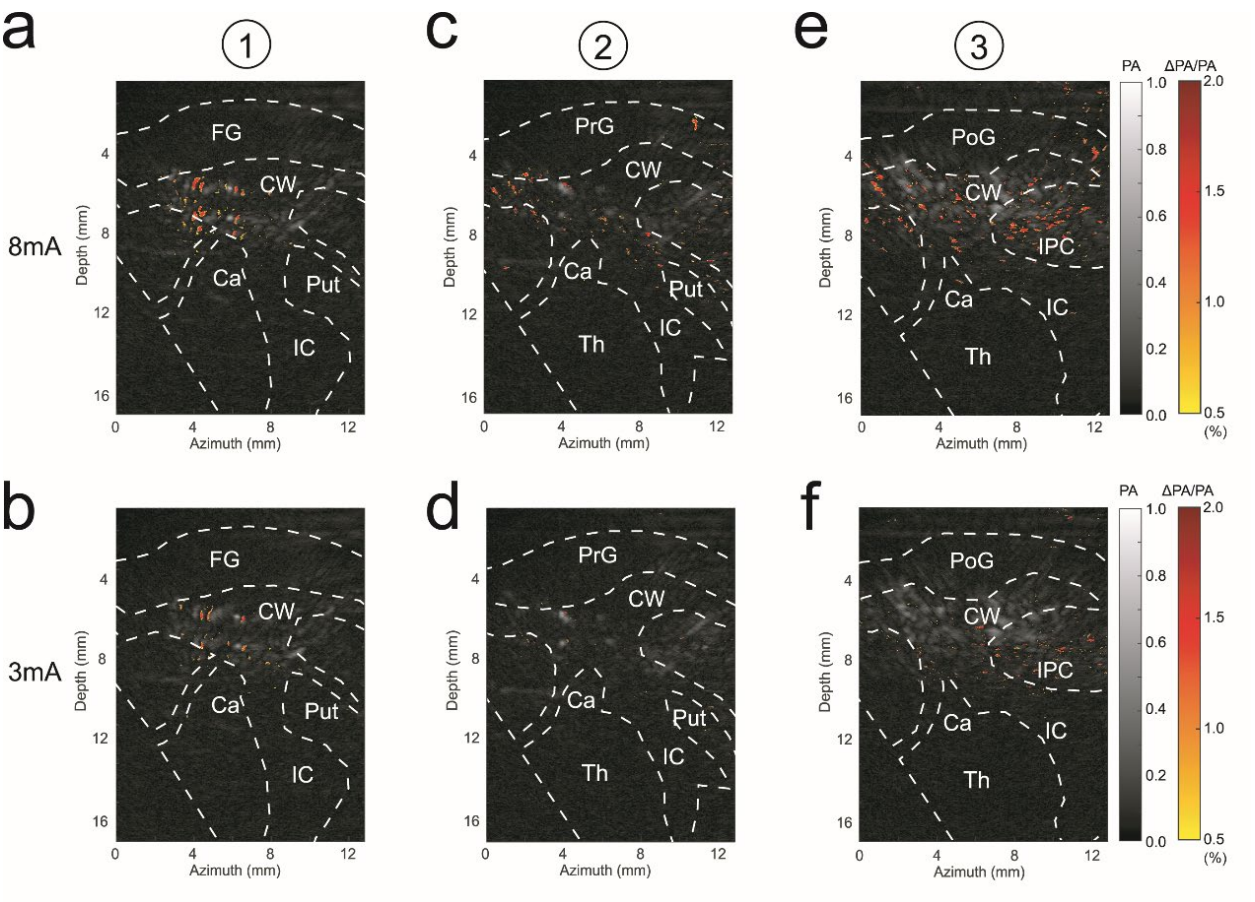

Figure 4.6: Functional imaging by electrically evoked hemodynamic change before and during the stimulation. The regions at the level of PMd and PMv of the right hemisphere under electrical stimulation (grayscale) of (a) 8 mA and (b) 3 mA with the relative variation of the average signals during the stimulation to the average signals before the stimulation. (c-d) The regions with the relative variation at the level of M1 with electrical stimulation of 8 mA and 3 mA, respectively. (e-f) The regions with the normalized variation at the level of S1 with electrical stimulation of 8 mA and 3 mA, respectively. The colormaps represent the normalized PA amplitude and relative amplitude variation, respectively.

4.3.5 PAM in the Primary Somatosensory Cortex

The highly sensitive PAM system, as depicted in Figure 4.1b, was employed to closely analyze the S1 area (illustrated in Figure 4.7a) to showcase the multi-level capabilities of PAI technology. The vascular structure seen in the PAM image (Figure 4.7b) was in good agreement with the photograph in Figure 4.7a, except for a minor discrepancy in the lower left corner caused by a loss of laser focus attributable to the brain's contoured surface. Following this, the relative PA

signal representing hemodynamic changes was determined. This process involved deducting the pre-stimulation PA signal and then carrying out a normalization procedure. With the application of 8 mA electrical stimulation, a pronounced relative signal change was observed at the primary vessels' origin, gradually diminishing along the microvessels, as shown in Figure 4.7c. Consistent with PACT findings, the relative change was markedly reduced (74% lower) with a 3 mA stimulation compared to an 8 mA stimulation. These observations affirm that electrically evoked hemodynamic alterations during stimulation can be effectively captured using both PACT and PAM setups. While PACT offers insights into deeper brain regions (approximately 16 mm) with a high temporal resolution of 10 Hz, PAM excels in rendering high-resolution vascular images and exhibits heightened sensitivity to hemodynamic responses.

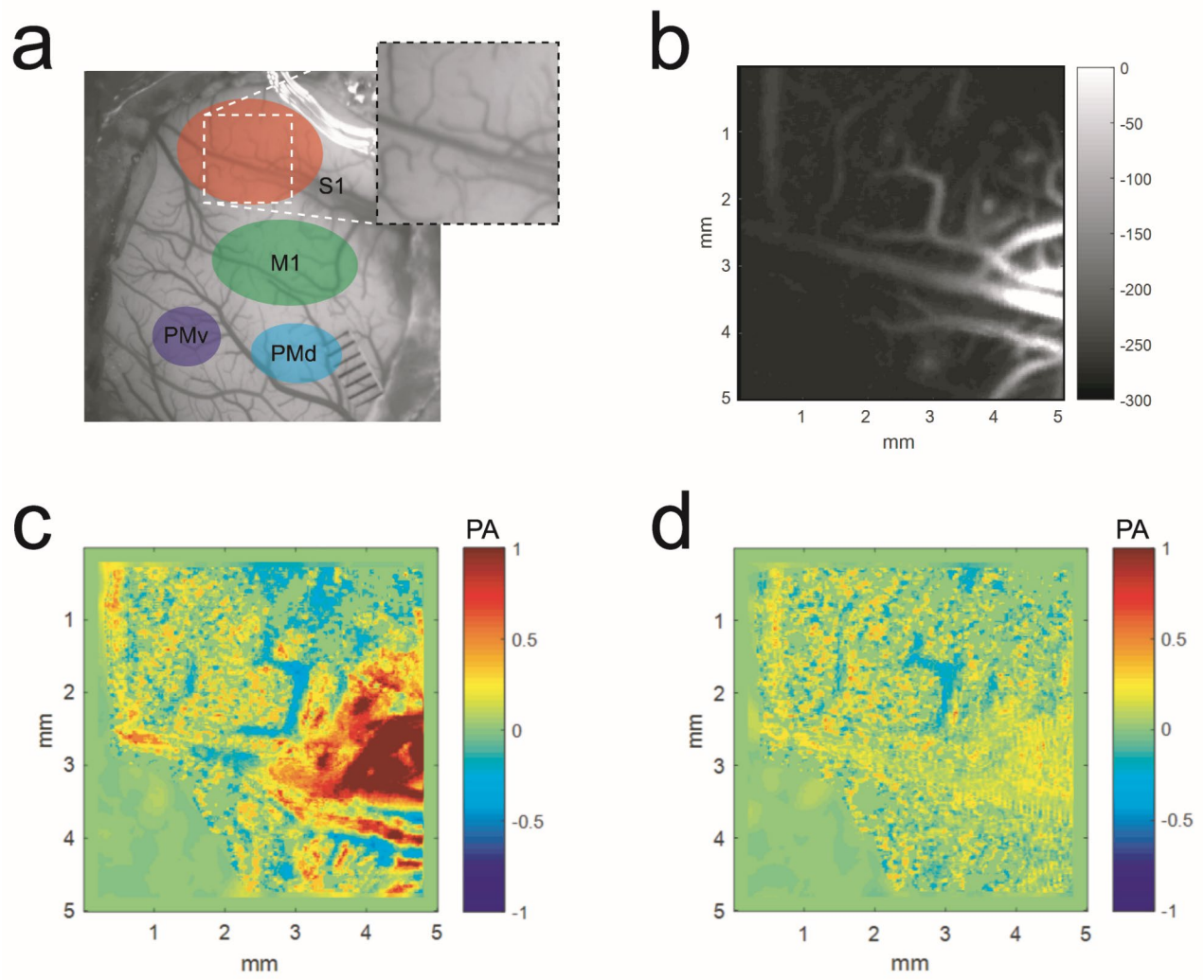

Figure 4.7: PAM of electrically evoked hemodynamic change. (a) Cerebral cortex regions shown on the photograph of the squirrel monkey brain. (b) The PAM image at S1. The relative change of hemodynamic signals at S1 after electrical stimulation of (c) 8 mA and (d) 3 mA. The colormap represents the normalized relative PA signal change.

4.3.6 PAM Image of NHP Cerebral Cortex with and without FCNN

In some cases where PAM suffers from degraded imaging quality due to imperfect animal handling for optimized imaging plane or motion artifacts, FCNN was implemented to improve the image quality of PAM images. Figure 4.8 displays the distinct contrast in PAM images before and after the application of FCNN. Initially, the PAM images without FCNN enhancement displayed a central area with acceptable SNR. However, post-FCNN application, the SNR in PAM images

exhibited a significant boost of 183.94%, underscoring a notable enhancement in image clarity (as indicated in Figure 4.8e). This improvement was statistically significant ($n=9$, $p<0.0001$). Moreover, the vessel count in the images also showed a substantial increase, rising from an average of 10 to 22.25 ($n = 8$, $p = 0.0002$), as depicted in Figure 4.8d. Similarly, the vessel area in FCNN-enhanced images experienced a 175% increase compared to the original PAM images ($n = 8$, $p < 0.0001$), further proving the improvement in image quality. Table 4-1 shows the numerical ranges of SNR of each image.

Additionally, the correlation coefficient of PA signals in FCNN-processed images surged by 25.96% ($n = 8$, $p < 0.0001$), as seen in Figure 4.8e, significantly higher than the original PAM images. This metric directly assesses the linear correlation between two images [133], with a full correlation represented by 1, a perfect negative correlation by -1, and no correlation by 0 [134]. The heightened correlation in FCNN-processed images suggests that the original PA signals were effectively retained during the enhancement process.

Similarly, SSIM for signals from FCNN-processed images was 31.66% higher than those from the original PAM images (Table 4-2). This index evaluates the similarity in terms of luminance, contrast, and structural elements between two images. A higher SSIM implies a closer resemblance in contrast, luminance, and structure. The enhanced SSIM in FCNN images, especially within the same group as shown in Figure 4.8e, indicates that these images were more aligned in terms of luminance, contrast, and structure compared to the original PAM images. This enhancement in SSIM further reinforces the effectiveness of FCNN in preserving and enhancing the quality of the original images [134–136].

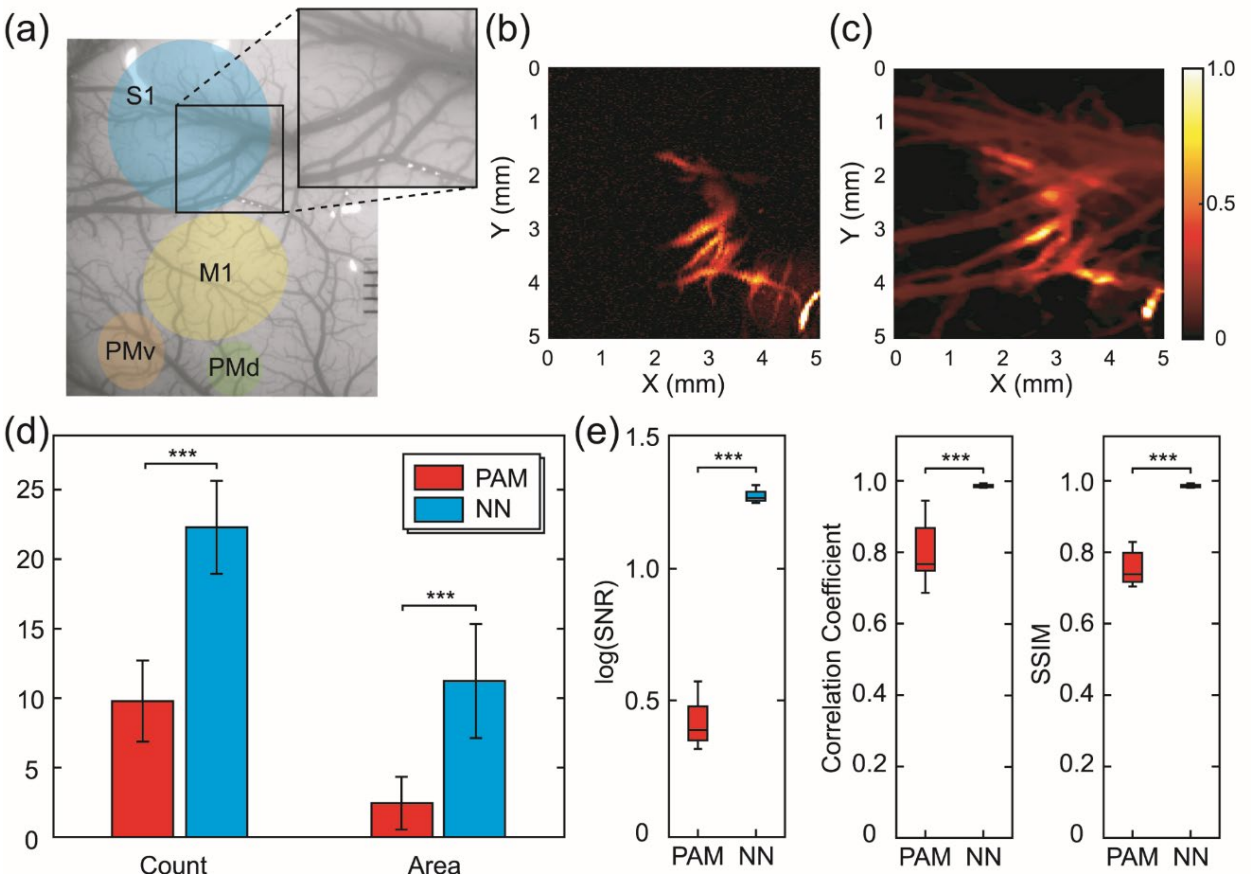

Figure 4.8: (a) Photograph, (b) originally acquired PAM image, and (c) FCNN processed PAM image of the vasculatures covering part of the primary somatosensory cortex. (d) Statistics of the vessel count (n = 9) and the vessel area (n = 9) of the original PAM and the FCNN processed image(e) The comparison of image quality including SNR (n = 9), correlation coefficient (n = 8), and SSIM (n = 8) between the same groups in PAM and FCNN-processed (NN) images. *** indicates statistical significance of $p < 0.001$ for the paired t-test.

Table 4-1: Signal-to-noise ratio of raw PAM and FCNN images

Image No.	PAM	FCNN
1	0.571791	1.265016
2	0.528976	1.267251
3	0.475756	1.313893
4	0.439158	1.264556
5	0.403036	1.261447
6	0.420194	1.294836
7	0.383402	1.273702
8	0.384489	1.30257
9	0.433842	1.229658

Table 4-2: Structural similarity index of raw PAM and FCNN images

	Image 1	Image 2	PAM	FCNN
D5	Sample 1 (0 seconds)	Sample 2 (0 seconds)	0.821667	0.997362
	Sample 1 (10 seconds)	Sample 2 (10 seconds)	0.710776	0.992581
	Control	Sample 1 (0 seconds)	0.820581	0.995404
	Control	Sample 2 (0 seconds)	0.780195	0.992376
D1	Sample 1 (0 seconds)	Sample 2 (0 seconds)	0.711379	0.987779
	Sample 1 (10 seconds)	Sample 2 (10 seconds)	0.740649	0.994644
	Control	Sample 1 (0 seconds)	0.724863	0.99152
	Control	Sample 2 (0 seconds)	0.720991	0.988837

4.3.7 PAM of Functional Changes due to the Peripheral Mechanical Stimulation

Hemodynamic changes on the NHP cortex were first detected by PAM, and then the functional changes were analyzed based on the original PAM images (Figure 4.9a) and those enhanced using FCNN model (Figure 4.9b) by calculating the fractional change from the control groups (ΔPA/PA). Notably, in the primary somatosensory cortex, clear functional changes were observed in PAM images captured within two time periods: from 0 to 10 seconds and from 10 to 20 seconds following the onset of mechanical stimulation on digits D1 and D5. These hemodynamic shifts, indicated by either an increase (FM+, positive change) or decrease (FM-, negative change) in cortical blood volume in response to finger tapping, are shown in Figure 4.9. The observed decrease in blood volume might be attributed to vessel constriction, counterbalancing increased blood volume in nearby vessels to maintain stable blood pressure.

The minor changes are not displayed because they are mostly from the noise. The apparent discontinuity in the changes observed within a single vessel is likely due to the temporal resolution of 10s. The functional changes based on the original PAM images showed more artifacts than the processed ones, while the overall changes were similar, because the FCNN model only improved the image quality, and would not induce or reduce the functional characteristics. The PA signals

acquired at 10s after stimulation were stronger when compared to control. The functional changes detected between 10 to 20s are slightly stronger than those between 0 to 10s, possibly due to the delayed onset of hemodynamic changes. There is no apparent difference between the stimulation on different fingers.

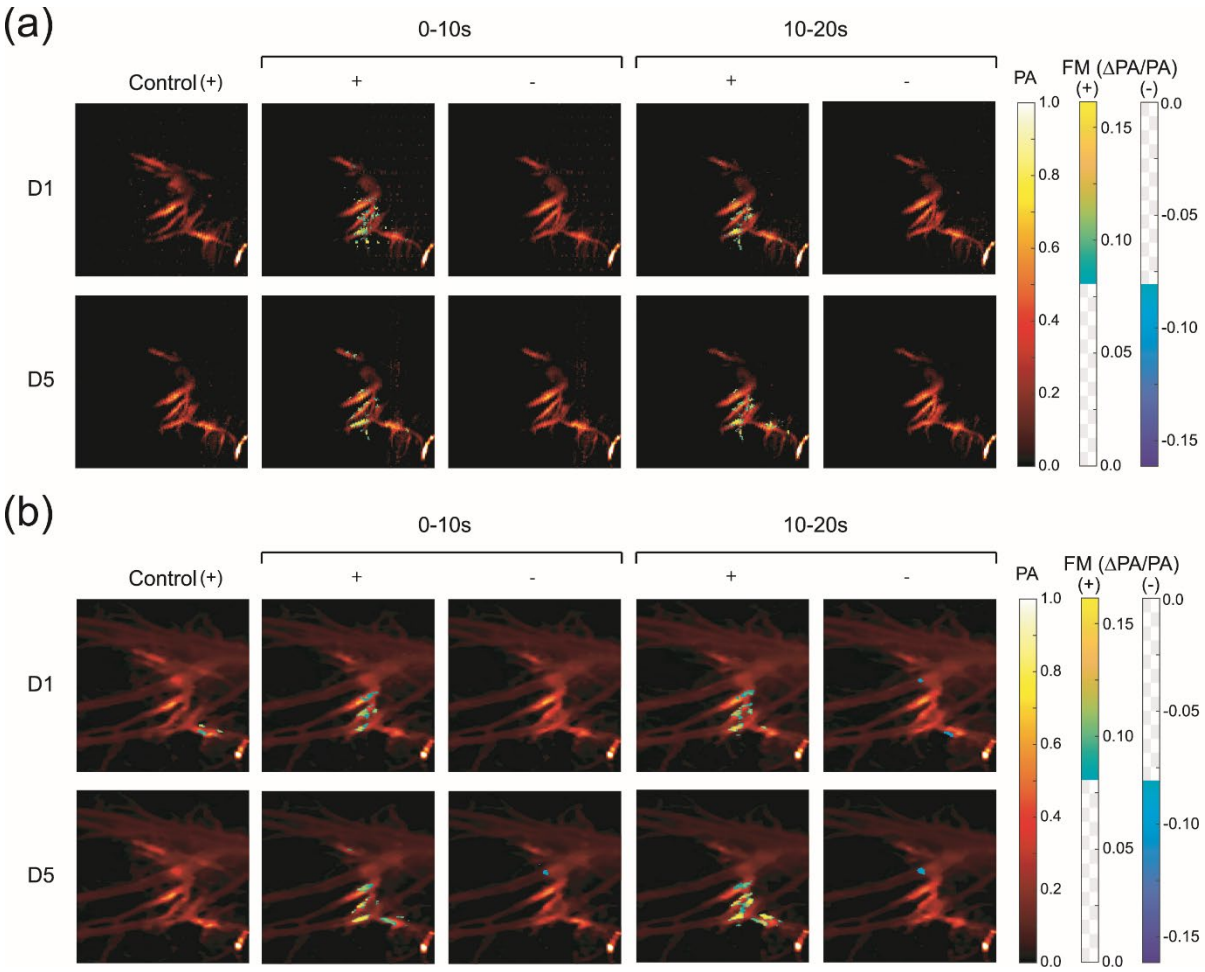

Figure 4.9: Functional maps (FM) overlying the vasculature on (a) the original PAM images and (b) FCNN images of the control, and at 0s and 10s after mechanical stimulation on D1 and D5 fingers. Positive and negative changes are shown separately.

4.4 Discussion and Conclusions

Prior to our investigation, the field of neuroimaging in NHPs was primarily characterized using conventional methodologies such as fMRI [58,59] and fUS [60], each with its inherent limitations. While fMRI offers whole-brain imaging, it struggles with high costs, limited temporal resolution, and motion artifacts, especially in awake and active NHP subjects. fUS, on the other hand, although promising in imaging cerebral blood volume, lacks the sensitivity to finer capillary flow and cannot assess blood oxygenation.

In this context, our study represents a significant leap forward in NHP neuroimaging. By developing and applying PACT and PAM systems for NHP brain imaging, we have bridged a crucial gap in imaging capabilities and enhanced the depth and fidelity of neurobiological insights. We developed a linear-array PACT system tailored for imaging subcortical regions and a high-resolution PAM system for capturing detailed images of cortical areas in the brain of a squirrel monkey. This approach allowed us to monitor the hemodynamic responses of multiple cortical and subcortical areas, particularly in response to peripheral electrical stimulation. We observed consistent responses in both cortical and subcortical regions, with varying intensities based on the electrical stimulation's strength. This variability in response strength underlines the sensitivity of these imaging techniques in detecting subtle hemodynamic changes.

Our findings demonstrate the potential of PACT and PAM in mapping complex neural responses and their multiscale and multi-resolution imaging capabilities. We noted that the temporal resolution of the PAM system, around 10 seconds, could be better optimized. Future developments could include the use of lasers with higher repetition rates for PA excitation and adjusting US transducer frequencies to improve depth penetration and reduce skull aberrations.

In the case of our PAM studies on NHPs, we focused on monitoring hemodynamic responses induced by mechanical stimulation. Although the PAM system's shallow tissue penetration limits its application for transcranial imaging in NHPs, its sensitivity and resolution are adequate for observing cortical responses. The study also addressed potential motion artifacts due to heartbeat and respiration in NHPs. The use of control groups without stimulation validated the minimization of these artifacts in our imaging results.

The study faced challenges in imaging quality due to the larger, more complex nature of NHP brains compared to mice. These challenges included difficulties in optimal positioning of the imaging plane and increased motion artifacts. However, we addressed these issues effectively through the application of FCNN, which significantly enhanced the image quality without compromising the hemodynamic sensitivity. FCNN notably improved the signal-to-noise ratio (SNR), correlation coefficient (CC), and structural similarity index (SSIM), indicating its effectiveness in recovering lost vascular structural information while preserving the integrity of functional changes.

Our exploration of the use of a single wavelength laser focused on a specific 5mm x 5mm area of the somatosensory cortex, demonstrating that this approach is sufficient to monitor desired functional changes in response to stimulation. This foundational work lays the groundwork for future studies that might incorporate multi-wavelength laser systems for more thorough hemodynamic assessments, further advancing our understanding of brain function and adaptation in NHP models.

Overall, our study underscores the value of advanced PAI technologies in neuroscience research. As these techniques continue to evolve, they promise to offer even more profound

insights into the workings of the primate brain, enhancing our capacity to address complex neurological conditions and contribute to the development of novel therapeutic approaches.

4.5 Acknowledgements

In reflecting upon the successes and advancements achieved in this study, it is crucial to acknowledge and appreciate the vital contributions of our collaborative partners. The proficiency and dedication of the surgical team from the University of Kansas Medical Center, Prof. Randolph J. Nudo's research group, were indispensable in the preparation and cortical mapping of the non-human primates. Their expertise ensured the precise execution of the intricate surgical and stimulation procedures, laying a solid foundation for our subsequent imaging and analysis. Additionally, the innovative analytical work conducted by Madhumithra Subramanian Karthikesh from Dr. Xinmai Yang's research group at the University of Kansas was pivotal in the application and optimization of the FCNN. This collaboration enhanced the quality of our PAM images and exemplified the seamless integration of computational neuroscience into advanced imaging techniques. The collaboration between these groups, combining clinical precision, neuroscientific expertise, and computational innovation, played a significant role in the completion of this research. This interdisciplinary partnership enriched the depth and breadth of our study and set a precedent for future collaborative endeavors in the realm of neuroimaging and neuroscience research.

Chapter 5 Comparative Analysis of Mouse Models with CMUT and Piezoelectric Arrays

5.1 Introduction

In the rapidly evolving field of neuroscientific imaging, the exploration of advanced ultrasonic transducer technologies holds a critical place. In this chapter, a comparative analysis of capacitive micromachined ultrasonic transducer (CMUT) arrays and piezoelectric transducer arrays was conducted in the context of photoacoustic computed tomography (PACT) in mouse models. This comparison is fundamental in understanding the relative advantages and potential limitations of each technology and in displaying their practical applicability in neuroscientific research.

This study is significantly enriched by the collaboration with North Carolina State University, particularly the expertise brought forth by Prof. Ömer Oralkan's research group. Their groundbreaking work in the fabrication of the CMUT array was a cornerstone of this project, providing a sophisticated and high-performing tool for our imaging needs. The precision and innovation inherent in their fabrication process were crucial in enhancing the capabilities of the CMUT array, demonstrating a notable advancement in ultrasonic transducer technology. Additionally, the hands-on assistance of Ermek Belekov, a talented member of Prof. Oralkan's team, was instrumental during the experimental phase. Ermek's technical expertise and understanding of CMUT technology ensured the meticulous execution of the imaging experiments, thereby facilitating the collection of high-quality data.

In this chapter, we intend to provide a detailed examination of the spatial resolution, signal-to-noise ratio, and overall imaging performance of both CMUT and piezoelectric arrays in a controlled experimental setup. This analysis is expected to offer valuable insights into the suitability of these technologies for neuroscientific applications, potentially guiding future research directions in the field of ultrasonic imaging.

5.2 Material and Methods

5.2.1 Imaging Phantom

To evaluate the spatial resolution of the transducer arrays at different depths, we utilized fishing lines with a diameter of 200 micrometers. These lines were placed in water at an angle intersecting the imaging plane. By employing a mechanical translation stage, we precisely adjusted the proximity of the fishing line to the surface of the array. The determination of imaging resolution involved deconvolution of the fishing line profiles captured in both PACT and ultrasound (US) images. This process was based on comparing these profiles to the actual cross-sectional shape of the fishing lines, i.e., a circle with a 200 μm diameter.

5.2.2 Animal Procedures

The research adhered to the guidelines approved by the University of Michigan's Institutional Animal Care and Use Committee. The study utilized male C57BL/6 wild-type mice, aged between 4 to 7 months, acquired from Jackson Laboratory (JAX000664). Three mice were used to test each array, and they were maintained on a 12-hour light/dark cycle, PACT conducted during their light phase. Other details have been previously described in 3.2.3 and 3.2.4.

5.2.3 Transducer Arrays and US Platform

This research involved a comparative analysis between a piezoelectric transducer array and a CMUT array, each comprising 256 elements. The piezoelectric array, a commercially available L8-18i model from GE Healthcare, operated at a central frequency of 13 MHz and offered a bandwidth ranging from 8 to 18 MHz. Its dimensions were 11.1 mm by 34.8 mm. The custom-built CMUT array featured a central frequency of 14 MHz, with an extensive bandwidth spanning 3 to 25 MHz, and measured 3.0 mm by 24.9 mm in size, as depicted in Figure 5.1A [90,91,137]. This array's elements were designed with lateral and elevational dimensions of 99 μm and 2988 μm, respectively, and an element pitch of 97 μm. Figure 5.1B illustrates a 3D printed holder that combines these transducer arrays with illumination optical fibers for PACT. Figure 5.1C presents the schematic design of the combined PACT-US imaging system.

For PACT, an Nd:YAG laser-pumped optical parametric oscillator (OPO) (Phocus Mobile, Opotek Inc.) served as the excitation source. The OPO's output featured a pulse duration of 4–6 ns, a 10 Hz repetition rate, and pulse energy variability under 5%. During phantom studies, a 5-mm-diameter fiber bundle from the OPO laser provided optimal illumination of the fishing line, positioned 30 mm from the emission source. The fishing line, set at distances of 10, 15, or 20 mm from the probe, was imaged with both US and PACT at each location without signal averaging.

In the animal experiments, the transducer array was initially aligned with the mouse brain's coronal plane, scanning across the entire brain. A particular plane, capturing both the primary visual cortex (V1) and the superior colliculus (SC), was selected by correlating the US images with the Allen Brain Atlas. During the procedure, PACT and US images were continuously recorded.

For PACT operations, a custom multimode fiber bundle, with fibers attached to either side of the linear arrays, conveyed laser energy. This bundle comprised 32 fibers spanning 25 mm on each side, ensuring overlapping projections at the skull surface, situated 15 mm from the array. The experiments employed a 797 nm wavelength, a range to which mouse retinal photoreceptors are non-responsive, thereby preventing interference with visual stimulation. At this wavelength, both oxygenated and deoxygenated hemoglobin exhibit identical absorption coefficients. The optical fluence at the skull did not exceed ~20 mJ/cm^2, adhering to the American National Standards Institute's safety guidelines. The PA signals were digitalized and sampled at 40 MHz using a Vantage 256 ultrasound system from Verasonics, with both arrays configured identically. The system's frame rate, dictated by the laser's repetition rate, was 10 Hz.

Following each PA data capture, a corresponding US frame was recorded using plane wave transmission for both arrays. Data acquisition covered 20 seconds before, 10 seconds during, and 30 seconds post retinal photostimulation, totaling 600 frames per session. To maintain dark-adapted conditions, each mouse underwent a single photostimulation session.

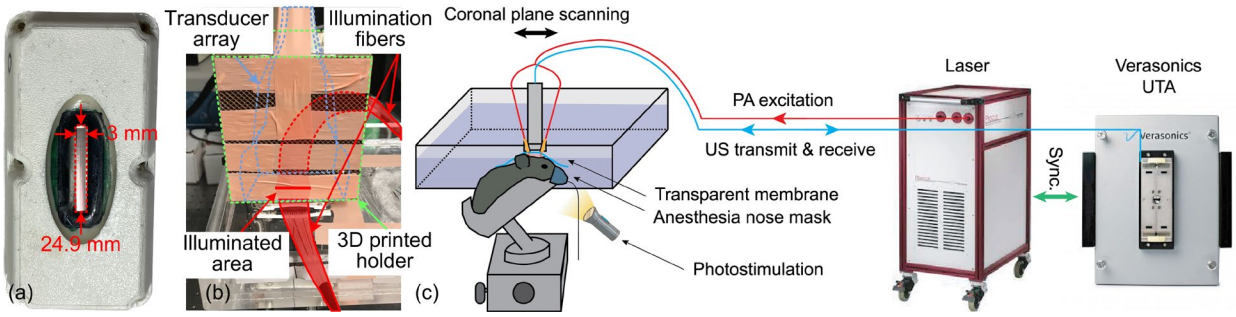

Figure 5.1: PACT-US imaging system. (a) Dimensions of the CMUT array. (b) PACT setup. A 3D-printed holder integrated the transducer arrays and the illumination fibers. The illumination was projected into a narrow band at the mouse skull surface. (c) The system schematics. Red lines show the optical paths. Blue lines show the acoustic signal paths.

5.2.4 Image Reconstruction and Signal Processing

The reconstruction of both US and PACT frames in this study was carried out using delay-and-sum (DAS) beamforming algorithms. The following steps detail the method for isolating responses in the visual regions:

(1) A temporal trace was extracted from each pixel across consecutive frames in the PACT images.

(2) Each temporal trace was detrended by subtracting its linear fitting line, calculated during the pre-stimulation phase, to eliminate any systematic shifts in the detected signals.

(3) Each detrended temporal trace was then normalized using the root-mean-square of the signal strength from the original pre-stimulation temporal trace. This process yielded baseline-subtracted and normalized photoacoustic (PA) signals (ΔPA/PA).

(4) To reduce noise arising from random fluctuations, a spatial moving average of 3×3 pixels and a temporal forward-moving average covering 25 frames (equivalent to 2.5 seconds) were applied. The selection of these averaging dimensions was informed by a prior leading study in the field of optoacoustic brain imaging in mice.

(5) The V1 and SC regions in the PACT images were located by cross-referencing the US images with the Allen brain atlas. The average temporal trace for each region was computed by aggregating the pixel-wise temporal traces within that region.

For the purpose of this research, signal-to-noise ratio (SNR) of the normalized, visual-evoked PA signals was defined as the peak magnitude of these signals divided by their standard deviation during the 20-second period preceding retinal photostimulation. The study encompassed a total of six mice, with three each being evaluated using the piezoelectric transducer and the

CMUT arrays. Student's t-tests were conducted with the null hypothesis that there was no significant difference in the SNR produced by the two types of transducer arrays.

5.3 Results

5.3.1 Phantom Studies with Fishing Line Targets

The US and PACT images, featuring the fishing lines, underwent a process of deconvolution using the actual profiles of these lines. This technique helped in generating the point spread function, which is illustrated in Figure 5.2 of the study. Both the piezoelectric transducer and the CMUT array were capable of precisely identifying the locations of the fishing lines. However, the CMUT array demonstrated superior spatial resolution, ranging from 1.3 to 2.9 times better compared to the piezoelectric transducer, as evidenced in Figure 5.3. This enhanced resolution of the CMUT array can be attributed to its broader frequency bandwidth. Additionally, the CMUT array exhibited a higher SNR. This improvement in SNR is likely due to the integration of front-end electronics directly into the imaging probe, enhancing the overall imaging performance.

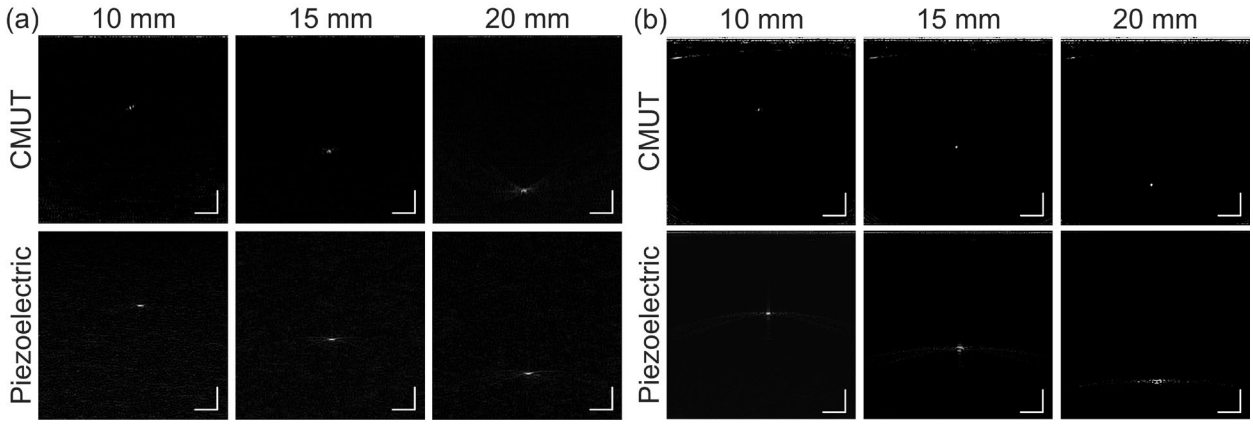

Figure 5.2: Point spread functions produced by imaging a fishing line at 10 mm, 15 mm, and 20 mm depths, respectively. (a) PA images. (b) US images. Scale bars are 3 mm.

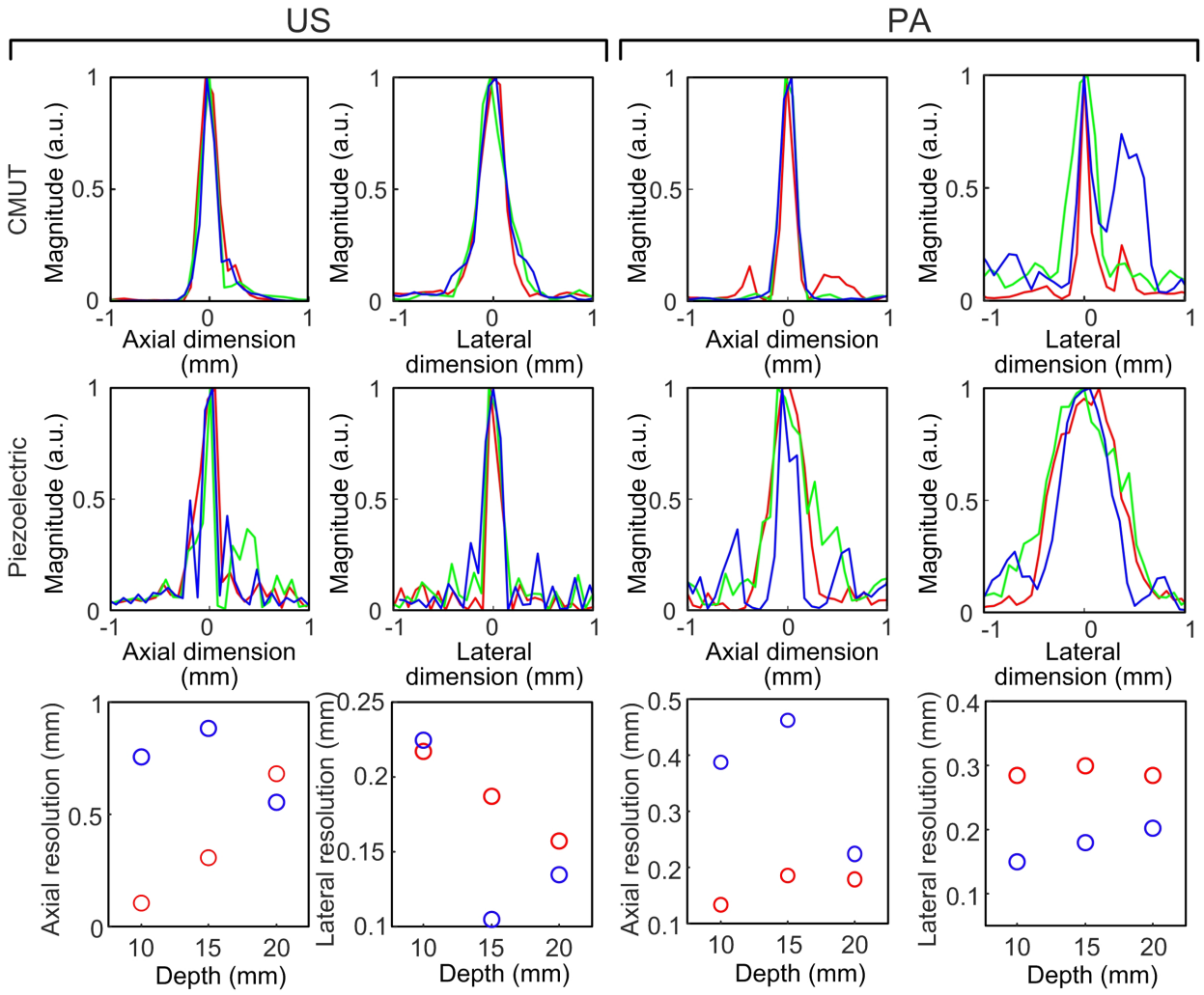

Figure 5.3: Point spread function profiles in Figure 5.2. The distance between the fishing lines and the transducer array surfaces is coded in color. In Rows 1 and 2, red, green, and blue curves represent point spread functions at 10 mm, 15 mm, and 20 mm depths, respectively. In Row 3, red and blue circles represent CMUT and piezoelectric arrays, respectively.

5.3.2 Photoacoustic Imaging of the Mouse Brain In Vivo

Figure 5.4 presents the US and PACT images obtained using both transducer arrays. The US images from both systems effectively revealed the internal structures of the brain, aiding in identifying specific regions of interest. The images captured by the CMUT array displayed a

marginally more diverse range of anatomical features within the brain's interior compared to piezoelectric array.

In the PACT images generated by both arrays, there was a depiction of anatomical details within the brain, albeit with less clarity than observed in the US images. This reduced clarity in the PACT images can be attributed to the inherent nature of PA emissions [138], which are omnidirectional. This characteristic often leads to the creation of more artifacts during the reconstruction process.

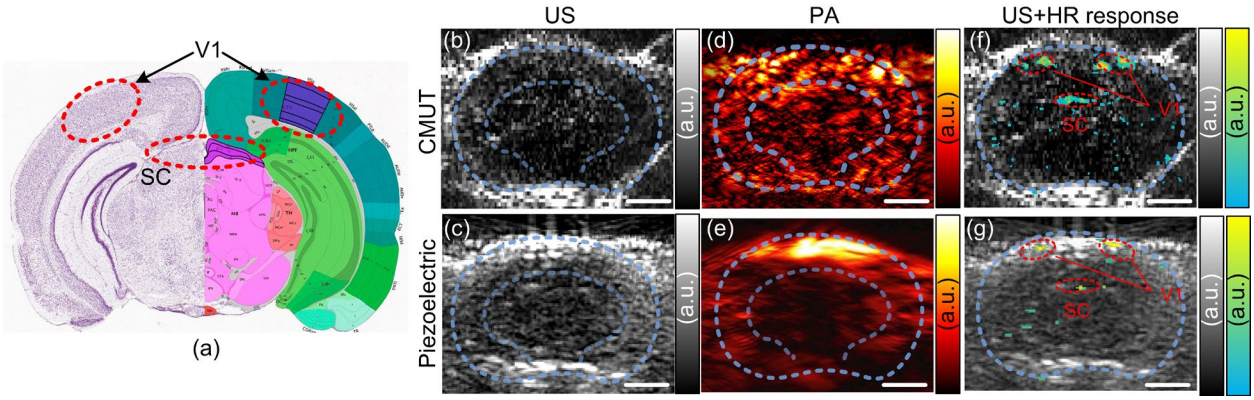

Figure 5.4: Images acquired by the CMUT and piezoelectric arrays. (a) Allen brain atlas showing the plane with V1 and SC regions. (b-c) US images. (d-e) PAT images. (f-g) hemodynamic responses on top of the US images. Scale bars: 3 mm. V1: primary visual cortex. SC: subcortical superior colliculus.

5.3.3 Visual-Evoked Hemodynamic Response

Figure 5.4f and g illustrate the visual areas identified in the US images, along with the peak values of hemodynamic reactions observed within the 60-second monitoring period. Figure 5.5a and b depict the temporal traces within the regions of the V1 and SC. Figure 5.5c presents the statistical analysis of the SNR for V1 and SC observations using both transducer arrays. In the V1 region, the CMUT array produced an SNR that was 5 dB higher than that of the piezoelectric

transducer array, with three mice tested in each group and a p-value of 0.04. In terms of SNR measurements in the SC region, both transducer arrays demonstrated similar performance.

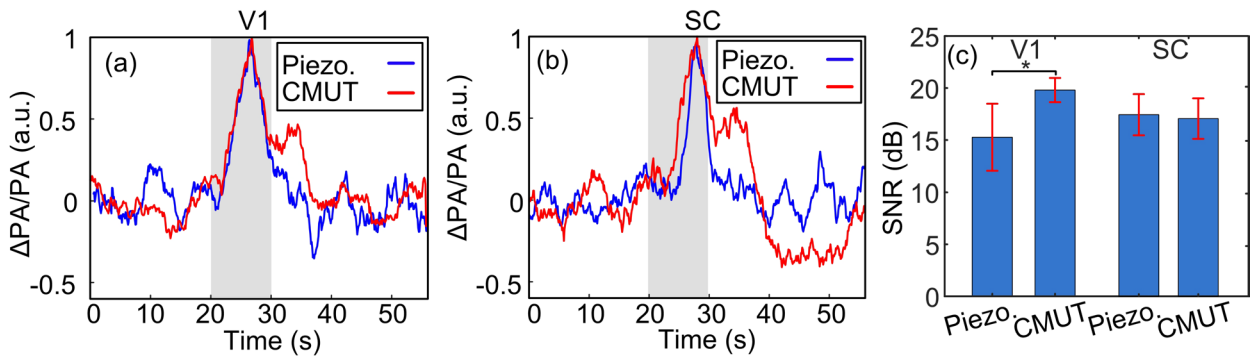

Figure 5.5: Hemodynamic responses in visual regions. (a-b) Hemodynamic responses in V1 and SC regions, respectively. (c) Statistics of the SNR of the hemodynamic responses. * indicates a significant difference in the t-test. N=3 for each group. Piezo.: Piezoelectric transducer.

5.4 Discussion

This research acknowledges certain constraints, notably that the piezoelectric transducer array and the CMUT array were not precisely matched in specifications. With this caveat, the comparative analysis suggests that CMUT holds up well against or possibly surpasses the piezoelectric array in aspects like spatial resolution, penetration depth, and SNR in the tested conditions. The piezoelectric array exhibited marginally superior lateral resolution, likely attributable to its broader aperture. Given CMUT's attributes of being lightweight, flexible, and scalable to 2D array configurations, it emerges as a promising option for examining brain activity in small animals that are awake and unrestricted – a scenario where using piezoelectric transducer arrays could be challenging.

In Figure 5.3, the piezoelectric array displayed a less consistent relationship between resolution and depth compared to the CMUT array. This inconsistency could stem from the

piezoelectric array's lower SNR, aligning with the observed variability in the first two rows of Figure 5.3 and the SNR comparison in Figure 5.5's right panel. The images in Figure 5.4, derived from different wild-type mice using CMUT and piezoelectric transducer arrays, were captured following a single photostimulation to ensure complete dark adaptation. The highlighted region at the skull's top in Figure 5.4C might be influenced by minor blood presence at the skull/membrane junction. Despite this, the US resolution of the PACT modality ensured that the internal brain anatomies and response signals remained distinct from surface-level signals.

By imaging the coronal sections of the mouse brain, this study confirms the viability of using PACT and US images for accurate identification of the V1 and the subcortical SC, as well as for detecting visually induced hemodynamic responses in these areas. Although the sample size was limited, our findings indicate that the CMUT array yields a marginally enhanced SNR for V1 imaging, a conclusion backed by statistical analysis. Future studies with larger sample sizes will be informed by a power analysis of this preliminary group.

For 1D transducer arrays, sequential scanning is necessary to pinpoint relevant brain regions. CMUT's advancement to 2D matrix arrays could greatly streamline this process, allowing for full brain coverage through single-shot data collection. This approach paves the way for rapid, non-invasive evaluations of the mouse visual system, accelerating the identification of functional impairments in disease model mice.

5.5 Preliminary Study with Free-moving Mice

The feasibility of imaging mice in motion was demonstrated with a preliminary study using a prototype head-mounted probe. This device, illustrated in Figure 5.6a and b, is equipped with seven optical fibers (FMT600T, Thorlabs) arranged in two rows to provide PA illumination. Atop

the headmount, we positioned a 1D piezoelectric catheter US array (Acunav Siemens). This array, with a central frequency of 8MHz and a bandwidth ranging from 3 to 10 MHz, features 64 elements with a 0.1mm pitch. Additionally, LEDs were installed on either side of the headmount to facilitate retinal stimulation. To ensure effective ultrasonic coupling, the space within the headmount was filled with US gels before attaching it to the mouse's head. Ear pins were used to securely fix the headmount, aligning the imaging plane with the brain regions V1 and SC. The optical fibers and the cable of the catheter US array were connected to the sliding block in Figure 5.6d.

The headmount, weighing approximately 6 grams (excluding transducer cables and optical fibers), was balanced by a sliding rail system and a spring attached to the optical fibers. The mouse was placed in an 8cm x 30cm x 15cm cage, where it mainly moved along the rail but could also turn slightly left or right. To monitor the mouse's activity, two infrared LEDs, invisible to mice, were installed inside the cage, and an infrared camera recorded the activity (Figure 5.6d). The data were only captured when the mouse was stationary.

The system effectively detected visual-evoked hemodynamic responses (HR) in the V1 and SC regions, as shown in Figure 5.6e and f. Comparisons revealed that the average V1 and SC PA measurements from unanesthetized, freely moving mice (n=3) were about 90% ($p=8x10^{-5}$) and 50% (not statistically significant) higher in amplitude, respectively, compared to those from anesthetized mice (n=10). Notably, the SC responses in freely moving mice were less transient, which aligns with findings from hypothalamic spike recordings comparing free-moving versus anesthetized animals [18,19].

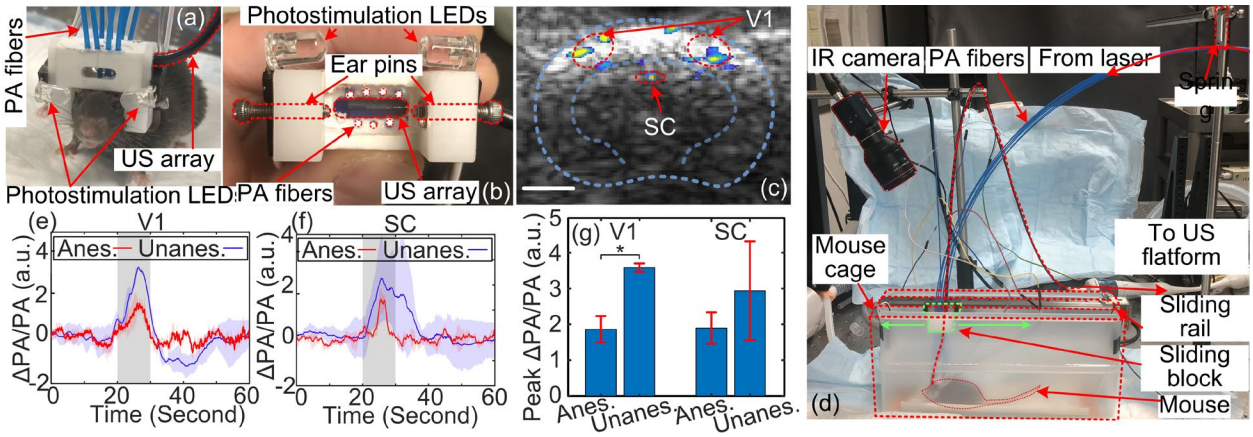

Figure 5.6 The prototype wearable PACT system. (a) A mouse with the headmount integrating PACT and US probe and the photostimulation LEDs. (b) Inner view of the headmount. The slot for the US array can fit one or two 1D catheter arrays, covering up to two imaging planes. (c) Functional maps acquired at a coronal plane containing V1 and SC. Scalebar: 2 mm. (d) Experiment setup. (e-f) Comparison between the PA signals in anesthetized (anes.) and unanesthetized, free-moving (unanes.) mice. The light sources for anesthetized and unanesthetized mice both had ~16.5 log photons $cm^{-2}s^{-1}$ corneal irradiance. (g) Statistics of peak ΔPA/PA acquired in anesthetized (n=10) and unanesthetized (n=3) mice. *p<1x10^{-4}.

5.6 Conclusion

This study marks a pioneering effort in employing PACT-US imaging to detect visual-evoked subcortical hemodynamic responses in the mouse brain. It shows that CMUT arrays, despite being miniaturized, do not compromise in performance compared to traditional piezoelectric arrays. A preliminary study using a wearable piezoelectric catheter array further demonstrates the feasibility of PACT for imaging free-moving mice.

5.7 Acknowledgements

We extend our sincere thanks to Prof. Ömer Oralkan's research group at North Carolina State University for their crucial role in this study. The development and fabrication of the CMUT array by their team were instrumental in advancing our research. Special acknowledgment is due

to Ermek Belekov for his expert assistance during the experimental phase. Their collaboration has been invaluable in enhancing the quality and scope of our work.

Chapter 6 Conclusions and Future Work

6.1 Summary of Major Findings

This dissertation has contributed substantially to the field of neuroscience through advanced photoacoustic (PA) imaging (PAI) techniques. It has successfully implemented and analyzed photoacoustic computed tomography (PACT) for brain imaging in mouse models, extending its application to non-human primate (NHP) models. It demonstrated the effectiveness of PACT and photoacoustic microscopy (PAM) in capturing intricate details of cerebral hemodynamics in both mice and NHPs. Notably, the comparative analysis of capacitive micromachined ultrasonic transducer (CMUT) and piezoelectric transducer arrays showed the technological advancements in this field, revealing their benefits and specific applications in neuroimaging, especially the development of wearable brain imaging device. The findings from these studies underscore the potential of PAI in bridging the gap between small animal studies and human clinical research, offering new insights into brain functions and disorders.

6.2 Contributions to the Field of Photoacoustic Imaging

The dissertation significantly advances PAI, particularly in neuroscience applications. It offers novel insights into the cerebral hemodynamics of small animal brains, which are crucial for understanding human brain disorders. The implementation of PACT in mouse models has revealed critical information in retinal disease research, enhancing our comprehension of brain

functionality. Extending this technology to NHPs has proven invaluable in studying more complex neurobiological processes, establishing a closer connection to human brain studies. Furthermore, the comparative analysis between CMUT and piezoelectric arrays in PAI has highlighted the strengths and limitations of each technology, guiding future developments in this field. These contributions have broadened the scope of neuroscience research and also paved the way for more sophisticated, non-invasive diagnostic tools.

6.3 Future Work

There are several avenues for further research emerge from this dissertation:

(1) The development of more compact, integrated PAI systems, particularly those that can be used in free-moving animal models, will be crucial. This advancement will enable more naturalistic studies of brain function, eliminating constraints imposed by anesthesia or physical restraints.

(2) Exploring multi-wavelength PAI techniques will enhance the ability to assess various aspects of brain functionality, such as blood oxygenation levels and metabolic rates, offering a more comprehensive view of cerebral hemodynamics.

(3) Advancements in CMUT technology, particularly in creating more sensitive and higher-resolution transducer arrays, will significantly improve image quality and depth penetration, allowing for more detailed insights into brain structures and functions.

(4) Integrating machine learning and deep learning algorithms in image processing can substantially enhance the quality and interpretability of PA images, leading to better diagnosis and understanding of neurological conditions.

(5) Translational research focused on adapting these PAI techniques for human clinical applications is imperative. This includes ensuring safety standards, optimizing imaging protocols, and validating the effectiveness of these methods in clinical settings.

(6) Finally, interdisciplinary collaborations between neuroscientists, engineers, and clinicians will be essential in pushing the boundaries of PAI and its applications in neuroscience, leading to groundbreaking discoveries and innovations in brain research and therapy.

Bibliography

[1] L.V. Wang, S. Hu, Photoacoustic Tomography: In Vivo Imaging from Organelles to Organs, Science. 335 (2012) 1458–1462.

[2] J. Yao, L. Wang, Photoacoustic brain imaging: from microscopic to macroscopic scales, Neurophotonics. 1 (2014) 011003.

[3] T. Wang, N. Sun, R. Cao, B. Ning, R. Chen, Q. Zhou, S. Hu, Multiparametric photoacoustic microscopy of the mouse brain with 300-kHz A-line rate, (n.d.).

[4] K.-W. Chang, Y. Zhu, H.M. Hudson, S. Barbay, D.J. Guggenmos, R.J. Nudo, X. Yang, X. Wang, Photoacoustic imaging of squirrel monkey cortical and subcortical brain regions during peripheral electrical stimulation, Photoacoustics. 25 (2022) 100326. https://doi.org/10.1016/j.pacs.2021.100326.

[5] M. Jeffrey, M. Lang, J. Gane, C. Wu, W.M. Burnham, L. Zhang, A reliable method for intracranial electrode implantation and chronic electrical stimulation in the mouse brain, BMC Neuroscience. 14 (2013) 82. https://doi.org/10.1186/1471-2202-14-82.

[6] J. Shah, S. Park, S. Aglyamov, T. Larson, L. Ma, K. Sokolov, K. Johnston, T. Milner, S.Y. Emelianov, Photoacoustic imaging and temperature measurement for photothermal cancer therapy., J Biomed Opt. 13 (2008) 034024. https://doi.org/10.1117/1.2940362.

[7] M. Xu, L.V. Wang, Universal back-projection algorithm for photoacoustic computed tomography., Phys Rev E Stat Nonlin Soft Matter Phys. 71 (2005) 016706. https://doi.org/10.1103/PhysRevE.71.016706.

[8] L.V. Wang, Multiscale photoacoustic microscopy and computed tomography, Nature Photonics. 3 (2009) 503–509. https://doi.org/10.1038/nphoton.2009.157.

[9] A. Petschke, P.J. La Rivière, Comparison of photoacoustic image reconstruction algorithms using the channelized Hotelling observer., J Biomed Opt. 18 (2013) 26009. https://doi.org/10.1117/1.JBO.18.2.026009.

[10] J. Won, L.Y. Shi, W. Hicks, J. Wang, R. Hurd, J.K. Naggert, B. Chang, P.M. Nishina, Mouse model resources for vision research., J Ophthalmol. 2011 (2011) 391384. https://doi.org/10.1155/2011/391384.

[11] J. Won, L.Y. Shi, W. Hicks, J. Wang, J.K. Naggert, P.M. Nishina, Translational vision research models program., Adv Exp Med Biol. 723 (2012) 391–397. https://doi.org/10.1007/978-1-4614-0631-0_50.

[12] T.M. Brown, C. Gias, M. Hatori, S.R. Keding, M. Semo, P.J. Coffey, J. Gigg, H.D. Piggins, S. Panda, R.J. Lucas, Melanopsin Contributions to Irradiance Coding in the Thalamo-Cortical Visual System, PLOS Biology. 8 (2010) e1000558. https://doi.org/10.1371/journal.pbio.1000558.

[13] W.H. Ridder, S. Nusinowitz, The visual evoked potential in the mouse—Origins and response characteristics, Vision Research. 46 (2006) 902–913. https://doi.org/10.1016/j.visres.2005.09.006.

[14] A. Niranjan, I.N. Christie, S.G. Solomon, J.A. Wells, M.F. Lythgoe, fMRI mapping of the visual system in the mouse brain with interleaved snapshot GE-EPI, NeuroImage. 139 (2016) 337–345.
[15] S.S. Eckley, J.S. Villano, N.S. Kuo, K.Y. Wong, Acepromazine and Chlorpromazine as Pharmaceutical-grade Alternatives to Chlorprothixene for Pupillary Light Reflex Imaging in Mice, Journal of the American Association for Laboratory Animal Science. 59 (2020) 197–203.
[16] H. Zeng, Y. Jiang, S. Beer-Hammer, X. Yu, Awake Mouse fMRI and Pupillary Recordings in the Ultra-High Magnetic Field., Front Neurosci. 16 (2022) 886709. https://doi.org/10.3389/fnins.2022.886709.
[17] J.H. Meijer, K. Watanabe, J. Schaap, H. Albus, L. Détári, Light Responsiveness of the Suprachiasmatic Nucleus: Long-Term Multiunit and Single-Unit Recordings in Freely Moving Rats, Journal of Neuroscience. 18 (1998) 9078–9087. https://doi.org/10.1523/JNEUROSCI.18-21-09078.1998.
[18] H.C. van Diepen, A. Ramkisoensing, S.N. Peirson, R.G. Foster, J.H. Meijer, Irradiance encoding in the suprachiasmatic nuclei by rod and cone photoreceptors., FASEB J. 27 (2013) 4204–4212. https://doi.org/10.1096/fj.13-233098.
[19] E. Drouyer, C. Rieux, R.A. Hut, H.M. Cooper, Responses of suprachiasmatic nucleus neurons to light and dark adaptation: relative contributions of melanopsin and rod-cone inputs., J Neurosci. 27 (2007) 9623–9631. https://doi.org/10.1523/JNEUROSCI.1391-07.2007.
[20] R.N.S. Sachdev, G.C. Champney, H. Lee, R.R. Price, D.R. 3rd Pickens, V.L. Morgan, J.D. Stefansic, P. Melzer, F.F. Ebner, Experimental model for functional magnetic resonance imaging of somatic sensory cortex in the unanesthetized rat., Neuroimage. 19 (2003) 742–750. https://doi.org/10.1016/s1053-8119(03)00093-4.
[21] C. Lee, T.A. Jones, Effects of Several Therapeutic Agents on Mammalian Vestibular Function: Meclizine, Diazepam, and JNJ7777120., J Assoc Res Otolaryngol. 22 (2021) 527–549. https://doi.org/10.1007/s10162-021-00803-5.
[22] B. Drexler, S. Zinser, H. Hentschke, B. Antkowiak, Diazepam Decreases Action Potential Firing of Neocortical Neurons via Two Distinct Mechanisms, Anesthesia & Analgesia. 111 (2010). https://journals.lww.com/anesthesia-analgesia/fulltext/2010/12000/diazepam_decreases_action_potential_firing_of.11.aspx.
[23] M.-C. Shin, M. Wakita, D.-J. Xie, S. Iwata, N. Akaike, Synergic effect of diazepam and muscimol via presynaptic GABA(A) receptors on glutamatergic evoked EPSCs., Brain Res. 1416 (2011) 1–9. https://doi.org/10.1016/j.brainres.2011.07.054.
[24] C. Kopp, U. Rudolph, K. Löw, I. Tobler, Modulation of rhythmic brain activity by diazepam: GABA(A) receptor subtype and state specificity., Proc Natl Acad Sci U S A. 101 (2004) 3674–3679. https://doi.org/10.1073/pnas.0306975101.
[25] N. Pivac, D. Perić, Inhibitory effect of diazepam on the activity of the hypothalamic-pituitary-adrenal axis in female rats., J Neural Transm Gen Sect. 92 (1993) 173–186. https://doi.org/10.1007/BF01244876.
[26] M. Higashima, H. Kinoshita, Y. Koshino, Differences in the effects of zolpidem and diazepam on recurrent inhibition and long-term potentiation in rat hippocampal slices., Neurosci Lett. 245 (1998) 77–80. https://doi.org/10.1016/s0304-3940(98)00178-5.
[27] M.P. Arolfo, J.D. Brioni, Diazepam impairs place learning in the Morris water maze., Behav Neural Biol. 55 (1991) 131–136. https://doi.org/10.1016/0163-1047(91)80133-y.

[28] I. Jurna, Depression of nociceptive sensory activity in the rat spinal cord due to the intrathecal administration of drugs: effect of diazepam., Neurosurgery. 15 (1984) 917–920.
[29] G. Strangman, J.P. Culver, J.H. Thompson, D.A. Boas, A Quantitative Comparison of Simultaneous BOLD fMRI and NIRS Recordings during Functional Brain Activation, NeuroImage. 17 (2002) 719–731. https://doi.org/10.1006/nimg.2002.1227.
[30] D. Das, K. Sivasubramanian, P. Rajendran, M. Pramanik, Label-free high frame rate imaging of circulating blood clots using a dual modal ultrasound and photoacoustic system., J Biophotonics. 14 (2021) e202000371. https://doi.org/10.1002/jbio.202000371.
[31] M. Nasiriavanaki, J. Xia, H. Wan, A.Q. Bauer, J.P. Culver, L.V. Wang, High-resolution photoacoustic tomography of resting-state functional connectivity in the mouse brain, Proceedings of the National Academy of Sciences. (2013). http://www.pnas.org/content/early/2013/12/18/1311868111.abstract.
[32] P. Zhang, L. Li, L. Lin, P. Hu, J. Shi, Y. He, L. Zhu, Y. Zhou, L.V. Wang, High-resolution deep functional imaging of the whole mouse brain by photoacoustic computed tomography in vivo, Journal of Biophotonics. 11 (2018) e201700024.
[33] J. Tang, L. Xi, J. Zhou, H. Huang, T. Zhang, P.R. Carney, H. Jiang, Noninvasive high-speed photoacoustic tomography of cerebral hemodynamics in awake-moving rats, Journal of Cerebral Blood Flow and Metabolism : Official Journal of the International Society of Cerebral Blood Flow and Metabolism. 35 (2015) 1224–1232.
[34] S. Gottschalk, O. Degtyaruk, B. Mc Larney, J. Rebling, M.A. Hutter, X.L. Deán-Ben, S. Shoham, D. Razansky, Rapid volumetric optoacoustic imaging of neural dynamics across the mouse brain., Nat Biomed Eng. 3 (2019) 392–401. https://doi.org/10.1038/s41551-019-0372-9.
[35] J. Tang, J.E. Coleman, X. Dai, H. Jiang, Wearable 3-D Photoacoustic Tomography for Functional Brain Imaging in Behaving Rats., Sci Rep. 6 (2016) 25470. https://doi.org/10.1038/srep25470.
[36] K.A. Phillips, K.L. Bales, J.P. Capitanio, A. Conley, P.W. Czoty, B.A. t Hart, W.D. Hopkins, S.L. Hu, L.A. Miller, M.A. Nader, P.W. Nathanielsz, J. Rogers, C.A. Shively, M.L. Voytko, Why primate models matter, Am J Primatol. 76 (2014) 801–27.
[37] S. Sani, D. Traul, A. Klink, N. Niaraki, A. Gonzalo-Ruiz, C.K. Wu, C. Geula, Distribution, progression and chemical composition of cortical amyloid-beta deposits in aged rhesus monkeys: similarities to the human, Acta Neuropathol. 105 (2003) 145–56.
[38] G.A. Orban, D. Van Essen, W. Vanduffel, Comparative mapping of higher visual areas in monkeys and humans, Trends in Cognitive Sciences. 8 (2004) 315–324.
[39] D. Koshiyama, M. Fukunaga, N. Okada, F. Yamashita, H. Yamamori, Y. Yasuda, M. Fujimoto, K. Ohi, H. Fujino, Y. Watanabe, K. Kasai, R. Hashimoto, Role of subcortical structures on cognitive and social function in schizophrenia, Scientific Reports. 8 (2018) 1183.
[40] P.M. Matthews, G.D. Honey, E.T. Bullmore, Applications of fMRI in translational medicine and clinical practice, Nature Reviews Neuroscience. 7 (2006) 732–744.
[41] A. Van der Linden, N. Van Camp, P. Ramos-Cabrer, M. Hoehn, Current status of functional MRI on small animals: application to physiology, pathophysiology, and cognition, Nmr in Biomedicine. 20 (2007) 522–545.
[42] N.K. Logothetis, What we can do and what we cannot do with fMRI, Nature. 453 (2008) 869–878.

[43] J. Hua, R.D. Stevens, A.J. Huang, J.J. Pekar, P.C.M. van Zijl, Physiological origin for the BOLD poststimulus undershoot in human brain: vascular compliance versus oxygen metabolism, Journal of Cerebral Blood Flow and Metabolism. 31 (2011) 1599–1611.
[44] J.M. Lawrence, J. Kornelsen, P.W. Stroman, Noninvasive observation of cervical spinal cord activity in children by functional MRI during cold thermal stimulation, Magnetic Resonance Imaging. 29 (2011) 813–818.
[45] K.M. Vogt, J.W. Ibinson, P. Schmalbrock, R.H. Small, The impact of physiologic noise correction applied to functional MRI of pain at 1.5 and 3.0 T, Magnetic Resonance Imaging. 29 (2011) 819–826.
[46] P.D. Gamlin, M.K. Ward, M.S. Bolding, J.K. Grossmann, D.B. Twieg, Developing functional magnetic resonance imaging techniques for alert macaque monkeys, Methods. 38 (2006) 210–220.
[47] J. Pfeuffer, A. Shmuel, G.A. Keliris, T. Steudel, H. Merkle, N.K. Logothetis, Functional MR imaging in the awake monkey: effects of motion on dynamic off-resonance and processing strategies, Magnetic Resonance Imaging. 25 (2007) 869–882.
[48] J.B.M. Goense, K. Whittingstall, N.K. Logothetis, Functional magnetic resonance imaging of awake behaving macaques, Methods. 50 (2010) 178–188.
[49] M.A. Pinsk, T. Moore, M.C. Richter, C.G. Gross, S. Kastner, Methods for functional magnetic resonance imaging in normal and lesioned behaving monkeys, Journal of Neuroscience Methods. 143 (2005) 179–195.
[50] G. Strangman, D.A. Boas, J.P. Sutton, Non-invasive neuroimaging using near-infrared light, Biological Psychiatry. 52 (2002) 679–693.
[51] J.P. Culver, A.M. Siegel, J.J. Stott, D.A. Boas, Volumetric diffuse optical tomography of brain activity, Optics Letters. 28 (2003) 2061–2063.
[52] T. Durduran, M.G. Burnett, G.Q. Yu, C. Zhou, D. Furuya, A.G. Yodh, J.A. Detre, J.H. Greenberg, Spatiotemporal quantification of cerebral blood flow during functional activation in rat somatosensory cortex using laser-speckle flowmetry, Journal of Cerebral Blood Flow and Metabolism. 24 (2004) 518–525.
[53] S.A. Sheth, M. Nemoto, M. Guiou, M. Walker, N. Pouratian, A.W. Toga, Linear and nonlinear relationships between neuronal activity, oxygen metabolism, and hemodynamic responses, Neuron. 42 (2004) 347–355.
[54] S. Yuan, A. Devor, D.A. Boas, A.K. Dunn, Determination of optimal exposure time for imaging of blood flow changes with laser speckle contrast imaging, Applied Optics. 44 (2005) 1823–1830.
[55] A.P. Gibson, J.C. Hebden, S.R. Arridge, Recent advances in diffuse optical imaging, Physics in Medicine and Biology. 50 (2005) R1–R43.
[56] B.W. Zeff, B.R. White, H. Dehghani, B.L. Schlaggar, J.P. Culver, Retinotopic mapping of adult human visual cortex with high-density diffuse optical tomography, Proceedings of the National Academy of Sciences of the United States of America. 104 (2007) 12169–12174.
[57] P.B. Jones, H.K. Shin, D.A. Boas, B.T. Hyman, M.A. Moskowitz, C. Ayata, A.K. Dunn, Simultaneous multispectral reflectance imaging and laser speckle flowmetry of cerebral blood flow and oxygen metabolism in focal cerebral ischemia, Journal of Biomedical Optics. 13 (2008). http://www.ncbi.nlm.nih.gov/pubmed/19021335.

[58] A. Grinvald, R.D. Frostig, R.M. Siegel, E. Bartfeld, High-resolution optical imaging of functional brain architecture in the awake monkey, Proceedings of the National Academy of Sciences. 88 (1991) 11559.
[59] N. Vnek, B.M. Ramsden, C.P. Hung, P.S. Goldman-Rakic, A.W. Roe, Optical imaging of functional domains in the cortex of the awake and behaving monkey, Proceedings of the National Academy of Sciences of the United States of America. 96 (1999) 4057–4060.
[60] A. Dizeux, M. Gesnik, H. Ahnine, K. Blaize, F. Arcizet, S. Picaud, J.A. Sahel, T. Deffieux, P. Pouget, M. Tanter, Functional ultrasound imaging of the brain reveals propagation of task-related brain activity in behaving primates, Nat Commun. 10 (2019) 1400.
[61] G. Ku, L.H.V. Wang, Deeply penetrating photoacoustic tomography in biological tissues enhanced with an optical contrast agent, Optics Letters. 30 (2005) 507–509.
[62] C. Kim, T.N. Erpelding, L. Jankovic, M.D. Pashley, L.V. Wang, Deeply penetrating in vivo photoacoustic imaging using a clinical ultrasound array system, Biomed. Opt. Express. 1 (2010) 278–284.
[63] X.D. Wang, Y.J. Pang, G. Ku, X.Y. Xie, G. Stoica, L.H.V. Wang, Noninvasive laser-induced photoacoustic tomography for structural and functional in vivo imaging of the brain, Nature Biotechnology. 21 (2003) 803–806.
[64] E.W. Stein, K. Maslov, L.V. Wang, Noninvasive mapping of the electrically stimulated mouse brain using photoacoustic microscopy, in: SPIE, San Jose, 2008: pp. 68561J–1. http://144.206.159.178/ft/CONF/16410363/16410415.pdf.
[65] X.M. Yang, L.V. Wang, Monkey brain cortex imaging by photoacoustic tomography, Journal of Biomedical Optics. 13 (2008) 044009.
[66] X.M. Yang, A. Maurudis, J. Gamelin, A. Aguirre, Q. Zhu, L.V. Wang, Photoacoustic tomography of small animal brain with a curved array transducer, Journal of Biomedical Optics. 14 (2009) 054007.
[67] J. Staley, P. Grogan, A.K. Samadi, H.Z. Cui, M.S. Cohen, X.M. Yang, Growth of melanoma brain tumors monitored by photoacoustic microscopy, Journal of Biomedical Optics. 15 (2010) Article No. 040510.
[68] J. Jo, X. Yang, Detection of cocaine induced rat brain activation by photoacoustic tomography, Journal of Neuroscience Methods. 195 (2011) 232–235.
[69] J. Jo, H. Zhang, P.D. Cheney, X. Yang, Photoacoustic detection of functional responses in the motor cortex of awake behaving monkey during forelimb movement, Journal of Biomedical Optics. 17 (2012) 110503–110503.
[70] Y. Liu, H. Liu, H. Yan, Y. Liu, J. Zhang, W. Shan, P. Lai, H. Li, L. Ren, Z. Li, L. Nie, Aggregation-Induced Absorption Enhancement for Deep Near-Infrared II Photoacoustic Imaging of Brain Gliomas In Vivo, Advanced Science. 6 (2019) 1801615.
[71] L. Li, L. Zhu, C. Ma, L. Lin, J. Yao, L. Wang, K. Maslov, R. Zhang, W. Chen, J. Shi, L.V. Wang, Single-impulse panoramic photoacoustic computed tomography of small-animal whole-body dynamics at high spatiotemporal resolution, Nature Biomedical Engineering. 1 (2017) 0071.
[72] W. Xia, D. Piras, M.K.A. Singh, J.C.G. van Hespen, T.G. van Leeuwen, W. Steenbergen, S. Manohar, Design and evaluation of a laboratory prototype system for 3D photoacoustic full breast tomography, Biomedical Optics Express. 4 (2013) 2555–2569.

[73] Y. Zhu, G. Xu, J. Yuan, J. Jo, G. Gandikota, H. Demirci, T. Agano, N. Sato, Y. Shigeta, X. Wang, Light Emitting Diodes based Photoacoustic Imaging and Potential Clinical Applications, Scientific Reports. 8 (2018) 9885.
[74] W. Choi, E.-Y. Park, S. Jeon, Y. Yang, B. Park, J. Ahn, S. Cho, C. Lee, D.-K. Seo, J.-H. Cho, C. Kim, Three-dimensional Multistructural Quantitative Photoacoustic and US Imaging of Human Feet in Vivo, Radiology. 303 (2022) 467–473.
[75] L. Song, C. Kim, K. Maslov, K.K. Shung, L.V. Wang, High-speed dynamic 3D photoacoustic imaging of sentinel lymph node in a murine model using an ultrasound array, Medical Physics. 36 (2009) 3724–3729.
[76] Y. Asao, K. Nagae, K. Miyasaka, H. Sekiguchi, S. Aiso, S. Watanabe, M. Sato, S. Kizaka-Kondoh, Y. Nakajima, K. Kishi, T. Yagi, In Vivo Label-Free Observation of Tumor-Related Blood Vessels in Small Animals Using a Newly Designed Photoacoustic 3D Imaging System, Ultrasonic Imaging. 44 (2022) 96–104.
[77] X. Zhang, F.Y. Yamaner, Ö. Oralkan, Fabrication of Vacuum-Sealed Capacitive Micromachined Ultrasonic Transducers With Through-Glass-Via Interconnects Using Anodic Bonding, Journal of Microelectromechanical Systems. 26 (2017) 226–234.
[78] M. Shin, J.S. Krause, P. DeBitetto, R.D. White, Acoustic Doppler velocity measurement system using capacitive micromachined ultrasound transducer array technology, J Acoust Soc Am. 134 (2013) 1011–20.
[79] C. Tekes, J. Zahorian, G. Gurun, S. Satir, T. Xu, M. Hochman, F.L. Degertekin, Volumetric imaging using single chip integrated CMUT-on-CMOS IVUS array, in: 2012 Annual International Conference of the IEEE Engineering in Medicine and Biology Society, IEEE, 2012: pp. 3195–3198.
[80] J. Chen, M. Wang, J.C. Cheng, Y.H. Wang, P.C. Li, X. Cheng, A photoacoustic imager with light illumination through an infrared-transparent silicon CMUT array, IEEE Trans Ultrason Ferroelectr Freq Control. 59 (2012) 766–75.
[81] S. Vaithilingam, T.J. Ma, Y. Furukawa, I.O. Wygant, X. Zhuang, A. De La Zerda, O. Oralkan, A. Kamaya, S.S. Gambhir, R.B. Jeffrey, B.T. Khuri-Yakub, Three-dimensional photoacoustic imaging using a two-dimensional CMUT array, IEEE Trans Ultrason Ferroelectr Freq Control. 56 (2009) 2411–9.
[82] B. Bayram, O. Oralkan, A.S. Ergun, E. Haeggstrom, G.G. Yaralioglu, B.T. Khuri-Yakub, Capacitive micromachined ultrasonic transducer design for high power transmission, IEEE Trans Ultrason Ferroelectr Freq Control. 52 (2005) 326–39.
[83] B.T. Khuri-Yakub, O. Oralkan, Capacitive micromachined ultrasonic transducers for medical imaging and therapy, J Micromech Microeng. 21 (2011) 54004–54014.
[84] S.H. Wong, M. Kupnik, R.D. Watkins, K. Butts-Pauly, B.T. Khuri-Yakub, Capacitive micromachined ultrasonic transducers for therapeutic ultrasound applications, IEEE Trans Biomed Eng. 57 (2010) 114–23.
[85] A.S. Erguri, Y. Huang, X. Zhuang, O. Oralkan, G.G. Yarahoglu, B.T. Khuri-Yakub, Capacitive micromachined ultrasonic transducers: Fabrication technology, IEEE Transactions on Ultrasonics, Ferroelectrics, and Frequency Control. 52 (2005) 2242–2258.
[86] O. Oralkan, X. Jin, F.L. Degertekin, B.T. Khuri-Yakub, Simulation and experimental characterization of a 2-D capacitive micromachined ultrasonic transducer array element, IEEE Trans Ultrason Ferroelectr Freq Control. 46 (1999) 1337–40.

[87] A. Savoia, G. Calianov, M. Pappalardo, A CMUT probe for medical ultrasonography: from microfabrication to system integration, IEEE Trans Ultrason Ferroelectr Freq Control. 59 (2012) 1127–38.
[88] A. Novell, J.M. Escoffre, A. Bouakaz, Second harmonic and subharmonic for non-linear wideband contrast imaging using a capacitive micromachined ultrasonic transducer array, Ultrasound Med Biol. 39 (2013) 1500–12.
[89] O. Oralkan, A.S. Ergun, J.A. Johnson, M. Karaman, U. Demirci, K. Kaviani, T.H. Lee, B.T. Khuri-Yakub, Capacitive micromachined ultrasonic transducers: next-generation arrays for acoustic imaging?, IEEE Trans Ultrason Ferroelectr Freq Control. 49 (2002) 1596–610.
[90] J.L. Sanders, A.Ö. Biliroğlu, I.G. Newsome, O.J. Adelegan, F.Y. Yamaner, P.A. Dayton, Ö. Oralkan, A Handheld Imaging Probe for Acoustic Angiography With an Ultrawideband Capacitive Micromachined Ultrasonic Transducer (CMUT) Array, IEEE Transactions on Ultrasonics, Ferroelectrics, and Frequency Control. 69 (2022) 2318–2330.
[91] E. Belekov, K.J. Bautista, M. Annayev, O.J. Adelegan, A.O. Biliroglu, T.M. Kierski, J.L. Sanders, R.E. Kemal, E. Sennik, F.Y. Yamaner, Performance Assessment of Ultra-Wideband and Dual-Mode 1D CMUT Arrays for Acoustic Angiography, in: 2022 IEEE International Ultrasonics Symposium (IUS), IEEE, 2022: pp. 1–4.
[92] C. Seok, F.Y. Yamaner, M. Sahin, O. Oralkan, A Wearable Ultrasonic Neurostimulator - Part I: A 1D CMUT Phased Array System for Chronic Implantation in Small Animals, IEEE Transactions on Biomedical Circuits and Systems. 15 (2021) 692–704.
[93] C. Seok, O.J. Adelegan, A.Ö. Biliroğlu, F.Y. Yamaner, O. Oralkan, A Wearable Ultrasonic Neurostimulator—Part II: A 2D CMUT Phased Array System With a Flip-Chip Bonded ASIC, IEEE Transactions on Biomedical Circuits and Systems. 15 (2021) 705–718.
[94] Y. Ma, J. Bao, Y. Zhang, Z. Li, X. Zhou, C. Wan, L. Huang, Y. Zhao, G. Han, T. Xue, Mammalian Near-Infrared Image Vision through Injectable and Self-Powered Retinal Nanoantennae, Cell. 177 (2019) 243-255.e15. https://doi.org/10.1016/j.cell.2019.01.038.
[95] D.-G. Luo, W.W.S. Yue, P. Ala-Laurila, K.-W. Yau, Activation of visual pigments by light and heat., Science. 332 (2011) 1307–1312. https://doi.org/10.1126/science.1200172.
[96] M.J. McKeown, L.K. Hansen, T.J. Sejnowsk, Independent component analysis of functional MRI: what is signal and what is noise?, Current Opinion in Neurobiology. 13 (2003) 620–629.
[97] L. Gagnon, K. Perdue, D.N. Greve, D. Goldenholz, G. Kaskhedikar, D.A. Boas, Improved recovery of the hemodynamic response in diffuse optical imaging using short optode separations and state-space modeling, NeuroImage. 56 (2011) 1362–1371.
[98] L. Gagnon, M.A. Yücel, D.A. Boas, R.J. Cooper, Further improvement in reducing superficial contamination in NIRS using double short separation measurements, NeuroImage. 85 (2014) 127–135.
[99] W.H. Lee, Z. Liu, B.A. Mueller, K. Lim, B. He, Influence of white matter anisotropic conductivity on EEG source localization: Comparison to fMRI in human primary visual cortex, Clinical Neurophysiology. 120 (2009) 2071–2081.
[100] K. Han, H. Wen, J. Shi, K.-H. Lu, Y. Zhang, D. Fu, Z. Liu, Variational autoencoder: An unsupervised model for encoding and decoding fMRI activity in visual cortex, NeuroImage. 198 (2019) 125–136.

[101] Z. Liu, N. Zhang, W. Chen, B. He, Mapping the bilateral visual integration by EEG and fMRI, NeuroImage. 46 (2009) 989–997.
[102] A. von Lühmann, A. Ortega-Martinez, D.A. Boas, M.A. Yücel, Using the General Linear Model to Improve Performance in fNIRS Single Trial Analysis and Classification: A Perspective, Frontiers in Human Neuroscience. 14 (2020). https://www.frontiersin.org/articles/10.3389/fnhum.2020.00030.
[103] A. von Lühmann, X. Li, K.-R. Müller, D.A. Boas, M.A. Yücel, Improved physiological noise regression in fNIRS: A multimodal extension of the General Linear Model using temporally embedded Canonical Correlation Analysis, NeuroImage. 208 (2020) 116472.
[104] R. Henson, K. Friston, Convolution models for fMRI, Statistical Parametric Mapping: The Analysis of Functional Brain Images. (2007) 178–192.
[105] T. Jin, S.-G. Kim, Cortical layer-dependent dynamic blood oxygenation, cerebral blood flow and cerebral blood volume responses during visual stimulation, NeuroImage. 43 (2008) 1–9.
[106] M. Havlicek, D. Ivanov, A. Roebroeck, K. Uludağ, Determining Excitatory and Inhibitory Neuronal Activity from Multimodal fMRI Data Using a Generative Hemodynamic Model, Frontiers in Neuroscience. 11 (2017). https://www.frontiersin.org/articles/10.3389/fnins.2017.00616.
[107] F. Cignetti, E. Salvia, J.-L. Anton, M.-H. Grosbras, C. Assaiante, Pros and Cons of Using the Informed Basis Set to Account for Hemodynamic Response Variability with Developmental Data, Frontiers in Neuroscience. 10 (2016). https://www.frontiersin.org/articles/10.3389/fnins.2016.00322.
[108] D.H. Kim, K.-D. Lee, T.C. Bulea, H.-S. Park, Increasing motor cortex activation during grasping via novel robotic mirror hand therapy: a pilot fNIRS study, Journal of NeuroEngineering and Rehabilitation. 19 (2022) 8.
[109] V.D. Calhoun, M.C. Stevens, G.D. Pearlson, K.A. Kiehl, fMRI analysis with the general linear model: removal of latency-induced amplitude bias by incorporation of hemodynamic derivative terms, NeuroImage. 22 (2004) 252–257.
[110] H. Lambers, M. Segeroth, F. Albers, L. Wachsmuth, T.M. van Alst, C. Faber, A cortical rat hemodynamic response function for improved detection of BOLD activation under common experimental conditions, NeuroImage. 208 (2020) 116446.
[111] M.A. Lindquist, J. Meng Loh, L.Y. Atlas, T.D. Wager, Modeling the hemodynamic response function in fMRI: Efficiency, bias and mis-modeling, NeuroImage. 45 (2009) S187–S198.
[112] A.D. Güler, J.L. Ecker, G.S. Lall, S. Haq, C.M. Altimus, H.W. Liao, A.R. Barnard, H. Cahill, T.C. Badea, H. Zhao, M.W. Hankins, D.M. Berson, R.J. Lucas, K.W. Yau, S. Hattar, Melanopsin cells are the principal conduits for rod-cone input to non-image-forming vision, Nature. 453 (2008) 102–5.
[113] D. Göz, K. Studholme, D.A. Lappi, M.D. Rollag, I. Provencio, L.P. Morin, Targeted destruction of photosensitive retinal ganglion cells with a saporin conjugate alters the effects of light on mouse circadian rhythms, PLoS One. 3 (2008) e3153.
[114] M. Hatori, H. Le, C. Vollmers, S.R. Keding, N. Tanaka, T. Buch, A. Waisman, C. Schmedt, T. Jegla, S. Panda, Inducible ablation of melanopsin-expressing retinal ganglion cells reveals their central role in non-image forming visual responses, PLoS One. 3 (2008) e2451.

[115] D.M. Berson, F.A. Dunn, M. Takao, Phototransduction by Retinal Ganglion Cells That Set the Circadian Clock, Science. 295 (2002) 1070–1073.
[116] R.J. Nudo, W.M. Jenkins, M.M. Merzenich, T. Prejean, R. Grenda, Neurophysiological correlates of hand preference in primary motor cortex of adult squirrel monkeys, J Neurosci. 12 (1992) 2918–47.
[117] R.J. Nudo, G.W. Milliken, Reorganization of movement representations in primary motor cortex following focal ischemic infarcts in adult squirrel monkeys, J Neurophysiol. 75 (1996) 2144–9.
[118] S.B. Frost, S. Barbay, K.M. Friel, E.J. Plautz, R.J. Nudo, Reorganization of remote cortical regions after ischemic brain injury: a potential substrate for stroke recovery, J Neurophysiol. 89 (2003) 3205–14.
[119] R.J. Nudo, Remodeling of cortical motor representations after stroke: implications for recovery from brain damage, Mol Psychiatry. 2 (1997) 188–91.
[120] S. Barbay, E.K. Peden, G. Falchook, R.J. Nudo, Sensitivity of neurons in somatosensory cortex (S1) to cutaneous stimulation of the hindlimb immediately following a sciatic nerve crush, Somatosens Mot Res. 16 (1999) 103–14.
[121] N. Dancause, S. Barbay, S.B. Frost, E.J. Plautz, D. Chen, E.V. Zoubina, A.M. Stowe, R.J. Nudo, Extensive cortical rewiring after brain injury, J Neurosci. 25 (2005) 10167–79.
[122] M. Schwarz, N. Garzorz-Stark, K. Eyerich, J. Aguirre, V. Ntziachristos, Motion correction in optoacoustic mesoscopy, Scientific Reports. 7 (2017) 10386.
[123] J. Aguirre, A. Berezhnoi, H. He, M. Schwarz, B. Hindelang, M. Omar, V. Ntziachristos, Motion Quantification and Automated Correction in Clinical RSOM, IEEE Transactions on Medical Imaging. 38 (2019) 1340–1346.
[124] X. Ma, M. Cao, Q. Shen, J. Yuan, T. Feng, Q. Cheng, X. Wang, A.R. Washabaugh, N.A. Baker, C.N. Lumeng, R.W. O'Rourke, Adipocyte Size Evaluation Based on Photoacoustic Spectral Analysis Combined with Deep Learning Method, Applied Sciences. 8 (2018). https://doi.org/10.3390/app8112178.
[125] A. Hauptmann, F. Lucka, M. Betcke, N. Huynh, J. Adler, B. Cox, P. Beard, S. Ourselin, S. Arridge, Model-based learning for accelerated, limited-view 3-D photoacoustic tomography, IEEE Transactions on Medical Imaging. 37 (2018) 1382–1393.
[126] S. Antholzer, M. Haltmeier, J. Schwab, Deep learning for photoacoustic tomography from sparse data, Inverse Problems in Science and Engineering. 27 (2019) 987–1005. https://doi.org/10.1080/17415977.2018.1518444.
[127] J. Gröhl, M. Schellenberg, K. Dreher, L. Maier-Hein, Deep learning for biomedical photoacoustic imaging: A review, Photoacoustics. 22 (2021) 100241. https://doi.org/10.1016/j.pacs.2021.100241.
[128] J. Yang, S. Rahardja, P. Fränti, Outlier Detection: How to Threshold Outlier Scores?, in: Proceedings of the International Conference on Artificial Intelligence, Information Processing and Cloud Computing, Association for Computing Machinery, New York, NY, USA, 2019. https://doi.org/10.1145/3371425.3371427.
[129] J.A. Gergen, P.D. MacLean, H. National Institutes of, A stereotaxic atlas of the squirrel monkey's brain (Saimiri sciureus), U.S. Department of Health, Education, and Welfare, Public Health Service, National Institutes of Health, Bethesda, Md. :, 1962. https://www.biodiversitylibrary.org/item/198767.
[130] L.M. Chen, G.H. Turner, R.M. Friedman, N. Zhang, J.C. Gore, A.W. Roe, M.J. Avison, High-Resolution Maps of Real and Illusory Tactile Activation in Primary Somatosensory

Cortex in Individual Monkeys with Functional Magnetic Resonance Imaging and Optical Imaging, The Journal of Neuroscience. 27 (2007) 9181.
[131] R. Wu, L. Su, P.-F. Yang, L. Min Chen, Altered Spatiotemporal Dynamics of Cortical Activation to Tactile Stimuli in Somatosensory Area 3b and Area 1 of Monkeys after Spinal Cord Injury, Eneuro. 3 (2016) ENEURO.0095-16.2016.
[132] R. Anna Wang, E.W. Jeremy, M.F. Robert, Study of single and multidigit activation in monkey somatosensory cortex using voltage-sensitive dye imaging, Neurophotonics. 4 (2017) 1–9.
[133] J. Prakash, A.S. Raju, C.B. Shaw, M. Pramanik, P.K. Yalavarthy, Basis pursuit deconvolution for improving model-based reconstructed images in photoacoustic tomography, Biomedical Optics Express. 5 (2014) 1363–1377.
[134] N. Awasthi, G. Jain, S.K. Kalva, M. Pramanik, P.K. Yalavarthy, Deep neural network-based sinogram super-resolution and bandwidth enhancement for limited-data photoacoustic tomography, IEEE Transactions on Ultrasonics, Ferroelectrics, and Frequency Control. 67 (2020) 2660–2673.
[135] S. Guan, A.A. Khan, S. Sikdar, P.V. Chitnis, Fully dense UNet for 2-D sparse photoacoustic tomography artifact removal, IEEE Journal of Biomedical and Health Informatics. 24 (2019) 568–576.
[136] Z. Wang, A.C. Bovik, H.R. Sheikh, E.P. Simoncelli, Image quality assessment: from error visibility to structural similarity, IEEE Transactions on Image Processing. 13 (2004) 600–612.
[137] J.L. Sanders, A.Ö. Biliroğlu, I.G. Newsome, O.J. Adelegan, F.Y. Yamaner, P.A. Dayton, O. Ö, An Ultra-Wideband Capacitive Micromachined Ultrasonic Transducer (CMUT) Array for Acoustic Angiography: Preliminary Results, 2020 IEEE International Ultrasonics Symposium (IUS). (2020) 1–3.
[138] M. Roumeliotis, P. Ephrat, J. Patrick, J.J.L. Carson, Development and characterization of an omni-directional photoacoustic point source for calibration of a staring 3D photoacoustic imaging system, Optics Express. 17 (2009) 15228–15238.
[139] A. Danish, B. Niels, F. Eberhard, L. Nikos, S. Ranganatha, The hemodynamic initial-dip consists of both volumetric and oxymetric changes reflecting localized spiking activity, Frontiers in Neuroscience. 17 (2023)